COMPOSITIONAL SIMULATION OF CO_2 ENHANCED OIL RECOVERY IN UNCONVENTIONAL LIQUID RESERVOIRS

A Thesis

by

AMY FANGZE ZOU

Submitted to the Office of Graduate and Professional Studies of
Texas A&M University
in partial fulfillment of the requirements for the degree of

MASTER OF SCIENCE

Chair of Committee,	David S. Schechter
Committee Members,	Ding Zhu
	Mark Holtzapple
Head of Department,	A. Dan Hill

December 2015

Major Subject: Petroleum Engineering

ABSTRACT

After implications of hydraulic fracturing operations, the commercial production of tight formations and shale plays were successfully achieved in past decades. The industry now shifts its interest in enhancing the production after the stimulation treatment. Experimental results showed promising oil recovery potential using CO_2. This study utilizes commercial simulation software to investigate the oil production mechanisms from the matrix into the fracture by simulating two laboratory experiments, and evaluates the potential of using CO_2 huff n puff process to enhance the oil recovery in liquid rich shale plays with nano-Darcy range permeability values.

This study fully explores the mechanisms contributing to the oil recovery with numerical modeling of experimental works, and performs a thorough investigation on the effects of various parameters on oil recovery. The core scale modeling involves two methods of determining properties used to construct the 3D heterogeneous models. The experimental findings are then upscaled to a field case model where a single stage hydraulic fracture is modeled. The effects of reservoir properties and operational parameters on oil recovery are then investigated.

Diffusion is proven to be the dominating oil recovery mechanism with laboratory scale modeling. However, it is not as significant in the field scale model. Due to the difference in mass transfer mechanism between the core scale model and the field scale model, the two models are sensitivity to different parameters. The CO_2 huff n puff

process was found beneficial in both models in terms of enhancing the ultimate oil recovery in unconventional liquid reservoirs.

DEDICATION

This thesis is dedicated to my parents, my grandparents, and those who have supported me.

ACKNOWLEDGEMENTS

I would like to thank my committee chair, Dr. David Schechter, who took me as his student, served as the greatest mentor, and supported me throughout my graduate studies at Texas A&M University.

I would like to thank my committee member, Dr. Ding Zhu, who encouraged me to become a petroleum engineer seven years ago, and has been a friend and a life coach to me throughout the years.

I would like to thank my committee member, Dr. Mark Holtzapple, to be on my committee and showed great support.

I would also like to thank all professors at the petroleum engineering department at Texas A&M University for teaching and guiding me through many obstacles.

Finally, I would like to thank my friends and colleagues for inspiring and encouraging me. And, the department faculty and staff for making my time at Texas A&M University a great experience. I would like to extend my gratitude to the support teams at CMG (Computer Modeling Group Ltd.) and Eclipse (Schlumberger).

NOMENCLATURE

°C	Degree Celsius
cm	Centimeter
cp	Centipoise
CT	Computed tomography
°F	Degree Fahrenheit
EOR	Enhanced oil recovery
EOS	Equation of State
FCM	First contact miscible
HCPV	Hydrocarbon Pore Volume
k	Absolute permeability
m	Cementation factor
MCM	Multiple contact miscible
md	Milli-Darcy
ml	Milliliter
MMP	Minimum miscibility pressure
nd	Nanodarcy
p	Pressure
PR	Peng-Robinson EOS
PV	Pore volume
RF	Recovery factor

SRV	Simulated reservoir volume
T	Temperature
ϕ	Porosity
σ	Interfacial tension
μ	Viscosity

TABLE OF CONTENTS

Page

ABSTRACT ii

DEDICATION iv

ACKNOWLEDGEMENTS v

NOMENCLATURE vi

TABLE OF CONTENTS viii

LIST OF FIGURES xi

LIST OF TABLES xv

1. INTRODUCTION 1

1.1 Objectives and Scope 2
1.2 Overview of Thesis Sections 2

2. LITERATURE REVIEW 3

2.1 Overview of Available EOR Methods 4
2.1.1 Chemical Methods 5
2.1.2 Thermal Methods 6
2.1.3 Microbial Methods 6
2.1.4 Gas Injection Methods 6
2.1.4.1 Cyclic Gas Injection 7
2.2 Miscibility 8
2.2.1 First Contact Miscible 9
2.2.2 Multiple Contact Miscible 12
2.2.3 Miscibility Determination 14
2.2.3.1 Slim Tube Experiment 14
2.2.3.2 Compositional Simulation 16
2.3 Selection of the Gas EOR Agent 16
2.3.1 Physical Properties of CO_2 17
2.3.2 Advantages of CO_2 18
2.3.3 Operational Challenges Associated with CO_2 19
2.4 Literature Review of Laboratory Studies 20
2.5 Literature Review of Simulation Studies and Modeling Theory 22

3. MASS TRANSFER THEORY 27

3.1 Dispersion 27
3.2 Diffusion 30
3.2.1 The Classical Fick's Law 31
3.2.2 The Irreversible Thermodynamic Model 32
3.2.2.1 Chemical Potential and Fugacity 33
3.3 Diffusion Coefficient 37

4. NUMERICAL SIMULATION 38

4.1 Commercial Simulators 38
4.2 Basic Reservoir Simulation Properties 40
4.2.1 Porosity 40
4.2.2 Absolute Permeability 40
4.2.3 Relative Permeability 42
4.2.4 Capillary Pressure 43
4.2.5 Surface Tension 44
4.2.5.1 Relative Permeability Interpolation 45
4.2.5.2 Capillary Pressure Interpolation 48
4.2.6 Diffusion Coefficient 49
4.3 CO_2 Core Flood Experiments with Shale Cores 50
4.4 Experiment Modeling 52
4.4.1 Fluid Model 52
4.4.1.1 Fluid Characterization 53
4.4.1.2 Component Lumping 54
4.4.1.3 Fluid Model Regression 55
4.4.1.4 Fluid Properties 59
4.4.2 Experiment Model Grid and Property Sensitivity Analysis 62
4.4.2.1 Grid Sensitivity 62
4.4.2.2 Property Sensitivity Analysis 66
4.4.2.2.1 Matrix Permeability 67
4.4.2.2.2 Matrix Porosity 75
4.4.2.2.3 Fracture Permeability 76
4.4.2.2.4 Fracture Porosity 77
4.4.2.2.5 Water Saturation 78
4.4.2.2.6 Diffusion Coefficient 80
4.4.2.2.7 Pressure 82
4.4.2.2.8 Capillary Pressure for the Immiscible Case 83
4.4.3 Experiment I – Homogenous 3D Model 85
4.4.3.1 Results and Discussion 87
4.4.3.1.1 Sensitivity Analysis of Soaking Time 93
4.4.4 Experiment I – Heterogeneous 3D Model 94
4.4.4.1 Property Determinations 95

4.4.4.2 Results and Discussions 97
4.4.5 Experiment II – Heterogeneous 3D Model 101
4.4.5.1 Porosity Map Determination 102
4.4.5.2 Results and Discussions 110
4.5 Field Case Modeling 113
4.5.1 Fluid Model and Reservoir Properties 114
4.5.2 Primary Depletion and Base Case 121
4.5.2.1 Primary Depletion 121
4.5.2.2 Huff n Puff 1 Cycle 123
4.5.3 Sensitivity Analysis of Reservoir Properties 125
4.5.3.1 Matrix Porosity 125
4.5.3.2 Matrix Permeability 127
4.5.3.3 Fracture Porosity 128
4.5.3.4 Fracture Permeability 129
4.5.3.5 Capillary Pressure 130
4.5.3.6 Effect of Diffusion 132
4.5.4 Sensitivity Analysis of Operational Parameters 135
4.5.4.1 Time of First Injection 135
4.5.4.2 Injection Rate 136
4.5.4.3 Injection Pressure 138
4.5.4.4 Length of Injection Time 139
4.5.4.5 Length of Soaking Time 140
4.5.4.6 Number of Cycles 142
4.5.4.7 LPG Injection 143
4.5.4.7.1 Reservoir Temperature 145
4.5.4.7.2 Different LPG Compositions 147

5. CONCLUSIONS AND RECOMMENDATIONS 149

5.1 Conclusions 149
5.2 Future Work Recommendations 151

REFERENCES 152

LIST OF FIGURES

Page

Fig. 1 – Pseudo-ternary diagram of a fluid system (Adapted after Donaldson *et al*. 1989). 10

Fig. 2 – Pseudo-ternary diagram of first contact miscibility. 11

Fig. 3 – Pseudo-ternary diagram of multiple contact miscibility vaporizing process. 13

Fig. 4 – Using the slim-tube oil recovery versus pressure curve to estimate the MMP of a fluid system at constant temperature (Adapted after Jarrell *et al.* 2002)... 15

Fig. 5 – Phase diagram of pure CO_2 (Adapted after Lie 2013). 17

Fig. 6 – Five dispersion regime characterization. (Adapted from Lie 2013). 29

Fig. 7 – Relative permeability curve scaling between miscible and immiscible conditions. 48

Fig. 8 – Measured and simulated density of the dead oil at various temperatures. 56

Fig. 9 – Measured and simulated viscosity of the dead oil at various temperatures. 58

Fig. 10 – Simulated slim tube result at 150 ºF using PVTsim. 59

Fig. 11– Oil density change with different mole fraction of CO_2. 60

Fig. 12 – Oil viscosity change with different mole fraction of CO_2. 61

Fig. 13 – Oil swelling factor with different mole fraction of CO_2. 62

Fig. 14 – Grid sensitivity on both radial and Cartesian grids with different degrees of refinement. 64

Fig. 15 – Grid sensitivity results for the five grids being investigated. 65

Fig. 16 – The slice model used for property sensitivity analysis. The red region represents the matrix, which is saturated with oil and water. The blue region represents the gas bearing fracture. 66

Fig. 17 – Cumulative oil production and oil production rate for cases with different matrix permeability values (Scenario 1). 68

Fig. 18 – Average pressure in the core region over time (Scenario 1). 70

Fig. 19 – Cumulative oil production for cases with different matrix permeability values (Scenario 2). 71

Fig. 20 – Average pressure in the core region over time (Scenario 2). 73

Fig. 21 – Production versus square root of time. The linear relationship represents diffusion dominate flow. 74

Fig. 22 – Cumulative oil production for cases with different matrix porosity values. 76

Fig. 23 – Cumulative oil production for cases with different fracture permeability values. 77

Fig. 24 – Cumulative oil production for cases with different fracture porosity values. 78

Fig. 25 – Cumulative oil production for cases with different water saturation values. 79

Fig. 26 – Cumulative oil production for cases with different diffusion coefficient values. 81

Fig. 27 – Cumulative oil production for cases with different pressure values. 83

Fig. 28 – Three sets of capillary pressure curves representing low, mid and high ranges. 84

Fig. 29 – Cumulative oil production for cases with different capillary pressure curves. 85

Fig. 30 – COMP 2 mole fraction profile at 10 hours. The log scaled image shows the effect of gravity on the oil distribution in the fracture region. 88

Fig. 31 – Cumulative oil production from the matrix into the fracture for the three cases. 89

Fig. 32 – Cumulative oil production from the system (matrix and fracture) into the producers. 90

Fig. 33 – Molar fraction of each hydrocarbon components in the exported oil. 91

Fig. 34 – CO_2 production volume from the producers for case 1 and case 2. 92

Fig. 35 – Cumulative oil production from the producers for cases with different soaking times. 94

Fig. 36 – Sample porosity map for experiment I simulation. 96

Fig. 37 – Oil density change for the experiment I 3D heterogeneous model at time 0hr, 5hr, 10hr, 24hr, 48hr, and 72hr. 98

Fig. 38 – Oil viscosity reduction for the experiment I 3D heterogeneous model at time 0hr, 5hr, 24hr, 48hr. 100

Fig. 39 – Cumulative production for the experiment I 3D heterogeneous model. 101

Fig. 40 – Thin section images for core 2-1 (left) and core 2-2 (right). 103

Fig. 41 – Image analysis for core 2-1 porosity estimation. 104

Fig. 42 – Sample MicroCT image of core 2-1 taken in the XY plane. 106

Fig. 43 – Sample MicroCT image of core 2-1 taken in the XZ plane. 106

Fig. 44 – An enlarged view of a section of the XY plane view. 107

Fig. 45 – Porosity distribution for slice 3. 109

Fig. 46 – Cumulative oil production of experiment II 3D heterogeneous model. 110

Fig. 47 – Oil density change over time for slice 3 at time 0 hr, 2 hr, 5 hr, 10 hr, 24 hr, 48 hr, 72 hr, and 78 hr. 111

Fig. 48 – Schematic of the simulated reservoir volume (SRV). 113

Fig. 49 – Phase diagram of the live oil. 115

Fig. 50 – Oil density change at various pressure. 116

Fig. 51 – Oil viscosity change at various pressure. 116

Fig. 52 – Oil density change at various CO_2 mole fraction in oil. 117

Fig. 53 – Oil viscosity change at various CO_2 mole fraction in oil. 118

Fig. 54 – Oil volume change at various CO_2 mole fraction in oil. 118

Fig. 55 – Saturation pressure change at various CO_2 mole fraction in oil. 119

Fig. 56 – Cumulative oil production for the primary depletion cases with different producer BHP. 122

Fig. 57 – Cumulative oil production for all cases. 124

Fig. 58 – Cumulative production for matrix porosity sensitivity analysis. 126

Fig. 59 – Cumulative oil production of matrix permeability sensitivity analysis. 128

Fig. 60 – Cumulative oil production for fracture porosity sensitivity analysis. 129

Fig. 61 – Cumulative oil production for fracture permeability sensitivity analysis. 130

Fig. 62 – Cumulative oil production for matrix capillary pressure sensitivity analysis. 131

Fig. 63 – Cumulative oil production for diffusion coefficient sensitivity analysis (Scenario 1). 133

Fig. 64 – Cumulative oil production for diffusion coefficient sensitivity analysis (Scenario 2). 134

Fig. 65 – Cumulative oil production of sensitivity analysis on the starting time of the first injection cycle. 136

Fig. 66 – Cumulative oil production for sensitivity analysis on injection rate. 137

Fig. 67 – Cumulative oil production of injection pressure sensitivity analysis. 139

Fig. 68 – Cumulative oil production of injection duration sensitivity analysis. 140

Fig. 69 – Cumulative oil production for soaking time sensitivity analysis. 142

Fig. 70 – Cumulative production of number of cycles sensitivity analysis. 143

Fig. 71 – Cumulative production of CO_2 and LPG injections. 145

Fig. 72 – Cumulative production of CO_2 and LPG injections at different reservoir temperatures. 146

Fig. 73 – Cumulative production of LPG cases with different amount of C_2 added. 148

LIST OF TABLES

Page

Table 1 – The dimensions of the cores used in the two experiments (Modified after Tovar *et al*. 2014). 50

Table 2 – Chemical composition of the dead oil and the corresponding normalized mass percentage obtained from GC-MS analysis. 53

Table 3 – Weight-based pseudo-component lumping. 54

Table 4 – Measured and simulated density of the dead oil at various temperatures. 56

Table 5– Measured and simulated viscosity of the dead oil at various temperatures. 57

Table 6 – Properties of the fluid model after regression. 58

Table 7 – Grid sensitivity on both radial and Cartesian grids with different degrees of refinement. 63

Table 8 – Permeability values for different cases and the corresponding yielded recovery factors (Scenario 1). 68

Table 9 – Permeability values and the corresponding recovery factors for cases with different matrix permeability values (Scenario 2). 71

Table 10 – Matrix porosity values and the corresponding recovery factors. 75

Table 11 – Fracture permeability values and the corresponding recovery factors. 76

Table 12 – Fracture porosity values and the corresponding recovery factors. 78

Table 13 – Core region water saturation values and the corresponding recovery factors. 79

Table 14 – Diffusion coefficient calculated with the Sigmund correlation with correction. 80

Table 15 – Diffusion coefficient values and the corresponding recovery factors. 81

Table 16 – Pressure values and the corresponding recovery factors for different cases. . 83

Table 17 – Capillary pressure ranges and the corresponding recovery factors for different cases. 84

Table 18 – Diffusion coefficients used to match the ultimate recovery volume. 96

Table 19 – Effective porosity values of core 2-1 and 2-2 measured with helium porosimeter. 102

Table 20 – Live oil composition and properties. 114

Table 21 – Simulated reservoir properties. 120

Table 22 – Diffusion coefficient used in the field model. 120

Table 23 – Cases with different producer BHP and the corresponding recovery factors. 122

Table 24 – Recovery factor for the different cases and recovery factor increment for the injection cases. 123

Table 25 – Recovery factor and recovery factor increment for different matrix porosity cases. 125

Table 26 – Matrix permeability sensitivity analysis. 127

Table 27 – Fracture porosity sensitivity analysis. 128

Table 28 – Fracture permeability sensitivity analysis. 130

Table 29—Sensitivity analysis of matrix capillary pressure. 131

Table 30 – Diffusion coefficient sensitivity analysis for 1000 psi BHP cases (Scenario 1). 132

Table 31 – Diffusion coefficient sensitivity analysis for 1000 psi BHP cases (Scenario 2). 133

Table 32 – Sensitivity analysis on the starting time of the first injection cycle. 135

Table 33 – Sensitivity analysis on injection rate. 137

Table 34 – Sensitivity analysis of injection pressure. 138

Table 35 – Sensitivity analysis of the length of injection time. 140

Table 36 – Sensitivity analysis for soaking time. 141

Table 37 – Sensitivity analysis of number of injection cycles. 143

Table 38 – Comparison of CO_2 and LPG performance. 144

Table 39 – Recovery factor of CO_2 and LPG injections at different reservoir temperatures.....146

Table 40 – Performance of LPG with different amount of C_2 added.....147

1. INTRODUCTION

One of the main interests of the current petroleum industry is to explore methods that can economically produce from the previously unprofitable plays. After implications of hydraulic fracturing operations, the commercial production of tight formations and shale plays were successfully achieved in past decades. Operators focused their resources on optimizing hydraulic fracturing designs and operation techniques (Tovar *et al.* 2014). According to EIA (2013) statistics, US oil production had observed an increase from 5 million barrel per day in 2005 to 6.5 million barrel per day in 2012 due to the advancements in horizontal drilling with multistage hydraulic fracturing. However, it is shown that, for most of the unconventional plays, the primary production declines rapidly resulting in a low recovery factor in a typical range of 3 to 5 percent of the original oil in place depending on the characteristics of the reservoir (Liu *et al.* 2014). In the cases of producing from reservoirs that have permeabilities in the scale of nano-Darcy, many studies are now focusing on methods that can efficiently recover the residual hydrocarbon left behind after primary depletion. Studies on using surfactants and various gas injections such as nitrogen, hydrocarbon gas and CO_2 have been conducted.

CO_2 EOR processes in unconventional plays cannot be considered the same as conventional CO_2 flooding due to the differences in reservoir petrophysics properties, fluid behaviors, and mass transfer mechanisms. This study will investigate the oil production mechanisms from the tight matrix into the fractures on both core scale and

field scale, the change in phase behavior when CO_2 interacts with the resident fluid under different conditions, and factors that affect the dispersion of CO_2 in the porous media during CO_2 EOR processes in unconventional oil rich reservoirs with nano-Darcy range permeability.

1.1 Objectives and Scope

The objectives of this study are to

- Understand the significance of the effect of convection and molecular diffusion on oil recovery from the matrix into the fractures;
- Simulate laboratory core flood experiments;
- Perform sensitivity analysis on different parameters that affect the oil recovery in both laboratory and field scales;
- Evaluate the potential of using CO_2 as an EOR agent in field scale unconventional liquid reservoirs.

1.2 Overview of Thesis Sections

This thesis is divided into five chapters. The next chapter presents the problem statement, background information, and literature review. Chapter 3 provides detailed theory background on mass transfer used in this study. Chapter 4 describes the software used in this study, basic reservoir simulation properties, experimental work being modeled, and the modeling of the experiments as well as a synthetic field case. The last chapter summarizes the work and presents the conclusions and future work recommendations.

2. LITERATURE REVIEW

Since the start of the first commercial CO_2 injection project at SACROC Unit, TX in 1972, CO_2 has been recognized as one of the most important and successfully applied EOR processes in the U.S.. Statistics show that out of the 153 active CO_2 EOR projects worldwide, 139 of them are in the U.S. (Ahmed *et al.* 2012). CO_2 flooding is the only EOR method in the U.S. that was consistent and economical since the drop in oil prices in the 1980s.

For the past few decades, due to the increasing demand of energy and the advancements in horizontal drilling and hydraulic fracturing technologies, the industry reallocated its resources into exploring ways to produce oil from the previously unprofitable shale plays. The current technique to produce from the shale plays is through primary depletion. However, studies have shown that the recovery factor remains low, and large sums of the reserves are left behind in the reservoirs (Liu *et al.* 2014). Hence, to look ahead into the future production of the remaining reserves because of the declination of primary recovery to an uneconomic level, operators are shifting their attentions into research that focuses on EOR methods in shale reservoirs. However, due to the many differences between conventional and unconventional reservoirs, the EOR methods that are suitable in conventional reservoirs need to be re-evaluated when applied in unconventional reservoirs. Studies on using surfactants and various gas injections such as nitrogen, hydrocarbon gas and CO_2 have been conducted. The next section will briefly discuss the different available EOR techniques, and why CO_2

injection is a preferred method chosen to be studied in this work due to the many advantageous properties of CO_2.

2.1 Overview of Available EOR Methods

Enhanced oil recovery (EOR), also known as tertiary recovery, serves the purpose of producing the remaining hydrocarbons after the depletion of the reservoir energy (primary recovery) or after pressurizing the reservoir and displacing the hydrocarbon with gas or water (secondary recovery). EOR processes are necessary when the pressure maintenance processes become inefficient or in the cases where secondary recovery processes are not applicable due to the low recovery potential. They can be classified into four categories (chemical method, thermal method, microbial method and gas injection) and will be discussed individually in the following sections. Unlike primary and secondary recovery, EOR processes increase production mainly by altering the rock and fluid properties, which are more suitable in unconventional reservoirs where the option of secondary recovery is not applicable due to the low injectivity. During a conventional EOR scheme, the overall recovery is determined by both macroscopic and microscopic displacement efficiency. The macroscopic displacement efficiency is affected by the reservoir heterogeneities and anisotropy, characteristics of the matrix, fluid mobility, flood patterns, etc.. The microscopic displacement efficiency is affected by interfacial tension, wettability, capillary pressure and relative permeability (Terry 2001). Because of the difference in mass transfer mechanisms, some of the above factors remain significant in unconventional cases, whereas some factors do not affect

the recovery. This study will focus on exploring the effect of microscopic characteristics by simulating two laboratory experiments, then expand to a synthetic field case study.

The following sections discuss the different EOR methods, the oil recovery mechanisms, and the limitations of each method, which provide the reasons for considering CO_2 injection as the most plausible option to be applied in liquid rich shale reservoirs.

2.1.1 Chemical Methods

Chemical flooding mainly relies on mobility control and sweep efficiency improvement or surface tension reduction to favor water imbibition. Chemical flooding can be characterized into polymer flooding, surfactant flooding, and caustic flooding. Other than gas injection, studies are heavily focused on utilizing surfactant chemical processes in unconventional reservoirs. A surfactant is a surface active agent containing a hydrophobic and a hydrophilic end (Terry 2001). When in contact with oil and water, surfactant significantly lowers the interfacial tension between the two phases and shifts the relative permeability curves so the oil is more mobile at lower saturations. However, Sheng (2014) stated that in practice, surfactant methods require high fracture density to achieve economic recovery. Donaldson *et al.* (1989) also mentioned that surfactant flooding is very complex and has the highest degree of uncertainty during the designing process. Limitations associated with using surfactants are temperature, salinity and lithology.

2.1.2 Thermal Methods

Thermal EOR methods are generally applied in heavy oil reservoirs and tar sands. Oil viscosity reduces significantly when the temperature rises (Terry 2001). Thermal EOR are processes such as steam injection, cyclic steam injection (huff n puff), steam assisted gravity drainage (SAGD), hot water flooding and in-situ combustion. However, not all reservoirs are suitable for thermal EOR methods. For instance, steam flooding is limited to shallow reservoirs because the loss of energy in the wellbore, and in-situ combustion requires low API oil with enough heavy components to serve as the fuel source (Terry 2001). Because of the reasons mentioned above, thermal EOR methods are not considered beneficial in shale reservoirs, and no studies have investigated the potential of using thermal EOR methods in liquid rich shale reservoirs.

2.1.3 Microbial Methods

Similar to chemical EOR processes, microbial EOR method is the injection of micro-organisms (microbes and nutrients) to generate polymers or surfactants to assist in oil production. Very few pilot projects have been conducted on this method, and according to Terry (2001), applying microbial processes in reservoirs with low injectivity produces polymers that damage the near wellbore regions. Therefore, microbial EOR method is not considered to be applicable in shale reservoirs.

2.1.4 Gas Injection Methods

Gas injection is the oldest EOR method, and one of the most commonly known secondary and tertiary recovery methods employed in many reservoirs. According to various studies, gas injection shows very promising potential in improving hydrocarbon

recovery in tight or shale reservoirs with natural and hydraulic fractures. The category of gas injection include gas flooding, water-alternating-gas (WAG) and huff n puff. In conventional reservoirs, where the gas is able to enter and flow through the matrix, gas flooding could be a feasible approach. However, in unconventional reservoirs that have nano-Darcy permeabilities, natural fracture complexity and extensive fracture network, gas could easily break through to the producers via the fractures, bypassing the oil bearing matrix (Hawthorne *et al.* 2013). Therefore, cyclic gas injection is being considered in this study as well as most other studies focusing on gas EOR in shale.

2.1.4.1 Cyclic Gas Injection

Cyclic injection, also known as huff n puff, is a process similar to cyclic steam injection but more applicable in reservoirs containing light oil (Thomas and Monger 1991). In the process, a well is used to inject a gas solvent (e.g. CO_2), and the well is shut in for a period of soaking time. During the soaking time, the injected gas solvent provides pressure support for the depleted reservoir and changes the rock and fluid properties in the reservoir to a better state for oil production. Then, the well is alternated into a producer through which hydrocarbon as well as the injected gas are produced. Studies conducted on the cyclic gas injection process mainly investigate the effects of pressure, soaking time and number of cycles. In the cases of unconventional reservoirs where gas solvent mainly exists in the fractures after being introduced into the reservoir, the mass transfer between the matrix and fractures during soaking times and production times are also investigated.

2.2 Miscibility

Unlike water or water based flooding methods, gases such as CO_2, nitrogen or hydrocarbon gas can achieve miscibility with the resident hydrocarbon when certain conditions are met. Therefore, gas injection can be further divided into immiscible and miscible processes.

During immiscible processes, the gas is injected at pressures that are below the minimum miscibility pressure (MMP) to provide pressure support, displace the oil, swell the oil, and reduce the oil viscosity. The lower pressure injection is suitable for various reservoir conditions, such as with the presence of light crude, shallow reservoirs with low fracture gradients, and low reservoir pressures. Studies have shown that gas injection has higher end point recovery than water flooding in conventional reservoirs (Mohammadi *et al*. 2011). Two case studies discussed by Donaldson *et al.* (1989) indicated that immiscible CO_2 flooding in conventional reservoirs have the potential for increasing oil production. However, during an immiscible displacement process, the biggest limitation is that the microscopic displacement efficiency does not reach unity (Green and Willhite 1998), since the microscopic displacement efficiency largely depends on the interfacial forces between the crude oil, injected gas and rock. The residual oil is trapped inside the pores with small pore throats due to capillary forces and is not moved by the flow.

The development of miscibility between the injected solvent gas and the resident oil overcomes the limitation of immiscible flood. Studies have shown the oil recovery is significantly higher under miscible conditions compared with immiscible conditions

because the injected gas is capable of displacing 100 percent of the resident oil (Pasala 2010). Therefore, in most gas injection schemes, achieving a miscibility or a near-miscibility condition between the injected gas and the resident oil is a critical factor in determining oil recovery.

Miscibility of two fluids develops when they are able to mix to form a single phase at all proportions (Green and Willhite 1998). Miscibility achieves when the pressure is above the minimum miscibility pressure (MMP). Interfacial tension/surface tension approaches zero when the two fluids become miscible, which serves as an indication of how miscible the two fluids are. The miscibility of two phases is affected by factors such as composition, temperature and pressure. Generally speaking, as the temperature increases, the gas phase is less miscible with the liquid phase, whereas increasing the pressure makes the two phases more miscible. Miscible flooding can be further categorized into first contact miscible and multiple contact miscible processes.

2.2.1 First Contact Miscible

A classic example of first contact miscibility is alcohol and water. The two fluids mix instantaneously when in contact at any proportion leaving no phase discontinuity between them. LPG (liquefied petroleum gases), which contains hydrocarbons with low molecular weights, can achieve first contact miscibility with crude oil at a much lower pressure than other gases. The first contact miscible process can be explained using a pseudo-ternary diagram. **Fig. 1** is a pseudo-ternary diagram of a hydrocarbon fluid system.

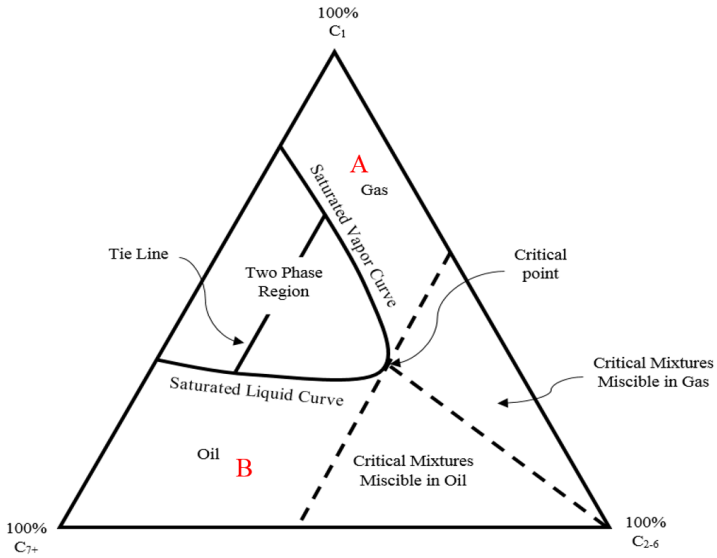

Fig. 1 – Pseudo-ternary diagram of a fluid system (Adapted after Donaldson *et al.* 1989).

According to Pedersen *et al.* (2014), a hydrocarbon system can be generally described with three pseudo-component fractions: C_1, C_2-C_6, and C_{7+}. Based on the physical conditions and composition, one can determine whether the mixture is in the gas, liquid or two-phase region. For instance, mixtures with the composition in region "A" exist as gas, and mixtures in "B" exist as liquid.

An example of first contact miscibility can be illustrated using point "O" and "P" on the pseudo-ternary diagram as shown in **Fig. 2**.

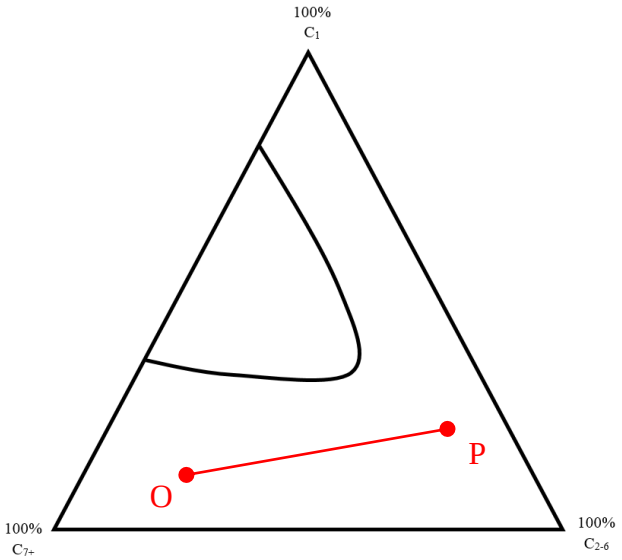

Fig. 2 – Pseudo-ternary diagram of first contact miscibility.

Mixing processes are represented as straight lines on a pseudo-ternary diagram. Let “O” represent oil and “P” represent LPG. By connecting the two points with a straight line, each point on the line “OP” represents an overall composition when “O” and “P” are mixed at a certain proportion. As shown in Fig. 2, the line “OP” does not cross the two phase region. It indicates that when the two fluids, “O” and “P”, mix at any proportion, the resulting mixture exists as a single phase. Therefore, “O” and “P” can achieve first contact miscibility.

It is easier to achieve first contact miscibility with oil during a LPG flood than during other gas flooding. However, since the price for LPG is relatively high, it is more practical to choose cheaper gases, such as CO_2 and nitrogen. Although such gases cannot achieve first contact miscibility with the crude oil at normal reservoir and operating

conditions, they can achieve multiple contact miscibility with the crude oil through either condensing or vaporizing processes.

2.2.2 Multiple Contact Miscible

CO_2 and Nitrogen establish miscibility with crude oil via a dynamic multiple contact process, which means the two phases are not miscible when first in contact, but require components transferring back and forth between the gas and the crude oil until the two fluids cannot be distinguished from each other. Two mechanisms involved in a multiple contact process are condensing and vaporizing. During a condensing process of rich gas and crude oil, the hydrocarbon components in the gas dissolve in the oil phase and thus generate a mixture bank that results in miscibility. For lean gas and CO_2, the mechanism is mainly vaporization, where the light and intermediate components of the oil phase transfer into and enrich the gas phase, forming a mixture bank that eventually becomes miscible with the original oil. A dry gas vaporizing process is illustrated with a pseudo-ternary diagram in **Fig. 3.**

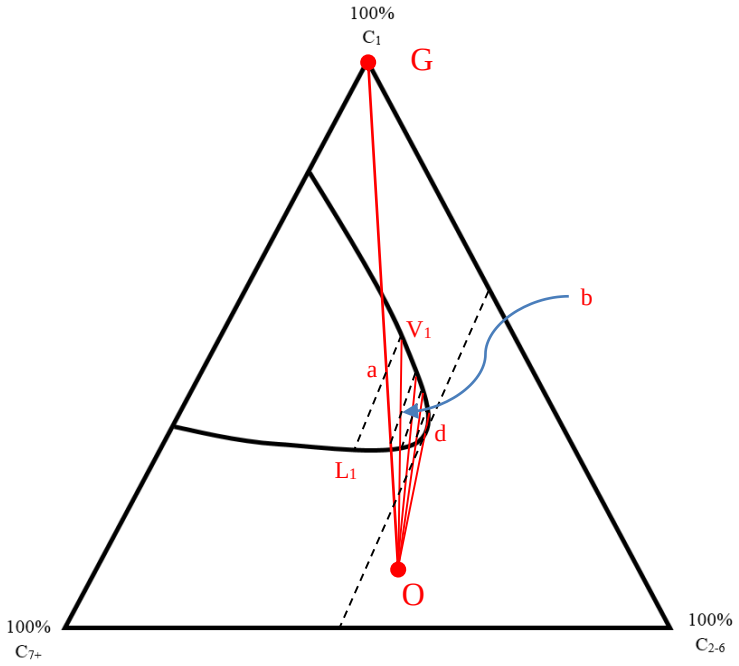

Fig. 3 – Pseudo-ternary diagram of multiple contact miscibility vaporizing process.

Let point "O" represent the crude oil and point "G" represent the injected lean gas. When the lean gas displacement front is in contact with the oil, the two fluids mix and form a mixture "a" at the intersection of the line "OG" and the tie-line. This mixture "a" exists in the two phase region, and therefore can be separated into vapor phase "V_1" and liquid phase "L_1". Since gas moves faster than liquid, vapor "V_1" gets in contact with the fresh crude ahead and forms another mixture "b" at the intersection of "OV_1" and the tie-line. Similar to mixture "a", mixture "b" can be further separated into a vapor phase and a liquid phase, which can be further mixed with the crude oil "O". The process repeats until the mixture forms a single phase with the crude oil "O" at point

"d", which lies on the critical tie line. After this point, the process becomes fully miscible.

2.2.3 Miscibility Determination

As mentioned previously, miscible gas injection is one of the most widely applied EOR methods. The MMP is the minimum pressure required for the multiple contact miscibility to occur at the reservoir temperature (Jarrell *et al.* 2002). Accurately predicting or measuring the MMP of the fluid system is critical in designing miscible gas injection processes. For instance, if the estimated MMP is lower than the actual MMP, the gas injection process will become immiscible and the oil recovery could be significantly lower than the predicted value. MMP can be measured with laboratory experiments or estimated using mathematical models. Laboratory methods include slim tube experiment, rising bubble experiment and vanishing interfacial tension (VIT) technique. Theoretical estimations include compositional modeling using equation of state (EOS), mixing-cell models and using various correlations. As the most frequently used experimental approach, the concept of a slim tube experiment will be briefly introduced in the next section. However, since the slim tube experiment is very time consuming and expensive, this study will employ the computational method using available commercial software.

2.2.3.1 Slim Tube Experiment

Slim tube experiments are conducted with a long coiled tube with a small diameter packed with uniform size particles that act as the porous medium. The ratio between the diameter and the length of the tube is small and the injection rate is low so

that gas fingering is minimized by transverse dispersion. For each test, the tube is initially saturated with oil at reservoir temperature, solvent is injected at a reasonable rate. The pressure on the production side is usually controlled by a back pressure regulator (BPR). For each testing pressure, oil production is measured as a function of the solvent injection volume. Conventionally, if the oil recovery factor achieves 95% after 1.2 pore volume (PV) of solvent injected, the two fluids are said to be miscible and the pressure is at MMP (Jarrell *et al*. 2002). Normally, several tests are performed at different pressures, and the oil recovery after 1.2 PV of solvent injection is plotted against the corresponding production pressure. **Fig. 4** is an example of using oil recovery versus pressure plot to determine the MMP.

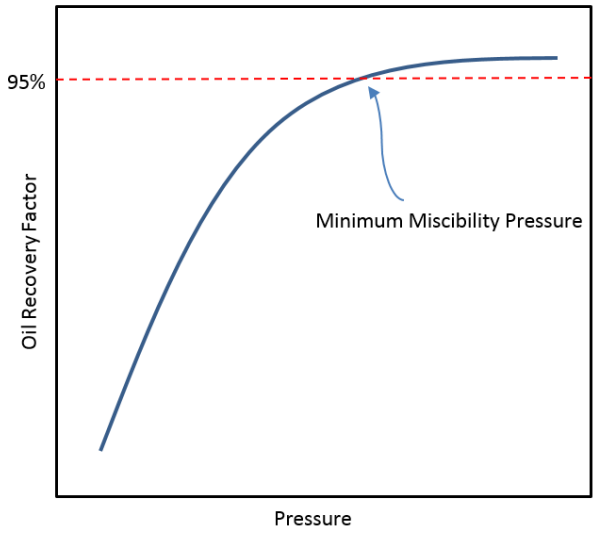

Fig. 4 – Using the slim-tube oil recovery versus pressure curve to estimate the MMP of a fluid system at constant temperature (Adapted after Jarrell *et al.* 2002).

As seen in Fig. 4, the pressure where a sharp change in the slope of the oil recovery curve occurs is the MMP for the fluid system. When pressure is above the MMP, the recovery does not increase as significantly as when the fluids are immiscible.

For slim tube experiments, the displacing fluid is assumed to ideally achieve local thermodynamic equilibrium with the displaced fluid at all points throughout the experiment. Therefore, the displacement efficiency, represented by the oil recovery, is considered to be purely a function of thermodynamic phase behavior of the fluid system and not related to the properties of the porous medium.

2.2.3.2 Compositional Simulation

As mentioned earlier, slim tube experiments are expensive and time consuming. Alternatively, commercial compositional simulators can be used for the purpose of estimating MMP.

In addition, one can employ software such as PVTsim Nova 1, which is a very powerful tool for building fluid models and performing various property estimations. As one of the functions of PVTsim, the MMP, FCM, and slim tube experiment simulations can be easily performed, which will be discussed in detail in Section 4.4.1.4.

2.3 Selection of the Gas EOR Agent

Studies on various gas injections such as nitrogen, flue gases, hydrocarbon gas and CO_2 have been conducted in the past. This study mainly focuses on exploring the potential of using CO_2 as the oil recovery agent due to the many advantageous properties of CO_2. LPG injection will also be considered in the field case simulation for the purpose of comparison.

2.3.1 Physical Properties of CO_2

A carbon dioxide (CO_2) molecule consists of one carbon and two oxygen atoms with a molecular weight of 44.01 g/mol. It may exist as a gas, liquid, solid, or supercritical fluid depending on the physical condition. **Fig. 5** shows the phase diagram of pure CO_2.

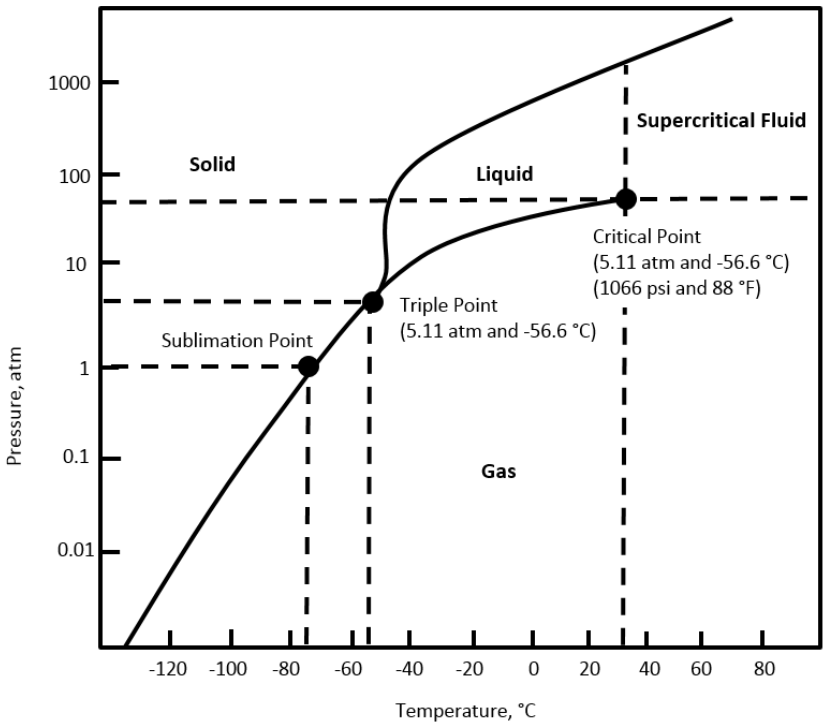

Fig. 5 – Phase diagram of pure CO_2 (Adapted after Lie 2013).

Under most reservoir and operational conditions, the pressure and temperature can exceed the critical point of CO_2 (1066 psi and 88 °F). Therefore, CO_2 exists as a

supercritical fluid, which has the density close to that of an oil, but viscosity close to that of a gas.

2.3.2 Advantages of CO_2

As mentioned in Section 2.2, the ability for gases to achieve miscibility with the resident oil plays a significant role in EOR processes. Laboratory experiments on using CO_2 as an EOR agent started in the 1950's. Research results show that at attainable reservoir pressures, CO_2 can develop MCM with the crude oil via vaporizing drive. As discussed in Section 2.2.2, the multiple contact miscible process between an injected gas and the crude oil can be represented using pseudo-ternary diagrams. For a CO_2 and crude oil system, the C_1 component on the pseudo-ternary diagram is substituted with CO_2. For the same pressure and temperature, the two-phase envelope on the pseudo-ternary diagram for a CO_2 system is much smaller than the one for a C_1 (or other gases such as nitrogen) system. Therefore, the MMP for a CO_2 and crude oil system is lower than that of a C_1 (or other gases such as nitrogen) and crude oil system. However, if the reservoir temperature is very high, the MMPs for CO_2, C_1, and nitrogen gases become similar. In general, CO_2 achieves miscibility with oil at a broader spectrum of conditions than other gases, such as lean gas and nitrogen. With the MMP being lower than the ones for other gases, CO_2 can be applied to heavier oils, shallower formations and formations that have low fracture gradients (Ahmed *et al.* 2012).

Viscous displacement, oil volume expansion, viscosity reduction, and vaporization of light hydrocarbon components up to C_{30} are considered to be the main hydrocarbon recovery mechanisms during CO_2 EOR processes depending on the

conditions. In addition, CO_2 is considerably cheaper than some of the gas candidates such as natural gas.

2.3.3 Operational Challenges Associated with CO_2

Issues associated with CO_2 EOR processes that need to be addressed before field operations include transportation, corrosion of the tubular, scale deposition, asphaltenes precipitation, and separating and recycling the gas.

There are three main sources to acquire CO_2: naturally occurring from reservoirs and industrial processes, carbon sequestration and artificially manufactures (Jarrell *et al.* 2002). It is critical to evaluate the availability of CO_2, cost of transportation and the quality of CO_2 during the planning of a CO_2 EOR project to ensure the project is economical.

CO_2 forms carbonic acid when dissolved in water, which is corrosive to carbon steel tubulars, especially at higher temperature. Corrosion resistant alloys or corrosion inhibitors are needed for a CO_2 process. However, the additional requirements add cost to the project. In addition, certain formations are sensitive to acidic solutions such as limestone formations. There is a potential issue associated with inorganic scale deposition.

Asphaltenes precipitation is a common problem during CO_2 flooding. Asphaltenes can block the pore throats and constrain flows. In addition, asphaltenes can deposit on the rock surface, alternating the rock wettability to oil wet, which is unfavorable for hydrocarbon production.

Furthermore, since the presence of contaminating gases such as methane and nitrogen increases the MMP of CO_2 and the oil system significantly, planning for a miscible CO_2 flood has high requirement for the purity of CO_2.

2.4 Literature Review of Laboratory Studies

Experimental work conducted by Tovar *et al*. (2014) used supercritical CO_2 and preserved sidewall shale cores. This experiment is the motivation of this simulation work and will be elaborated in detail in Section 4.3.

A similar study with both static (soaking) and dynamic (direct injection) CO_2 conducted by Hawthorne *et al*. (2013) using Bakken cores with low and ultra-low permeability showed that CO_2 is capable of producing a significant percentage of the oil inside tight shale cores with enough exposing times. In the study, Hawthorn *et al.* (2013) stated the difference between a conventional and unconventional EOR process. During a flooding in a conventional reservoir, CO_2 is capable of flowing through both the fractures and the matrix. Whereas in unconventional reservoirs, CO_2 is expected to flow rapidly through the fractures, and not significantly through the tight matrix, which eliminates the displacement mechanism that occurs during a conventional CO_2 flooding. The authors proposed a conceptual mechanism for CO_2 EOR in unconventional reservoirs with hydraulic fractures. First, the CO_2 flows into the fractures and migrates into the tight matrix due to pressure gradient. Oil in the matrix could possibly be pushed further into the matrix during this process. Next, CO_2 causes oil swelling and viscosity reduction because of the dispersion of CO_2 inside the oil phase, which will result in production. As the mixing of CO_2 and the oil continues, oil will continuously be

displaced to the surface of the rock and into the fractures. After the pressure equalizes in the fractures and the matrix, the concentration driven diffusion will aid in the further mixing of the fluids, which will continuously enhance the oil mobilization. Four sets of samples were used during the experiment, which were upper Bakken and lower Bakken cores with ultra-low permeability and porosity; middle Bakken cores with low permeability and porosity; and conventional sandstone cores. Furthermore, the samples were prepared into different shapes (rods, square rods, chicklets and crushed samples) to investigate the effect of surface area. The experimental results of surrounding the Bakken core with supercritical CO_2 at pressure far above the MMP without applying any additional pressure gradient showed significantly high recovery factors. Nearly 100% of the resident oil were recovered by using static CO_2 with conventional and low permeability middle Bakken cores. They concluded that the CO_2 EOR process would favor lighter hydrocarbons due to the "stripping" effects. Also, initial oil swelling was not a major contributing factor of oil mobilization. In addition, the rate of recovery decreased exponentially over time, and the rate of CO_2 transporting into the inside of the rock depends on the surface area of the rock (e.g. crushed samples have higher recovery than larger size samples).

In the study performed by Kovscek *et al*. (2008), both unconventional and conventional methods were investigated by using two injection schemes. Their samples had permeability in the range of 0.02 to 1.3 mD, and porosity in the range of 30 to 40%. The experiments from this study included depletion of live oil, CO_2 cocurrent injection and CO_2 countercurrent injection at immiscible and near miscible conditions. In their

experiments, direct gas injection was possible in siliceous shale due to the fact that the core was pressure depleted and pathways were opened for gas to enter. They concluded that exposing the siliceous shale cores to CO_2 would result in significant oil recovery even under immiscible conditions. Tests that were done under near miscible conditions resulted in slightly higher recovery than the immiscible cases. In 2010, Vega *et al*. (2010) continued with the work and reported experimental results under miscible condition using the same apparatus and type of rock mentioned above. Despite the low permeability, miscible cocurrent flooding yielded a recovery factor of 93% by constantly penetrating inside the core. For both studies with the siliceous shale, countercurrent scheme yielded higher recovery than cocurrent flow. Vega *et al*. (2010) also expanded the work into simulations, which will be discussed in Section 2.5.

2.5 Literature Review of Simulation Studies and Modeling Theory

Besides experimental work, modeling theories and simulation studies on CO_2 EOR process in shale oil reservoirs are available. However, since it is a fairly new area of focus for the industry, there is only a limited amount of work directly targeting this topic. Hence, some of the literature reviews will focus on work conducted with naturally fractured reservoirs, which have some degree of similarity in principal compared with fractured shale reservoirs.

Hoteit (2011) focused his study on the proper modeling of diffusion flux, determination of the diffusion coefficient, and the mass transfer at the fracture-matrix interface during CO_2 EOR processes in naturally fractured reservoirs. Along with other studies (McKay 1971; Darvish *et al*. 2006), Hoteit (2011) stated in his work that the

proper modeling of diffusion mechanisms is often neglected during reservoir engineering due to the facts that convection is the predominate fluid transport mechanism in most conventional recovery processes, and the artificial dispersion calculated by numerical methods is often high enough to compensate for diffusion. However, he concluded that molecular diffusion in the cases of heavy oil recovery and gas injection in fractured reservoirs with low matrix permeability is the dominate mechanism for oil production, and cannot be excluded during the modeling process. He also emphasized on the importance of modeling cross phase diffusion at the CO_2-oil interface. When the fractures are saturated with CO_2 and the matrix is saturated with resident oil, the diffusion influx with the presence of a phase boundary is zero, and the diffusion between gas and oil cannot be initiated. In addition, the author investigated the use of diffusion coefficient in a binary mixture system and a multicomponent mixture system. As mentioned in his work, the modeling of the diffusion fluxes in a multicomponent system is best achieved with the irreversible thermodynamic model because the classical Fick's law is more suitable for an ideal binary mixture (Bird *et al.* 2002). According to Hoteit (2011) and Shafikova (2013), representing the cross phase diffusion, or rather the interface mass transfer, with the classical Fick's law does not have a sound base. In the provided examples in his work, he illustrated that when using different diffusion coefficients for different components in both isothermal and isobaric binary and multicomponent systems with diffusion as the only dispersion mechanism, there is variation in pressure caused by the violation of the molar balance constraint in the context of having a zero total diffusion flux. This variation in pressure in an isobaric

system can be overlooked when masked by convection caused by artificial pressure difference when the porous medium is considerably permeable, which results in questionable pressure solutions. Another study by Hoteit (2013) gave an example of a multi-component gas-oil diffusion system. Similar conclusions were reached when assigning unequal diffusion coefficients for the different components resulted in a variation in pressure for an isobaric isolated system.

As mentioned in Section 2.4, Vega *et al.* (2010) simulated their miscible experiments with CMG GEM single porosity model. Their investigation mainly focused on the effect of core heterogeneity and diffusion, and drew the following conclusions. The cocurrent model (forced injection) was sensitive to the presence of high/low permeability channels, whereas in the countercurrent model, production was not significantly affected by permeability heterogeneity. In addition, the effect of introducing diffusion coefficients into the model was studied. However, for the models using dead oil, only slight increase in recovery was observed for the countercurrent cases, and negligible changes for the cocurrent cases. The authors argued the reason was that the CMG GEM single porosity model is only capable of calculating intra-phase diffusion but not the inter-phase or cross phase diffusion. Also, for the cocurrent cases, convection was dominating over diffusion, which minimized the effects of diffusion in the mass transfer processes.

Wan and Sheng (2015) used the CMG dual permeability model coupled with diffusion equations for their reservoir simulation of gas flooding. They concluded the dual permeability model is more time efficient and can capture the matrix-fracture mass

transfer properly. In addition, from their field scale simulation results, they drew the conclusion that the dominate recovery mechanism in low permeability shale reservoirs is diffusion, and the effect of diffusion on recovery is significant.

Fai-Yengo *et al*. (2014) used single block matrix/fracture model to investigate the mechanism of oil recovery from low permeability Bakken formation. They suggested that hydrocarbon component stripping due to the change in phase of the oil when miscible with CO_2 plays a large role in the recovery. They also suggested that capillary pressure needs to be taken into consideration because CO_2 is only able to recover the oil below the capillary threshold height with diffusion. On the other hand, capillary pressure does not have significant effect on oil recovery since the produced oil is transported into the fracture by gas phase diffusion.

Studies on nanoscale simulations of shale fluid transport are also available. Chen *et al*. (2015) reconstructed a 3D porous medium using SEM images of shale samples on a nanoscale. Since the focus of their study is shale gas, Knudsen diffusion was represented in the simulation. Models in nano-scale could be adopted in the study of liquid shale transport properties. However, it is difficult to achieve with the existing commercial simulators.

Another group of studies that investigated the efficiency of CO_2 or other gases as an EOR agent in unconventional reservoirs did not take diffusion into consideration. The study conducted by Chen *et al.* (2014) used an EOS based compositional simulator UT-COMP to simulate the effect of heterogeneity on primary recovery as well as the CO_2 huff n puff process in the Bakken. In their study, CO_2 dispersion is resulted from first

contact or multiple contact miscibility during injection. They concluded CO_2 migration into the shale matrix is very limited due to the low matrix permeability. The study conducted by Gamadi *et al.* (2014) evaluated the potential of natural gas injection in the Eagle Ford Shale. They concluded that the soaking period has significant effect on the ultimate recovery. The study conducted by Rivera (2014) took diffusion into consideration in his study. However, since his model was built with the CMG GEM single porosity model, the cross phase diffusion is neglected in his simulation. The higher recovery resulted from inter phase diffusion is purely due to the initial convection caused by pressure gradient. Example of similar other studies include Holme (2013), Wan *et al*. (2013), Liu *et al*. (2014).

Based on many literature, diffusion during gas injection has been recognized as a critical mechanism that affects the oil recovery in fractured reservoirs. If the diffusive flow in the matrix is being neglected during simulation, the calculated result will underestimate productivity (Ozkan *et al.* 2010; Karimaie 2007; Morel *et al.* 1993; Wan and Sheng 2015).

3. MASS TRANSFER THEORY

During a CO_2 injection in conventional reservoirs, either under miscible or immiscible conditions, CO_2 is able to flow through the permeable rock matrix. The oil recovery mechanism is a combination of gravity drainage, light component stripping, oil swelling, viscosity reduction, and viscous displacement. Perkins and Johnston (1963) stated that if the fluid is able to flow through the porous media, the flow mechanism is dominated by convective dispersion, meaning the velocity of the bulk fluid is too high for diffusion to have any significant effect on dispersion. However, when CO_2 flows through the fractures in an unconventional reservoir, the flow will not significantly go through the rock matrix. Therefore, convection could be eliminated as the main mechanism responsible for the mass transfer between the matrix and fracture (Hawthorne *et* al. 2013).

3.1 Dispersion

Dispersion is the mixing of fluids within a porous medium. Dispersion of the fluid is controlled by two main mechanisms: convection and molecular diffusion (Bird *et al.* 2002; Deen 1998). The convective transport is accompanied by bulk motion. It is the mechanism caused by the heterogeneities of the porous medium, which caused local fluid velocity variations (Lie 2013). Additionally, molecular diffusion is caused by the compositional difference, or chemical potential of the species. It is resulted from the motion of the molecules, and it is related to small pore scale molecular displacement

(Deen 1998). Longitudinal dispersion in a porous medium is represented with **Eq. 1** (Jarrell *et al*. 2002).

$$K_l = D_e + \alpha_1 v \qquad \textit{(Eq. 1)}$$

K_l is the longitudinal dispersion coefficient, D_e is the effective molecular diffusion coefficient, α_1 is the longitudinal dispersivity and v is the superficial velocity which is the product of porosity and interstitial velocity (Jarrell *et al.* 2002). Based on Eq. 1, the rate of dispersion is a sum of the convective and diffusive spreading.

To understand the dominant mechanism for dispersion, Lie (2013) used the characterization of the flow described by Sahimi (2011), which explains the five different regimes using the Péclet number. The Péclet number is defined as the ratio between convection and diffusion transport as shown in **Eq. 2**.

$$P_e = \frac{d_g v}{D_m} = \frac{D_L}{D_m} \qquad \textit{(Eq. 2)}$$

Where d_g is the average diameter of the particle in meter, v is the interstitial velocity in m/s, and D_m is the molecular diffusion coefficient in m^2/s. D_L is the longitudinal dispersion coefficient, which is proportional to the average fluid velocity (Perkins and Johnston, 1963), and describes the transport in the direction of the bulk flow. **Fig. 6** below shows the characterization of the five dispersion regimes in terms of the Péclet number.

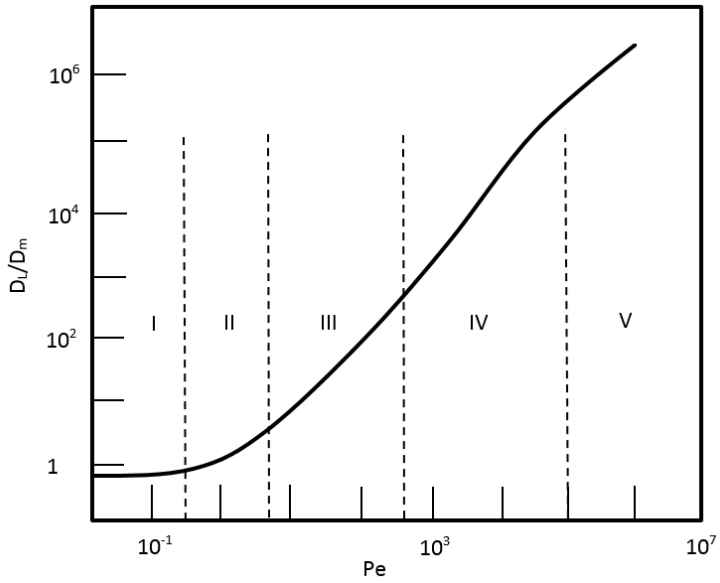

Fig. 6 – Five dispersion regime characterization. (Adapted from Lie 2013).

In region I, where the Péclet number is smaller than 0.3, the dispersion is dominated by diffusion. In this region, the fluid velocity is too low, and it gives enough time for molecular diffusion to take place.

In region II, where the Péclet number is greater than 0.3 but smaller than 5, diffusion is still dominating. However, convection will also aid in the process of dispersion.

In region III, where the Péclet number is greater than 5 but smaller than 300, the velocity is large enough for convection to become the dominant mechanism. However, the effect of diffusion on dispersion cannot be neglected in this flow regime. In this region, the flux caused by diffusion is inversely proportional to the diffusion coefficient of the species. This is because when diffusion influx is coming from the transverse

direction, the higher diffusion coefficient reduces the amount of time for the molecules to move forward along with the longitudinal convective flow.

In region IV, where the Péclet number is greater than 300 but smaller than 10^5 the dispersion is completely dominated by convection due to the considerably higher interstitial velocity. This is also referred to as mechanical dispersion.

Region V, which is also called the turbulent regime, is not of interest of the dispersion mechanism between shale matrix and the fractures.

In the scope of this study, which is to investigate the mechanism of oil recovery from the shale matrix into the fractures, the dispersion process is characterized into dispersion region I because of the nano scale permeability values. Therefore, when modeling CO_2 EOR in unconventional reservoirs, molecular diffusion is an important recovery mechanism. Many studies have reached similar conclusions (Hawthorne *et al.* 2103; Wan and Sheng 2015; Lie 2013; Grogan and Pinczewski 1987; Darvish *et al*. 2006; Hoteit and Firoozabadi 2009).

3.2 Diffusion

Molecular diffusion describes the random movement of molecules inside a system. Diffusion differs from convection in the sense that it happens with or without external forces, such as a pressure gradient or gravity. In an isobaric system, when there is a temperature or concentration gradient, the gradient tends to disappear as a function of time due to diffusion. In an isothermal and isobaric system in a porous medium, the rate of mass influxes due to diffusion is a function of pressure, temperature, composition, particle sizes, and the characteristics of the porous medium. The modeling

of mass transfer across a phase boundary has been extensively studied in the field of chemical engineering. The common approach is based on the film model, which assumes thermodynamic equilibrium at the gas-oil interface and the continuity of component fluxes across the interface (Hoteit 2013).

The rate and direction of the diffusion process is the diffusion flux. There are different models describing the calculation of the diffusion influx. The next two sections discuss the two models available in the simulator used for this study.

3.2.1 The Classical Fick's Law

The classical Fick's law is a very simple conceptual model to describe the movement of chemical components from one location to another. Analogous to Newton's Law of motion, Ohm's Law of electrical conduction and Fourier's Law of heat conduction, the Fick's Law describes the relationship between mass flux quantity and concentration gradient as shown in **Eq. 3**.

$$J_i = -D_i \frac{\partial c_i}{\partial d} \qquad (Eq.3)$$

Where

J_i is the diffusion flux,

D_i is the diffusion coefficient,

$\frac{\partial c_i}{\partial d}$ is the concentration gradient.

The classical Fick's law is ideal for diffusion calculation of a binary ideal fluid system. It simply assumes the diffusion process of each component is based on its concentration gradient and is independent from other components, which does not hold

true in a realistic case with multi-component mixture. Even for a binary system, one cannot predict when and where it may fail. As mentioned earlier, Hoteit (2013) provided examples of both binary and multi-component system diffusion studies. The examples showed the use of different diffusion coefficients for different components violated the molar flux balance and caused pressure variations in an isothermal and isobaric system. The solution to eliminate this pressure variance is to set the diffusion coefficients of all components to be equal or modify the diffusion coefficient of the last component so that the overall molar balance is honored. The variation in pressure is more significant when the system is at non-ideal conditions. Therefore, this study employs the irreversible thermal dynamic model, which uses the chemical potential to determine the diffusion flux instead of using the concentration gradient.

3.2.2 The Irreversible Thermodynamic Model

The irreversible thermodynamic model for diffusion flux calculation considers the chemical potential gradient to be the driving force for diffusion. The calculation takes the form as shown with **Eq. 4**.

$$J_i = -cD_i^a x_i \frac{1}{RT} \frac{\partial}{\partial d}\left[\mu_i - M_i g(h - h_o) + M_i D_i^T \ln(T)\right] \qquad (Eq.\ 4)$$

The above equation takes gravity and temperature gradients in addition to the chemical potential gradients into consideration. For an isothermal system that ignores gravity, Eq. 4 can be written as **Eq. 5**.

$$J_i = -cD_i^a x_i \frac{\partial}{\partial d} \ln(f_i) \qquad (Eq.\ 5)$$

D_i^a is the activity-corrected diffusion coefficient. Combining Eq. 3 and Eq. 5, the activity-corrected diffusion coefficient can be expressed with **Eq. 6**.

$$D_i^a = \frac{D_i}{\partial \ln(f_i) / \partial \ln(x_i)} \qquad \textit{(Eq. 6)}$$

3.2.2.1 Chemical Potential and Fugacity

According to Eq. 5, the contributing parameters involved in the diffusion flux calculation in an oil and gas system are porosity, oil and gas saturation, molar density of the oil and gas, mole fractions of the components, diffusion coefficients, and fugacity. Out of the above parameters, the molar density, diffusion coefficient and fugacity are functions of pressure and temperature. Therefore, although the initiation of the diffusion process is not governed by the system pressure, the rate of diffusion is controlled by the system pressure.

To understand the effect of physical conditions on diffusion flux, the term chemical potential needs to be briefly reviewed. This concept was introduced by Gibbs in 1957. This section will briefly explain the definition of chemical potential and fugacity. Detailed definition can be found in the work published by Firoozabadi (1999).

For an open system in which there is no restriction of material and energy transfer, the differential form of the fundamental equation is expressed in **Eq. 7**.

$$dU = \left(\frac{\partial U}{\partial S}\right)_{V,\underline{n}} dS + \left(\frac{\partial U}{\partial V}\right)_{S,\underline{n}} dV + \sum_{i=1}^{c} \left(\frac{\partial U}{\partial n_i}\right)_{S,V,n_i} dn_i \qquad \textit{(Eq. 7)}$$

Where

$\underline{n} \equiv (n_1, n_2 ... n_c)$,

U is the internal energy of the system,

S is the entropy of the system,

V is the volume.

The first two partial derivatives on the right side of Eq. 7 are given as:

$$\left(\frac{\partial U}{\partial S}\right)_{V,\underline{n}} = T \qquad \textit{(Eq. 8)}$$

$$\left(\frac{\partial U}{\partial V}\right)_{S,\underline{n}} = -P \qquad \textit{(Eq. 9)}$$

Where

T is the thermodynamic temperature,

P is the pressure.

And the coefficient of the last term is defined as the chemical potential, denoted by μ :

$$\mu_i = \left(\frac{\partial U}{\partial n_i}\right)_{S,V,n_i} \qquad \textit{(Eq. 10)}$$

The function of the chemical potential is similar to that of the pressure and temperature of a system. When a chemical potential gradient exists within a system, diffusion occurs from regions with high chemical potential to regions with low chemical potential despite of gravity or other external forces.

Combining Eq. 7 to Eq. 10, the expression for internal energy change can be written as **Eq. 11**.

$$dU = TdS - PdV + \sum_{i=1}^{c} \mu_i dn_i \qquad \textit{(Eq. 11)}$$

In general, for two cells separated by a permeable wall, which permits free transport of all components, the direction of the flow is solely determined by the chemical potential difference of the two cells. It is a form of work done by an isothermal and isobaric system due to composition changes to achieve thermal equilibrium.

The entropy of the two systems are:

$$dS^1 = \frac{dU^1}{T^1} + \frac{P^1}{T^1} dV^1 - \sum_{i=1}^{c} \left(\frac{\mu_i^1}{T^1} \right) dn_i^1 \qquad \textit{(Eq. 12)}$$

$$dS^2 = \frac{dU^2}{T^2} + \frac{P^2}{T^2} dV^2 - \sum_{i=1}^{c} \left(\frac{\mu_i^2}{T^2} \right) dn_i^2 \qquad \textit{(Eq. 13)}$$

Use the maximum entropy principle and rearranging Eq. 11 to Eq. 13:

$$dS = d(S^1 + S^2) = (\frac{1}{T^1} - \frac{1}{T^2}) dU^1 + (\frac{P^1}{T^1} - \frac{P^2}{T^2}) dV^1 - \sum_{i=1}^{c} (\frac{\mu_i^1}{T^1} - \frac{\mu_i^2}{T^2}) dn_i^1 = 0 \qquad \textit{(Eq. 14)}$$

The conditions for the two cells to achieve thermal equilibrium are $T^1 = T^2$, $P^1 = P^2$ and $\mu_i^1 = \mu_i^2$. Therefore, for an isothermal and isobaric system, the two cells need to have equal chemical potential instead of having equal mole fraction as defined in the classical Fick's law shown in Eq. 5.

Chemical potential is the partial molar Gibbs free energy, G. The Gibbs free energy is a function of temperature, pressure, and composition.

$$\mu_i = \left(\frac{\partial G}{\partial n_i} \right)_{T,P,n_i} \qquad \textit{(Eq. 15)}$$

Where

$$dG = VdP - SdT \qquad \textit{(Eq. 16)}$$

For a isothermal system,

$$dG = VdP \qquad \textit{(Eq. 17)}$$

For an ideal gas

$V = \frac{RT}{P}$, therefore combining Eq. 16 and Eq. 17

$$dG_{Ideal} = \frac{RT}{P} dP = RTd \ln P \qquad \textit{(Eq. 18)}$$

Combining Eq. 15 and Eq. 18

$$d\mu_i = RTd \ln(f)_{T,\underline{n}} \text{ and } \underset{P \to 0}{Lim}\left(\frac{f_i}{x_i P}\right) = 1 \qquad \textit{(Eq. 19)}$$

Where

x_i is the mole fraction,

f is the fugacity.

The term $\frac{f_i}{x_i P}$ is the fugacity coefficient. At low pressure, the fugacity coefficient equals one, which indicates the fluid behaves like an ideal fluid. In other words, fugacity is defined to represent the correct chemical potential for a real fluid with pressure P. The unit for fugacity is the same as the unit for pressure.

In an isothermal system, with diffusion as the only driving mechanism for mass transfer, the rate of mass transferring depends on the chemical potential (fugacity) of each components existing in the different phases.

For ideal gases, the fugacity is simply the pressure. For non-ideal gases, the fugacity does not equal the true pressure and needs to be corrected in terms of the compressibility factor and the pressure because of the change in Gibbs free energy.

$$\ln\left(\frac{f}{P}\right) = \int_0^P (z-1)\frac{dP}{P} \qquad \textit{(Eq. 20)}$$

For liquid, the fugacity at low pressure ideal conditions equals to the saturation pressure. At higher pressure, since the fluid properties does not change significantly, although there is a correction term for non-ideal liquid fugacity, the Gibbs free energy of a non-ideal liquid does not change much compared with ideal liquid.

3.3 Diffusion Coefficient

Numerous studies demonstrated or proposed methods to either physically measure the diffusion coefficient in the laboratory or estimate it using correlations. Physically measuring the diffusion coefficient for a multicomponent mixture can be challenging and sometimes inaccurate due to the fact that other factors such as gravity, capillary forces, convective mixing could interfere with the results. Correlations such as the ones proposed by Sigmund and Wilke-Chang are widely used in literature to predict the diffusion coefficient of mixtures. New models for diffusion coefficient estimation, such as the one developed by Leahy-Dios and Firoozabadi (2007), are not available in commercial software, and could be considered for future studies. The correlation used in this study is the Sigmund correlation (Sigmund 1976a; Sigmund 1976b), which will be discussed in detail in Section 4.2.6**.**

4. NUMERICAL SIMULATION

The purpose of numerical simulation is to provide mathematical model that validates the observed physical phenomena during laboratory experiments or field productions, and to be used for forecasting and optimization. This chapter describes the software used in this study, fundamental reservoir simulation properties, model sensitivity analysis, two simulations for laboratory experiments, as well as a field case study.

4.1 Commercial Simulators

Modeling with CMG GEM and Eclipse 300 were both investigated in this study. Attempts to use CMG GEM was made at first for the laboratory modeling. In CMG, the keyword DIFFUSION (CMG 2013) is used to define the gas diffusion for fractured reservoirs in dual porosity/dual permeability models. This keyword enables the diffusion mechanism to be included in the calculation for matrix-fracture molecular fluxes. The effective diffusion coefficient is corrected with tortuosity of the porous media. The rate of diffusion for the gas component depends on the contact area, porosity, tortuosity, gas saturation, diffusion coefficient, and the concentration gradient.

Another way CMG activates the diffusion option is by using the keywords DIFCOR-OIL, DIFCOR-GAS, or DIFFC-OIL and DIFFC-GAS (CMG 2013). The keywords DIFCOR-OIL and DIFCOR-GAS activate the diffusion coefficients calculated using either Sigmund or Wilke-Chang correlation. Whereas, the keywords DIFFC-OIL and DIFFC-GAS enable the user to defined the value for the diffusion coefficients

explicitly (CMG 2013). However, CMG is only capable of calculating the intra-phase diffusion for single porosity models, which means the cross phase diffusion is being neglected. When there is phase discontinuity at the boundary between the gas bearing fracture and the oil bearing matrix, small amounts of CO_2 are mixed into the oil phase due to the initial pressure difference. However, as the pressures in the fracture and the matrix regions become equal, no more CO_2 will enter the oil phase. The amount of CO_2 that is already mixed with the oil phase will diffuse within the oil phase and evenly distributed inside the homogenous core given enough time. Lie (2013) mentioned in his work that CMG GEM is unable to model the diffusion of supercritical CO_2, which is treated as a gas phase in the simulation, into the oil phase. Also, the simulation results do not agree with the observation from experimental work as shown in the simulation performed by Vega *et al*. (2010). Hoteit and Firoozabadi (2009) suggested a method to overcome the issue with modeling cross phase diffusion. They placed a thin block containing two phases between the fracture and the matrix, in which the gas and oil is in equilibrium. This approach was capable of producing reasonable results.

On the other hand, Eclipse 300 has the capability of modeling both intra phase and cross phase diffusion fluxes with single porosity models. There are two models available for the calculation of diffusion fluxes, which was discussed in Section 3.2.1 and Section 3.2.2. The first one is based on the classical Fick's law. In the classical Fick's law model, diffusion is driven by concentration gradient and can be activated using the keywords DIFFCOIL and DIFFCGAS (Eclipse 2014). The second model is based on the irreversible thermodynamics model, in which the diffusion is driven by

chemical potential gradient. This model was discussed in Section 3.2.2 and was selected for this study. It can be activated using keywords DIFFAOIL and DIFFAGAS (Eclipse 2014). To model the cross phase diffusion process, the cross phase diffusion coefficient is calculated with **Eq. 21** (Eclipse 2014).

$$Dog_i^a = \sqrt{Do_i^a \times Dg_i^a} \qquad \textit{(Eq. 21)}$$

4.2 Basic Reservoir Simulation Properties

4.2.1 Porosity

Porosity is the ratio of the pore volume to the bulk volume of a porous medium. The effective porosity, which is the ratio of the interconnected pore volume to the bulk volume, is defined using **Eq. 22,** where ϕ denotes porosity.

$$\phi = \frac{V_{pore}}{V_{bulk}} \qquad \textit{(Eq. 22)}$$

Porosity is an important parameter in reservoir engineering because it determines the storage capacity of the reservoir. In some cases where the compressibility of the rock is being considered in the model, porosity is affected by pressure and the total rock compressibility.

Various methods are available for porosity estimation such as volumetric measurement, injection methods, using logs, grain volume measurement, Boyle's law porosimeter, imaging analysis, etc.

4.2.2 Absolute Permeability

The permeability of a porous medium defines its capability to allow fluids to transmit through it. Permeability is defined using Darcy's law as shown with **Eq. 23**.

$$q = -\frac{kA}{\mu}\frac{\Delta P}{L} \qquad \textit{(Eq. 23)}$$

Where

q is the flow rate,

k is the permeability

A is the area of the cross section of the porous medium,

μ is the fluid viscosity,

ΔP is the pressure gradient across the porous medium,

L is the length of the porous medium.

The absolute permeability calculated with Darcy's law is only valid under certain assumptions such as laminar flow, steady state flow, saturated flow, homogenous system, isotropic media, etc. The application of Darcy's law might hold true for fluids flowing through a conventional rock, which allows laminar flow to develop by viscous forces. However, it is not suitable to use Darcy's law to model fluid transferring within an ultra-low permeability medium.

There are many methods to measure permeability. The most widely used method is by measuring the corresponding pressure drop across the core at different flow rates during a core flood experiment. The permeability is then calculated using Darcy's law. However, if the core has very low permeability, it is difficult to develop a steady state flow across the core. In such cases, unconventional ways such as pressure decay method or correlations are developed to estimate the permeability.

4.2.3 Relative Permeability

In a reservoir, where two or three fluids coexist within the pores, the transmitting of an individual fluid is generally inhibited and will flow at a different rate depending on the corresponding effective permeability. For a three phase system containing oil, water and gas, the effective permeability for each of the phases is calculated with **Eq. 24** to **Eq. 26**.

$$q_o = -\frac{k_o A}{\mu_o}\frac{\Delta P_o}{L} \qquad \textit{(Eq. 24)}$$

$$q_w = -\frac{k_w A}{\mu_w}\frac{\Delta P_w}{L} \qquad \textit{(Eq. 25)}$$

$$q_g = -\frac{k_g A}{\mu_g}\frac{\Delta P_g}{L} \qquad \textit{(Eq. 26)}$$

Where

q_o, q_w, q_g are the flow rate of the oil, water and gas phase, respectively,

k_o, k_w, k_g are the effective permeability of the oil, water and gas phase, respectively,

μ_o, μ_w, μ_g are the viscosity of the oil, water and gas phase, respectively,

ΔP_o, ΔP_w, ΔP_g are the pressure drop across the porous medium for the oil, water and gas phase, respectively.

Relative permeability is the ratio of effective permeability of a particular fluid at a particular saturation to absolute permeability of that fluid at total saturation.

$$k_{ro} = \frac{k_o}{k} \qquad \textit{(Eq. 27)}$$

$$k_{rw} = \frac{k_w}{k} \qquad \textit{(Eq. 28)}$$

$$k_{rg} = \frac{k_g}{k} \qquad \textit{(Eq. 29)}$$

Factors affecting relative permeabilities include saturation, saturation history (hysteresis), pore geometry, pore size distribution and wettability.

In the study conducted by Coats (1980), he proposed a model which accounts for the effect of surface tension on relative permeability. This model is used in simulating a miscible EOR process, and is discussed in detail in Section 4.2.5.1.

4.2.4 Capillary Pressure

Capillary pressure is defined as the pressure difference caused by the imbalance in the molecular forces of attraction across the interface of two immiscible fluids. The capillary pressure of a system holds each phase in equilibrium and controls the fluid distributions within a porous medium.

$$P_c = \frac{2\sigma \cdot \cos\theta}{r} \qquad \textit{(Eq. 30)}$$

When two immiscible fluids coexist inside a porous medium, one of them preferentially wets the surface and is defined as the wetting phase, whereas the other phase is the non-wetting phase. For instance, in a system containing both oil and gas phases, oil is the wetting phase, and gas is the non-wetting phase. Capillary of such a system is defined as the pressure differential between the non-wetting phase and the wetting phase as seen in **Eq. 31.**

$$P_{cog} = P_g - P_o \qquad \textit{(Eq. 31)}$$

4.2.5 Surface Tension

When two fluids (e.g. crude oil and injected gas) get in contact with each other, the thin layer between the two fluids is considered as the third phase which has its own properties that are intermediate between the two fluids (Reid *et al.* 1977). Surface tension is a measurement of the degree of miscibility between the two fluids, and the unit is usually in dynes per centimeter. In commercial simulators, the interpolations of the relative permeability curves and the capillary pressure curve in a miscible model are functions of the surface tension. Therefore, it is important to understand the calculations of surface tension as well as how it affects the calculations of the other properties.

If experimental values for the system surface tension at different pressures are available, they can be directly input into the simulator. Otherwise, the Macleod-Sugden correlation is used to calculate the system surface tensions as shown with **Eq. 32**.

$$\sigma = \left[\sum_{i=1}^{Nc} [P]_i \left(b_L^m x_i - b_V^m y_i \right) \right]^4 \qquad \textit{(Eq. 32)}$$

Where

σ [dynes/cm] is the surface tension,

P [(dynes/cm)$^{1/4}$cc/gm-M] is the temperature-independent parameter parachor values for each component,

b_L^m and b_V^m [gm-M/cc] are the molar densities for liquid and vapor phases,

x_i and y_i are the mole fractions for liquid and vapor phases.

For fluids that can form a single phase, such as miscible fluids or fluids near their critical points, the surface tension between them is zero as they can achieve

instantaneous equilibrium. When this occurs, the relative permeability curves and the capillary pressure curve for the system used in the actual calculation is different than the user input data. The interpolation of the curves between immiscible and miscible conditions is introduced in the next two sections.

4.2.5.1 Relative Permeability Interpolation

As mentioned earlier, relative permeability should be calculated in a system containing multiple phases. During the simulation, relative permeability should be input by the user. However, since the relative permeability curves undergo changes when the fluids achieve miscible conditions from immiscible conditions, Coats (1980) proposed a model that interpolates the relative permeability curves between immiscible and miscible conditions. An example of a two phase gas and oil system containing irreducible water saturation is shown below with **Eq. 33** to **Eq. 36**:

$$K_{rog} = K_{rocw}\{f(\sigma)\bar{S}_o^{n_{og}} + [1 - f(\sigma)]\bar{S}_o\} \quad \textit{(Eq. 33)}$$

$$K_{rg} = K_{rgcw}\{f(\sigma)\bar{S}_g^{n_g} + [1 - f(\sigma)]\bar{S}_g\} \quad \textit{(Eq. 34)}$$

$$\bar{S}_o = \frac{S_g - S_{gr}^*}{1 - S_{wir} - S_{gr}^*} \quad \textit{(Eq. 35)}$$

$$\bar{S}_g = \frac{1 - S_g - S_{wir} - S_{org}^*}{1 - S_{wir} - S_{org}^*} \quad \textit{(Eq. 36)}$$

Where

K_{rgcw} is the gas relative permeability at connate water,

K_{rocw} is the oil relative permeability at connate water

S_{wir} is the irreducible water saturation,

S_{gr} is the residual gas saturation,

S_{org} is the residual oil saturation.

The above equations simply imply the interpolation of the relative permeability curves below the minimum miscibility pressure is based on the ratio of the surface tension and the reference surface tension. $\overline{S}_o$ and $\overline{S}_g$ are relative permeabilities calculated with the Brooks-Corey model (Corey 1954). As the surface tension σ approaches zero, for instance at miscible conditions during a gas flooding, S^*_{gr} and S^*_{org} approach zero as shown with **Eq. 37** and **Eq. 38**.

$$S^*_{gr} = f(\sigma) S_{gr} \qquad \textit{(Eq. 37)}$$

$$S^*_{org} = f(\sigma) S_{org} \qquad \textit{(Eq. 38)}$$

In this case, $\overline{S}_o$ and $\overline{S}_g$ are linear functions of gas (or oil) saturation.

$f(\sigma)$ is the interpolation factor, which is a function of the surface tension between the gas and oil phases. In a simulation model, $f(\sigma)$ can be either manually entered, or estimated using **Eq. 39**.

$$f(\sigma) = \min\left[1, \left(\frac{\sigma}{\sigma_0}\right)^{\frac{1}{n_1}}\right] \qquad \textit{(Eq. 39)}$$

Where

σ is the surface tension,

σ_0 is the reference surface tension,

n_1 is the exponent of the surface tension ratio typically in the range of 4 to 10.

As mentioned in the previous section, two fluids are miscible when the surface tension between them is zero. As indicated by Eq. 39, $f(\sigma)$ equals zero when the surface tension equals zero, the relative permeability curves become straight lines with the same end points as the immiscible relative permeability curves. Therefore, the residual saturations are scaled based on the immiscible relative permeability curves in this case. On the other hand, as the surface tension approaches the reference surface tension, the two fluids become more immiscible. When the surface tension becomes equal or larger than the reference surface tension, $f(\sigma)$ equals one, and the relative permeabilities equal to the immiscible relative permeabilities, which are generally represented by the Brook-Corey model as mentioned earlier. The interpolation of the relative permeability curves is demonstrated in **Fig. 7**.

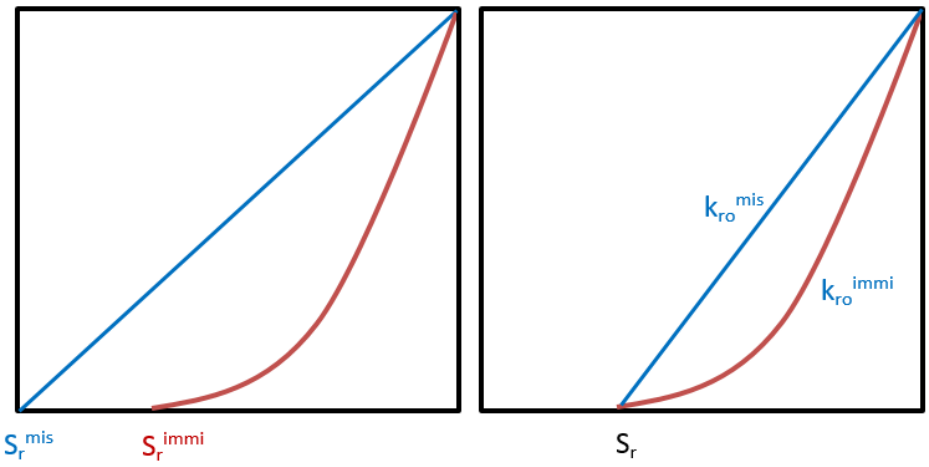

Fig. 7 – Relative permeability curve scaling between miscible and immiscible conditions.

4.2.5.2 Capillary Pressure Interpolation

Similar to relative permeability curves, the capillary pressure curve is interpolated using the same method proposed by Coats (1980). Oil/gas capillary pressure curve interpolation is shown with **Eq. 40.**

$$P_{cog} = f(\sigma) \cdot P_{cog}^{imm} \qquad \textit{(Eq. 40)}$$

$$f(\sigma) = \min\left[1, \frac{\sigma}{\sigma_0}\right] \qquad \textit{(Eq. 41)}$$

P_{cog}^{imm} is the capillary pressure corresponds to the reference surface tension σ_0.

When the surface tension σ equals zero, P_{cog} equals zero.

4.2.6 Diffusion Coefficient

In this study, the diffusion coefficients are estimated using the Sigmund correlation proposed by Sigmund (1976a; 1976b) shown with **Eq. 42** to **Eq. 51**.

$$D_{ij} = \frac{\rho_k^0 D_{ij}^0}{\rho_k} \cdot \left(0.99589 + 0.096016\rho_{kr} - 0.22035\rho_{kr}^2 + 0.032874\rho_{kr}^3\right) \quad \textit{(Eq. 42)}$$

$$\rho_{kr} = \rho_k \left(\frac{\sum_{i=1}^{n_c} y_{ik} v_{ci}^{5/3}}{\sum_{i=1}^{n_c} y_{ik} v_{ci}^{2/3}} \right) \quad \textit{(Eq. 43)}$$

$$\rho_k^0 D_{ij}^0 = \frac{0.0018583 T^{1/2}}{\sigma_{ij}^2 \Omega_{ij} R} \cdot \left(\frac{1}{M_i} + \frac{1}{M_j} \right)^{1/2} \quad \textit{(Eq. 44)}$$

$$\sigma_i = (2.3551 - 0.087\omega_i) \cdot \left(\frac{T_{ci}}{P_{ci}} \right)^{1/3} \quad \textit{(Eq. 45)}$$

$$\varepsilon_i = k_B (0.7915 + 0.1963\omega_i) T_{ci} \quad \textit{(Eq. 46)}$$

$$\sigma_{ij} = 0.5(\sigma_i + \sigma_j) \quad \textit{(Eq. 47)}$$

$$\varepsilon_{ij} = \sqrt{\varepsilon_i \varepsilon_j} \quad \textit{(Eq. 48)}$$

$$T_{ij}^* = \frac{k_B}{\varepsilon_{ij}} \quad \textit{(Eq. 49)}$$

$$\Omega_{ij} = 1.06306 (T_{ij}^{*\backslash})^{-0.1561} + 0.193 \exp(-0.47635 T_{ij}^*) + 1.03587 \exp(-1.52996 T_{ij}^*) + 1.76474 \exp(-3.89411 T_{ij}^*) \quad \textit{(Eq. 50)}$$

Lastly, the diffusion coefficient for component i in the mixture is calculated using an equation based on Wilke formula:

$$D_{ik} = \frac{1 - y_{ik}}{\sum_{j \neq i} y_{ik} D_{ij}^{-1}} \qquad \textit{(Eq. 51)}$$

As mentioned in numerous studies, the diffusion coefficients for the components are parameters subjected to adjustment during history matching. Therefore, the estimated diffusion coefficients only serve as a basis for future adjustments.

4.3 CO_2 Core Flood Experiments with Shale Cores

The core scale simulation in this study is based on the experimental data from two sets of experiments described in the work by Tovar *et al.* (2014). This section briefly presents the experimental equipment, materials, conditions, procedures and results.

Two experiments are performed using two sets of preserved sidewall cores from the same well in an unconventional play. The petrophysical properties and the saturations of the cores were not measured before the experiments to preserve its original conditions. However, since the cores are not stored in a pressurized environment, the fluids saturating the cores can be assumed as dead oil and water. The dimensions of the cores are summarized in **Table 1**.

	First Experiment		Second Experiment	
Core Number	1-1	1-2	2-1	2-2
Core Diameter, cm	2.53	2.53	2.53	2.52
Core Length, cm	3.97	3.48	3.62	3.29
Core Bulk Volume, cm^3	19.94	17.50	18.20	16.42

Table 1 – The dimensions of the cores used in the two experiments (Modified after Tovar *et al*. 2014).

To simulate the presence of a highly permeable fracture around the core, glass beads were packed outside the cores, for the purpose of allowing CO_2 to have direct contact with the cores. Two Berea sandstone cores were placed on each end of the set up to block the glass beads from entering the production tube. The core holder was then placed inside a water bath which circulates hot water to simulate the reservoir temperature. And, the assembly was mounted in a CT (computed tomography) scanner. The cores were kept horizontally during the experiment. The schematic of the experimental setup can be seen in Tovar *et al.* (2014).

The experiments were performed under constant pressure conditions where viscous displacement was absent. The first experiment was performed at 3000 psi at 150 °F, and the second experiment was performed at 1600 psi and 150 °F. Since the composition of the resident oil in the preserved cores was unknown at the time, one could only estimate the MMP. Periodic scanning of the cores with the CT scanner was performed throughout the experiment. The experiments typically last for two to three days, and production was allowed twice a day on average.

The CT images of the core reveled constant density/saturation/composition changes of the resident fluid during both experiments, which indicated CO_2 was constantly penetrating into the core throughout the process.

Final oil production volumes of 0.4 ml were recorded for both experiments. Based on the estimated original oil in place, the experiments yielded significantly high oil recovery.

This study follows the experimental work described in this section. The petrophysical properties of the cores and the fluid properties of the dead oil were evaluated after the experiments.

4.4 Experiment Modeling

The following sections include the description of the core flood experiment modeling. The first section describes the fluid model of the dead oil used in the experiment. The following section focuses on sensitivity analysis of grid selection and properties. The next section includes both 3D homogenous and heterogeneous models to validate the experiment and parameters. The last section shows the modeling of a lab scale huff n puff case which is different than the real experiment and the results are compared.

4.4.1 Fluid Model

Fluid property modeling is a critical part in reservoir simulation. Building a model that resembles the real fluid behavior is a key to obtain reasonable results. The fluid model used in this study was a characterized model based on the GC-MS analysis results. It was built with PVTsim Nova 1, which is a robust and user friendly software that allows the user to build the fluid model and perform various PVT simulations. In addition, PVTsim allows the exporting of the PVT files into different formats that are compatible with various commercial simulation platforms such as Eclipse, CMG, Prosper, Saphir, etc.

The following sections describe the fluid characterization, component lumping, model regression, and the simulated fluid properties.

4.4.1.1 Fluid Characterization

The dead oil sample from the same well where the preserved side wall cores were taken was used in the simulation of the laboratory experiments. The sample was analyzed with GC-MS (gas chromatography-mass spectrometry). A normalized weight percentage of each detected components were obtained from the analysis. A detailed chemical component list was determined as shown in **Table 2**.

Component	Mass Percent, %
Cyclohexane	4.318
Cyclopentane, 1,2-dimethyl	4.435
Heptane	3.28
Cyclohexane, methyl-	9.753
Cyclohexane, 1,3-dimethyl-	5.109
Octane	6.508
Cyclohexane, 1,1,3-trimeth	3.274
Nonane	4.495
Decane	6.701
Undecane	5.882
Dodecane	6.129
Tridecane	5.449
Tetradecane	5.284
Pentadecane	5.351
Hexadecane	4.433
Heptadecane	4.057
Octadecane	4.014
Nonadecane	3.298
Eicosane	3.225
Heneicosane	2.662
Docosane	2.344
Sum	100

Table 2 – Chemical composition of the dead oil and the corresponding normalized mass percentage obtained from GC-MS analysis.

4.4.1.2 Component Lumping

Pedersen *et al*. (2014) suggests lumping the components into three main categories: the defined components such as CO_2, N_2, H_2S, and C_1 to C_6; the C_{7+} fraction which are grouped based on boiling points; and a plus fraction which includes the heavy components that cannot be grouped into C_{7+} fractions. Since this study uses a dead oil sample starting from component C_6, the typical lumping schemes such as the one suggested by Pedersen *et al*. (2014) does not apply.

Based on the GC-MS results, the components were lumped into four pseudo-components including trace amount of CO_2 with mole fraction of 1E-6, which does not affect the oil properties as shown in **Table 3**. The lumping method was based on the weight-based lumping scheme suggested by Pedersen *et al.* (2014).

Component	Mole Fraction, %	Weight Fraction, %
CO_2	1E-6	3E-7
COMP1	33.18	21.79
COMP2	30.51	26.09
COMP3	22.90	28.10
COMP4	13.41	24.03

Table 3 – Weight-based pseudo-component lumping.

4.4.1.3 Fluid Model Regression

The PVT properties were calculated based on the cubic equation of state. The Equation of State (EOS) used was Peng-Robinson 1978 with Peneloux volume correction. For viscosity modeling, the Corresponding States Principle (CSP) method proposed was selected instead the Lohrenz-Bray-Clark (LBC) correlation. Although the LBC method is simple, consistent and fast computationally, it does not accurately predict the viscosity of a liquid (Yang *et al*. 2007). The CSP method gives better prediction for liquid viscosity, and therefore, was selected for this study.

Since limited experimental data was available for the oil sample, regression was performed based on the fluid density and viscosity at various temperatures. Parameters used for regression are critical pressure, critical temperature, acentric factor, molecular weight, and critical volume for viscosity calculations. Since COMP4 has the highest uncertainty due to the limitation of the characterized model built with PVTsim library and data obtained from Haynes (2015) and Yaws (2008), it was mainly targeted during regression.

Oil densities were measured using the Anton Parr DMA 4100 M Density Meter at atmospheric pressure. **Table 4** and **Fig. 8** show the density values from the experimental measurements as well as the simulated density values after model regression.

Temperature, °F	Experimental Density, g/ml	Simulated Density, g/ml
68	0.8518	0.8520
77	0.8484	0.8488
86	0.8448	0.8456
95	0.8412	0.8423
104	0.8376	0.8389
113	0.8341	0.8354
122	0.8306	0.8319
131	0.8271	0.8283
140	0.8235	0.8247
149	0.82	0.8209
158	0.8166	0.8171
167	0.8131	0.8132
176	0.8096	0.8093

Table 4 – Measured and simulated density of the dead oil at various temperatures.

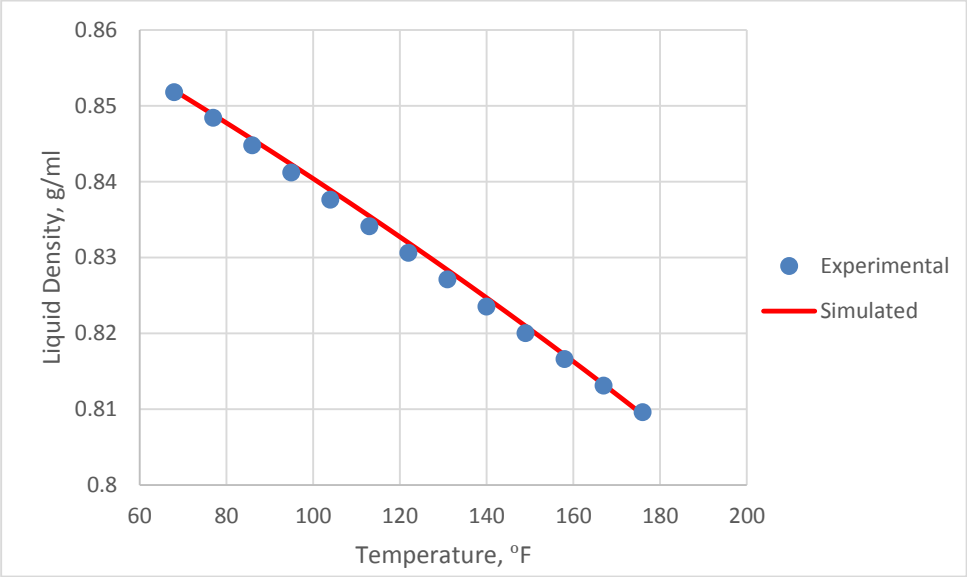

Fig. 8 – Measured and simulated density of the dead oil at various temperatures.

Oil viscosities were measured using the capillary viscometer with heated oil bath at atmospheric pressure. **Table 5** and **Fig. 9** show the viscosity values from the experimental measurements as well as the simulated viscosity values after model regression.

Temperature, °F	Experimental Viscosity, cp	Simulated Viscosity, cp
77	10.5	10.4919
92.3	8.3	8.2642
95	7.85	7.9340
104	6.9	6.9447
113	6.2	6.1037
122	5.4	5.3856
131	4.7	4.7699
140	4.3	4.2397
149	3.75	3.7814
158	3.4	3.3837

Table 5– Measured and simulated viscosity of the dead oil at various temperatures.

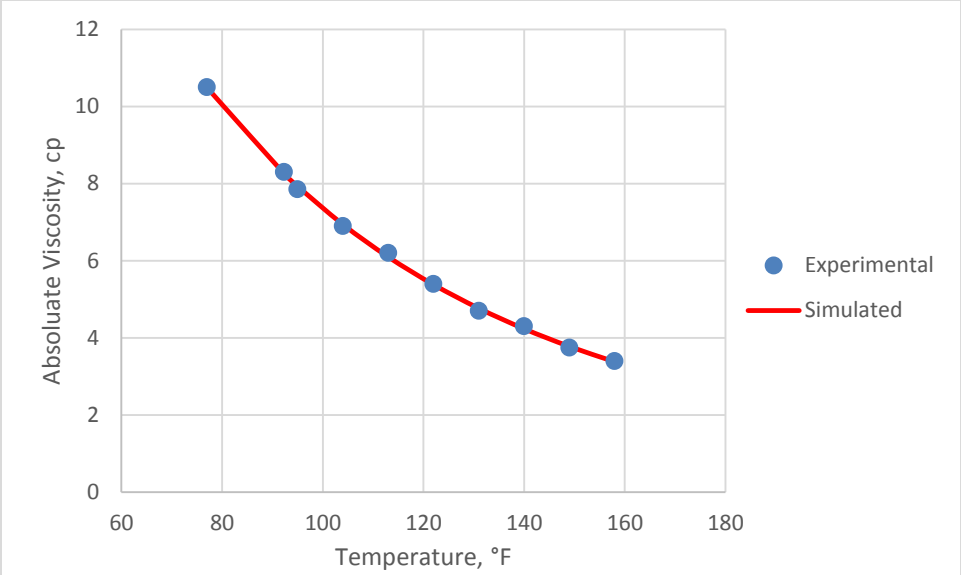

Fig. 9 – Measured and simulated viscosity of the dead oil at various temperatures.

After the regression, a dead oil model is obtained to be used in the simulation.

Table 6 summarized the properties of the fluid mode.

Component	Mole Fraction, %	Critical Pressure, atm	Critical Temperature, K	Acentric Factor	Molecular Weight, g/mol
CO_2	1E-6	72.80	304.20	0.225	44.01
COMP1	33.18	34.30	559.74	0.254	95.33
COMP2	30.51	23.97	593.36	0.399	124.12
COMP3	22.90	17.17	673.34	0.617	181.06
COMP4	13.41	14.74	634.14	0.719	259.99

Table 6 – Properties of the fluid model after regression.

4.4.1.4 Fluid Properties

The MMP and FCM were calculated with PVTsim. At 150 ºF, the MMP was determined at 1727 psi, and the FCM was achieved at 1934 psi. The MMP value is further confirmed with a simulated slim tube experiment. A 1D model with 200 cells was used. The transport mechanism was the moving excess model where the volume of each cell remains constant, and all excess gas and oil that exceed the original volume are transported to the next cell. And, if the oil volume becomes lower than the original volume, only the excess gas is being transferred. With constant pressure and temperature in each cell, after 1.2 PV of CO_2 injected, **Fig. 10** shows the MMP result calculated with the slim tube module in PVTsim, the result agrees with that estimated with the MMP module.

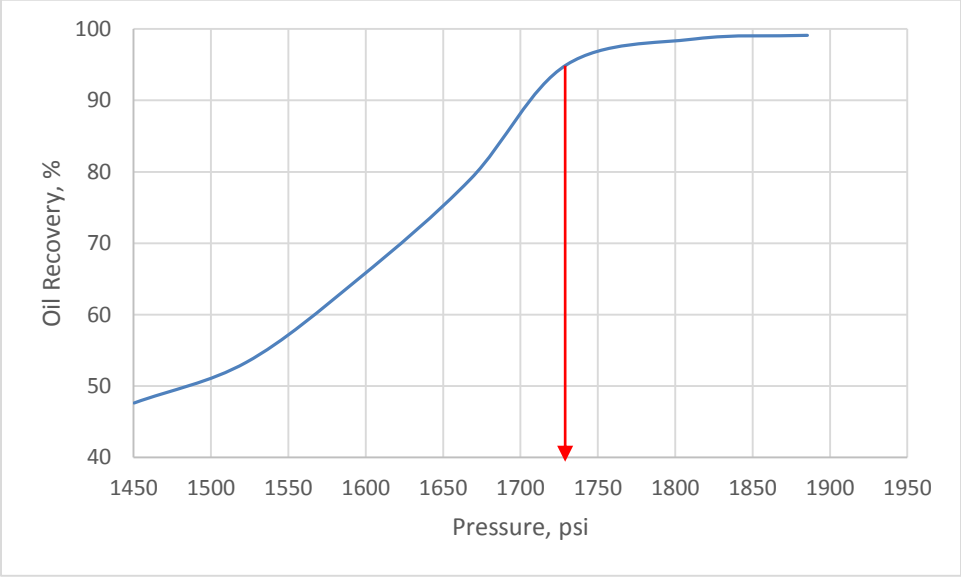

Fig. 10 – Simulated slim tube result at 150 ºF using PVTsim.

The density and viscosity of the fluid model at various temperatures after regression were listed in the previous section. During a CO_2 EOR process, oil volume expansion, density and viscosity reduction were the main recovery mechanisms as mentioned earlier. **Fig. 11** below shows the change in density when different mole fraction of CO_2 is mixed with the dead oil at 150 ºF and atmospheric pressure. The density displays a decreasing trend when more CO_2 is mixed with the oil.

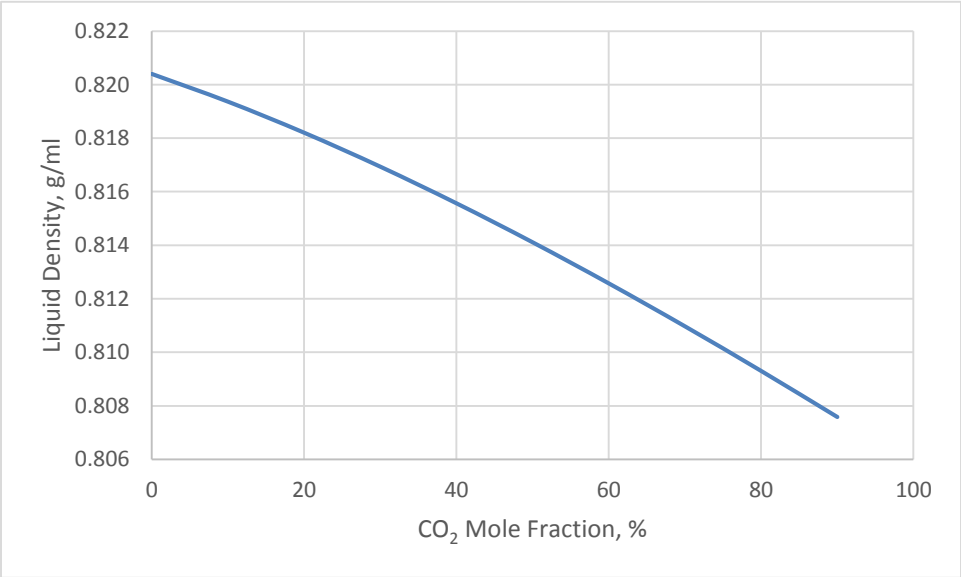

Fig. 11– Oil density change with different mole fraction of CO_2.

Viscosity on the other hand displays a more dramatic change compared with density when mixed with the oil as seen in **Fig. 18**.

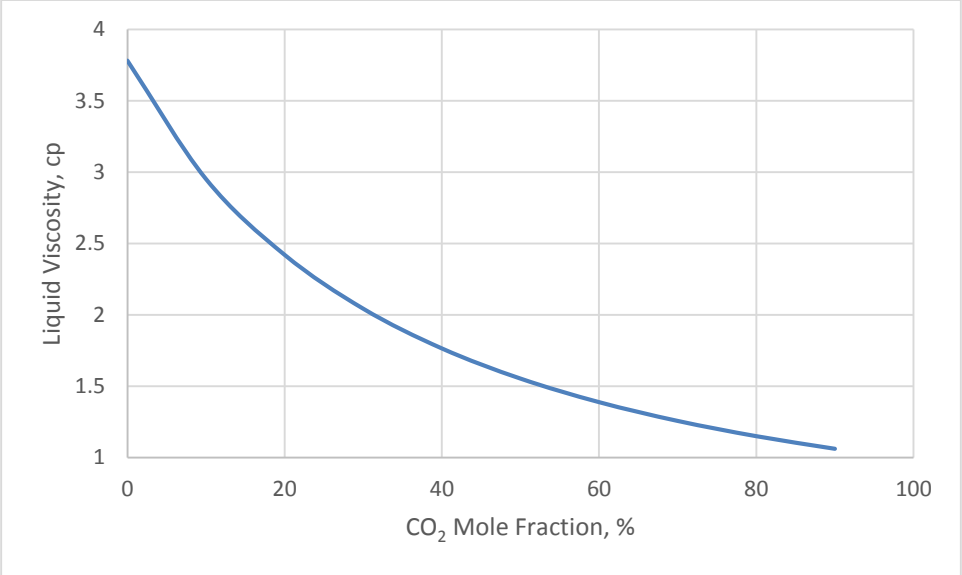

Fig. 12 – Oil viscosity change with different mole fraction of CO_2.

In addition to density and viscosity reduction, CO_2 also causes oil swelling as seen in **Fig. 13**, and when mixed at different proportions it results in changes in the saturation pressure.

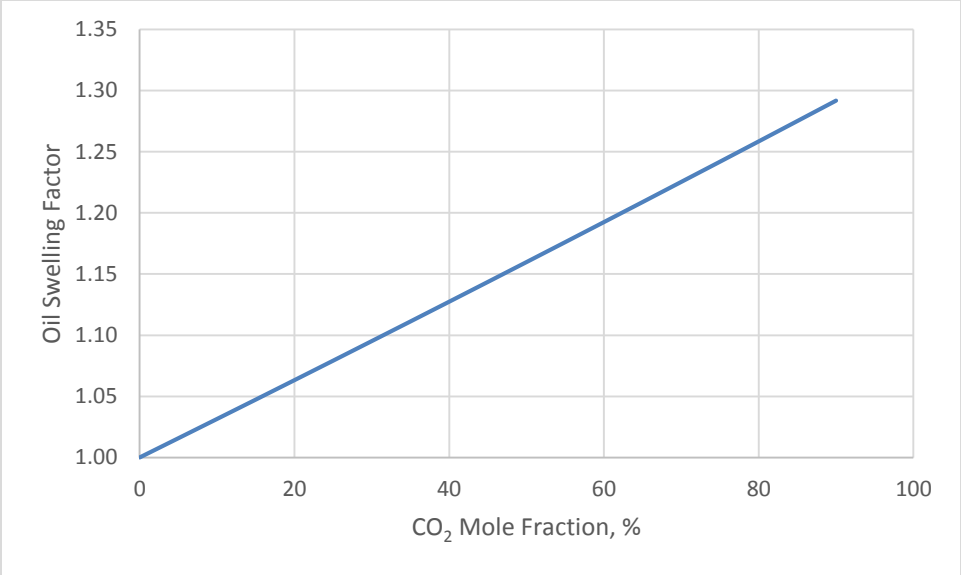

Fig. 13 – Oil swelling factor with different mole fraction of CO_2.

4.4.2 Experiment Model Grid and Property Sensitivity Analysis

To model the laboratory experiments, grid selection was explored in the next section. Then sensitivity analysis for different properties were performed in the following sections.

4.4.2.1 Grid Sensitivity

Since the experiment conducted by Tovar *et al*. (2014) described a 3D flow scheme, which included a radial flow around the core and an axial flow in the direction of the core face, a radial (cylindrical) grid is naturally suitable to be used in simulation. However, since the ultimate goal for core flood modeling is to incorporate heterogeneous property maps to imitate the images obtained from the CT scan, investigating the use of Cartesian grid was the main focus in this case. The diameter of

the core is 2.54 cm (1 in), and the length is 6.91 cm (2.72 in). Grid sensitivity analysis is done on three models with radial grids and two models with Cartesian grids, each of different degrees of refinement. The single porosity model was used in all cases, and the model is of the exact dimension of the real experimental setup as described by Tovar *et al*. (2014). **Table 7** below shows the dimension associated with the five grids being investigated. **Fig. 14** shows the graphic view of the three radial grid models and the two Cartesian grid models with different grid block dimensions.

Model	Grid Type	DR(DX)	Dθ(DY)	DZ	Single Matrix Block Dimension
Radial 1	Radial	11	10	12	0.127 cm x 36º x 0.691 cm
Radial 2	Radial	30	10	22	0.0635 cm x 36º x 0.3455 cm
Radial 3	Radial	60	36	50	0.03175 cm x 10º x 0.17275 cm
Cartesian 1	Cartesian	52	52	12	0.0508 cm x 0.0508 cm x 0.691 cm
Cartesian 2	Cartesian	52	52	32	0.0508 cm x 0.0508 cm x 0.23033 cm

Table 7 – Grid sensitivity on both radial and Cartesian grids with different degrees of refinement.

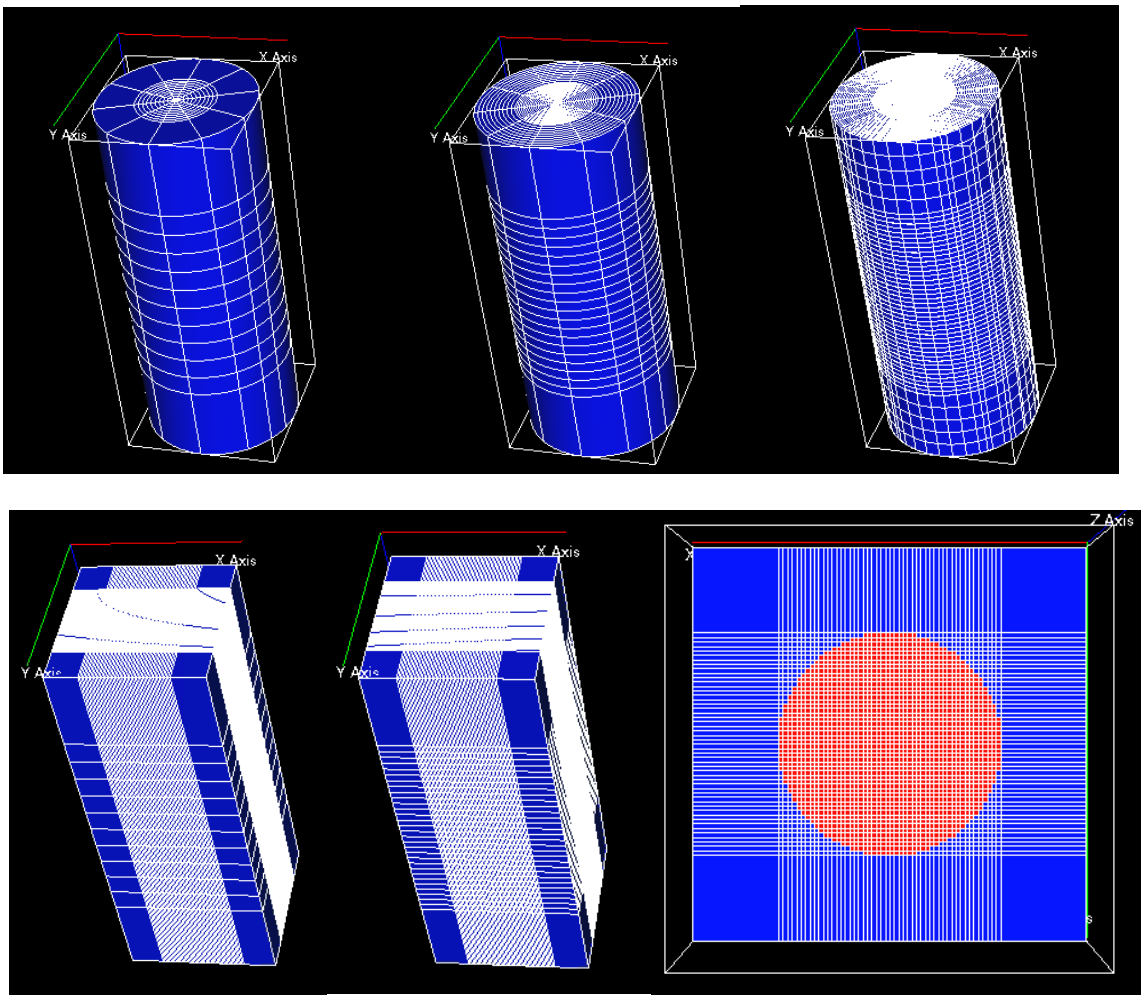

Fig. 14 – Grid sensitivity on both radial and Cartesian grids with different degrees of refinement.

The cores are assumed to be isotropic. The matrix and fracture properties are chosen based on literature review. The core used in the experiments conducted by Tovar *et al*. (2014) are from the upper part of the formation. According to the study of Sagar *et al*. (2010), out of the 796 samples they conducted measurements on, the average porosity is 5.7% with a standard deviation of 2.1%, which puts the porosity for this particular

shale in the range from 3.6% to 7.8%. The study conducted by Sigal (2013) also agrees with the results. An 8% porosity was chosen to be used in our synthetic model. The fracture porosity was set to be 45%. Permeability of the matrix was 100 nD. Water saturation was immobile at 10% for the core region. **Fig. 15** shows the cumulative oil production yielded from the grid sensitivity study.

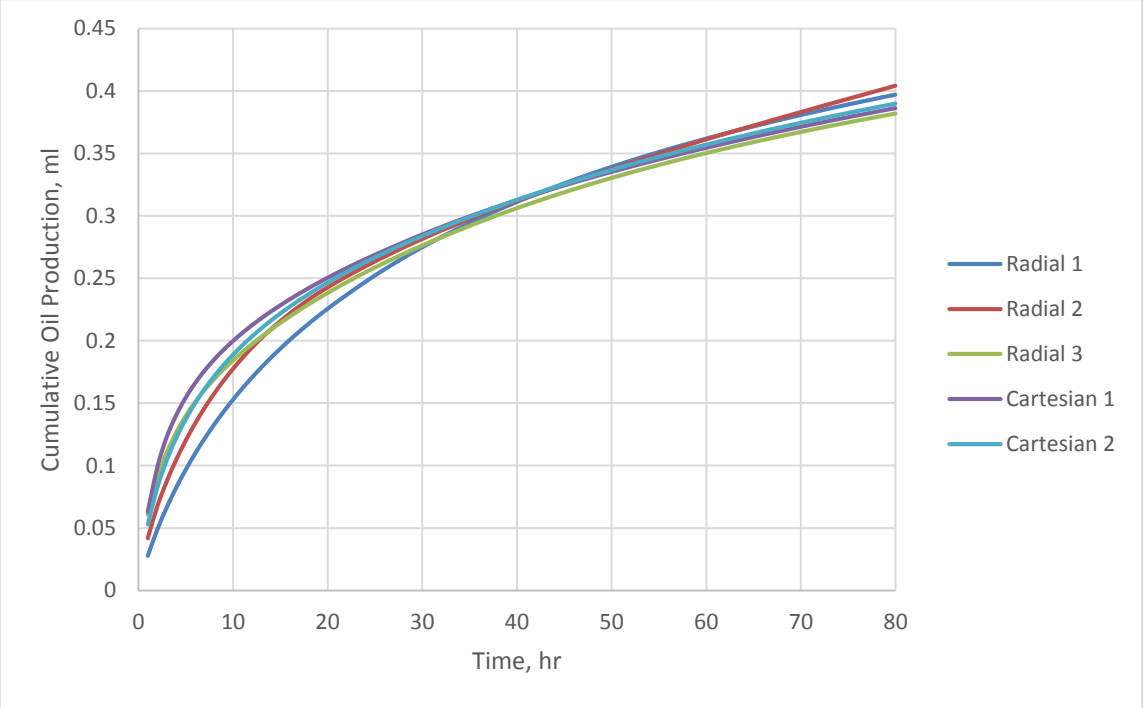

Fig. 15 – Grid sensitivity results for the five grids being investigated.

As seen is Fig. 15, although the models did not agree very well in the early times, the ultimate recovery yielded were fairly close. In addition, the Cartesian models gave

fairly close results to the radial models. To accomplish the ultimate goal of this study, Cartesian 1 grid, which agrees well with the radial models in both early and late time, is selected for the 3D modeling.

4.4.2.2 Property Sensitivity Analysis

To save computational time for the sensitivity analysis, a horizontal slice of the Cartesian core model was taken out for investigation. The slice model is shown in **Fig. 16**. It is more discretized both in the matrix and the fracture regions compared with the actual 3D model.

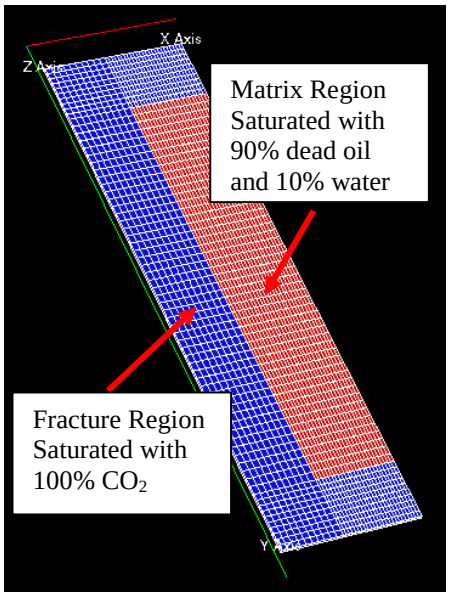

Fig. 16 – The slice model used for property sensitivity analysis. The red region represents the matrix, which is saturated with oil and water. The blue region represents the gas bearing fracture.

For all cases below, the conditions were the same as the conditions in experiment I, which are 3000 psi and 150 °F. Injectors were placed in the fracture region for pressurizing and pressure maintenance. Producers were not introduced at this point of the study. The cumulative oil production and oil production rate refer to the volume and the rate of oil being displaced from the matrix region into the fracture region. In addition, the initial conditions of the model were defined explicitly.

4.4.2.2.1 Matrix Permeability

4.4.2.2.1.1 Scenario 1

The matrix permeability values were changed for different cases. The first scenario considered only diffusion by setting the initial pressure for both the fracture and the matrix regions to 3000 psi (204 atm). This scenario eliminated the initial pressurizing process of the system using CO_2. The simulation time was 100 hours and the four pseudo-component fluid model was used. **Table 8** listed the different permeability scenarios and the corresponding recovery factors. Case 1 has considerably high permeability of 10 mD for the purpose of comparison. The cumulative oil production and production rate from the matrix into the fracture was plotted versus time as shown in **Fig. 17**.

	Permeability, mD	Recovery Factor, %
Case 1	10	14.46
Case 2	1.00E-03	14.46
Case 3	1.00E-04	14.46
Case 4	1.00E-05	14.46

Table 8 – Permeability values for different cases and the corresponding yielded recovery factors (Scenario 1).

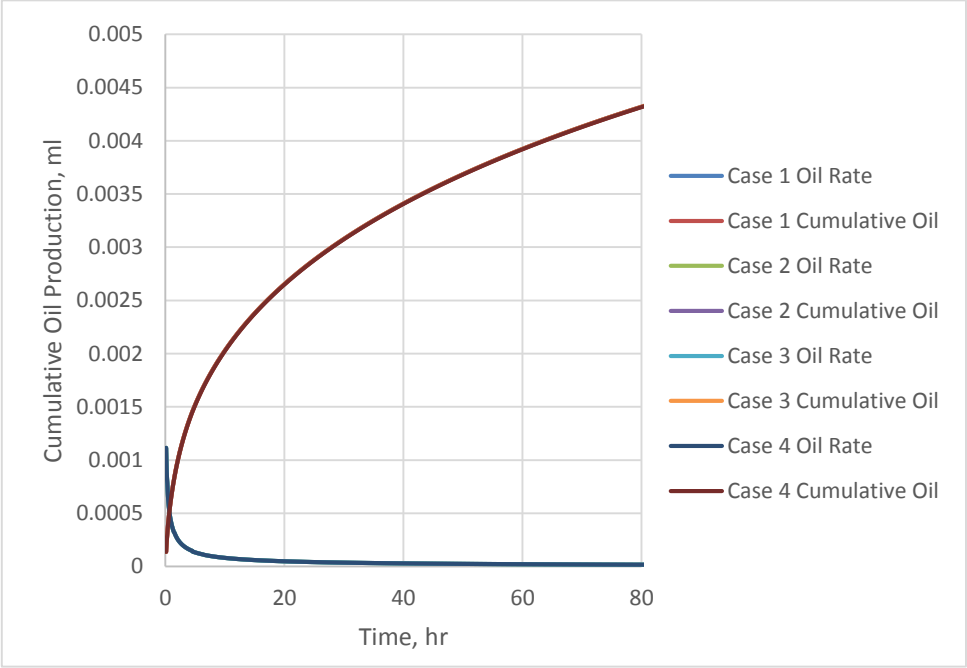

Fig. 17 – Cumulative oil production and oil production rate for cases with different matrix permeability values (Scenario 1).

As seen in Fig. 17, the recovery factors for all cases are equal despite the large permeability contrast. The result was expected because the production is only controlled by molecular diffusion, which is independent of pressure or bulk fluid movement. The

production rate in this case is only influenced by the chemical potential and the diffusion coefficient of each component, which are the same in all cases.

However, minor pressure variations in the matrix for the smaller permeability cases are observed as shown in **Fig. 18**. This is because the system pressure was initialized at 3000 psi (204 atm), and the fluids no longer behave as ideal fluids. Therefore, minor pressure variation inside the core can be observed although molar balance is maintained. However, one should note that the presence of this pressure variation can be masked by artificial convection when permeability is large enough, as mentioned in Hoteit (2013). The masking of the pressure variations can be observed in Fig. 18 with cases that have high permeability values. The significance of this numerical artifact depends on the case. For instance, in some single porosity simulation studies without proper cross-phase diffusion modeling, the observation of continuous CO_2 prorogation inside the matrix is resulted from this artificial convection or even gravity induced pressure gradient, which gives incorrect calculation.

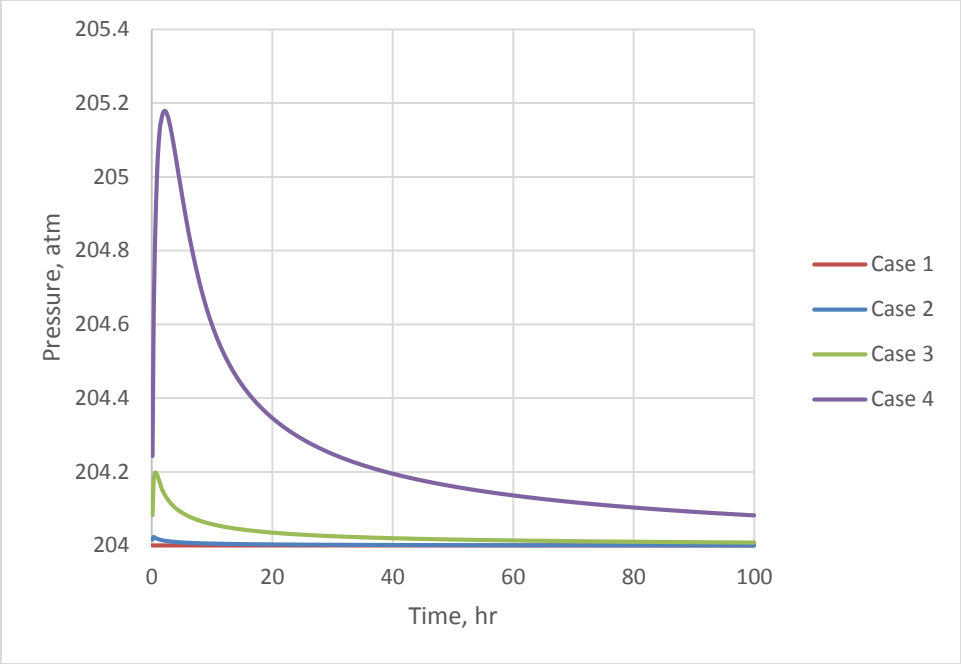

Fig. 18 – Average pressure in the core region over time (Scenario 1).

4.4.2.2.1.2 Scenario 2

During the actual experiment, the pressurizing process was necessary, and should be considered in the simulation. The models in scenario 2 described below were initialized at 14.7 psi (1 atm) in both the matrix and fracture regions. The system was then pressurized and maintained at 3000 psi with injectors. In this scenario, convection and diffusion both play parts in the mass transfer process. The significance of the two mechanisms differs based on the matrix permeability, which in turn affects the pressure in the matrix.

Table 9 shows the permeabilities and corresponding recovery factors. **Fig. 19** below shows the cumulative oil production for each case.

	Permeability, mD	Recovery Factor, %
Case 1	10	10.59
Case 2	1.00E-03	10.59
Case 3	1.00E-04	10.59
Case 4	1.00E-05	10.65
Case 5	1.00E-06	11.12

Table 9 – Permeability values and the corresponding recovery factors for cases with different matrix permeability values (Scenario 2).

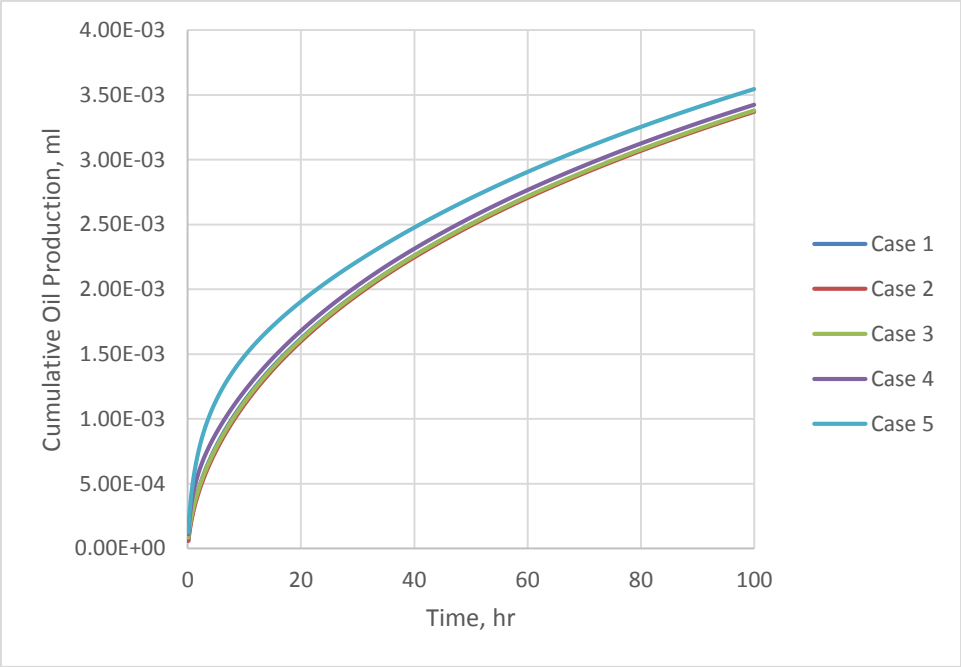

Fig. 19 – Cumulative oil production for cases with different matrix permeability values (Scenario 2).

The results from scenario 2 turned out to be counterintuitive. Case 5, which has the smallest permeability, yielded the highest recovery than the rest of the cases. Whereas the rest of the cases have similar production values close to that observed in scenario 1. In the cases where convection is included, pressure plays a significant role in determining recovery because it directly affects the chemical potential for each of the components. **Fig. 20** shows the average core pressure for all cases in scenario 2. Since the permeability differs, according to Darcy's law, the rate at which pressure builds up inside the core is directly proportional to the permeability value. As one can observe from Fig, 20, Case 5 has significantly lower pressure than the rest of the cases for approximately 40 hours inside the core region. Although the fugacity of a non-ideal liquid does not change much with pressure, it still has some effect. For Case 5, the fugacity of the fluid inside the core is less than that of the rest of the cases, whereas the fugacity in the fracture is the same. This fugacity gradient resulted in the higher mass transfer rate for Case 5 compared with the other cases. Again, since the fugacity of fluid does not change significantly with pressure, the increase in production is only minor.

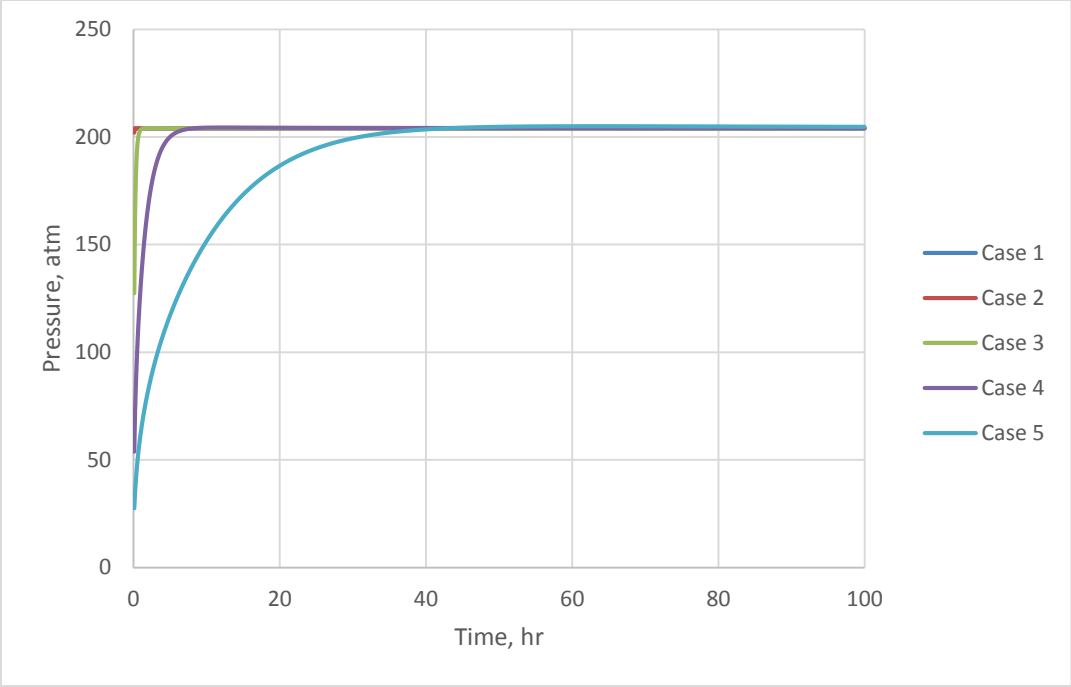

Fig. 20 – Average pressure in the core region over time (Scenario 2).

In addition, as mentioned in Eide *et al*. (2014), the concentration of a component is a linear function of the square root of time if the flow is dominated by diffusion. **Fig. 21** shows the oil production versus the square root of time. The early time shows a non-linear relationship between the two due to the initial convection caused by the pressure gradient between the fracture and matrix region. After that, a linear relationship can be observed, indicating diffusion is the dominate mechanism.

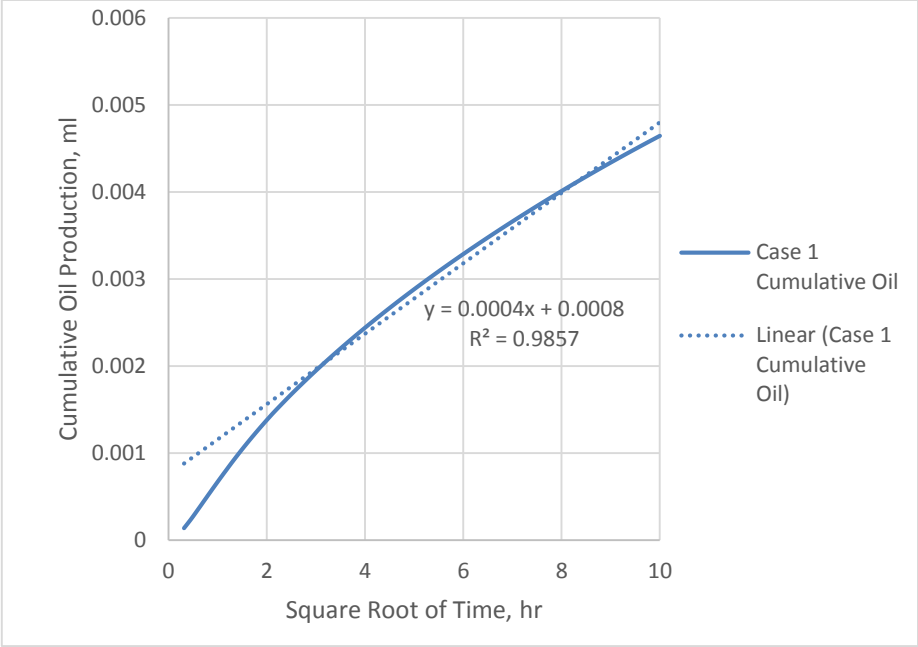

Fig. 21 – Production versus square root of time. The linear relationship represents diffusion dominate flow.

On the other hand, comparing Fig. 17 with Fig. 19, one can notice that the production of the pressurizing cases (scenario 2) are lower than the no convection cases (scenario 1). One possible explanation is the effect of the pressure variation inside the core mentioned earlier. The pressure of the core was higher in scenario 1, causing more oil to transfer into the fraction.

Overall, permeability of the matrix has only minor effects on oil recovery when diffusion is the dominating recovery mechanism. The study conducted by Vega *et al.* (2010) reached similar conclusion that heterogeneity has limited effects on cumulative recovery.

4.4.2.2.2 Matrix Porosity

The matrix porosity was changed for each case. Permeability for all cases were kept the same as 1E-4 mD and water saturations were 0.1. **Table 10** summarizes the three porosity scenarios and the corresponding recovery factor. **Fig. 22** is the cumulative production over time. Referring back to Eq. 5, porosity values are directly proportional to diffusion flux calculation. Physically, the higher contact area between CO_2 and the oil will result in higher flux. One would expect to observe an identical recovery factor from the three cases with different oil in place volume. However, since different porosity values slightly affected the pressure buildup inside the core due to the difference in the volume of fluid needs to be compressed, recovery factors differ slightly for the three cases.

In this section, the same diffusion coefficients were assumed for different porosity cases, which is incorrect. Section 4.4.2.2.6 will mention that the effective diffusion coefficient is also affected by porosity and tortuosity of the porous medium.

	Porosity, %	Recovery Factor, %
Case 1	12	9.76
Case 2	8	10.59
Case 3	4	11.22

Table 10 – Matrix porosity values and the corresponding recovery factors.

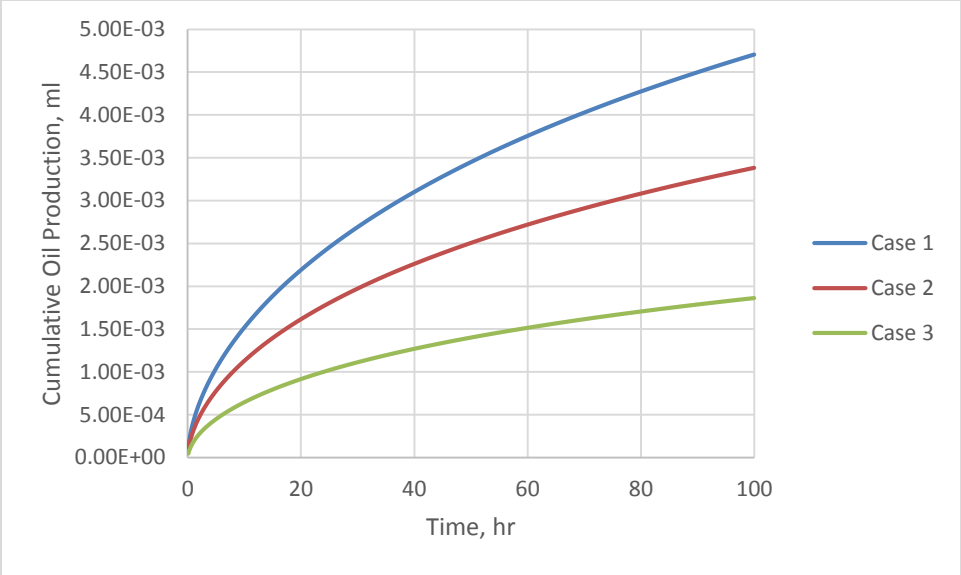

Fig. 22 – Cumulative oil production for cases with different matrix porosity values.

4.4.2.2.3 Fracture Permeability

The permeability of the fracture region was changed for two cases. The rest of the fracture and matrix properties were kept the same. **Table 11** and **Fig. 23** indicate that fracture permeability does not influence the mass transfer between the matrix and the fracture.

	Permeability, mD	Recovery Factor, %
Case 1	10000	10.59
Case 2	10	10.59

Table 11 – Fracture permeability values and the corresponding recovery factors.

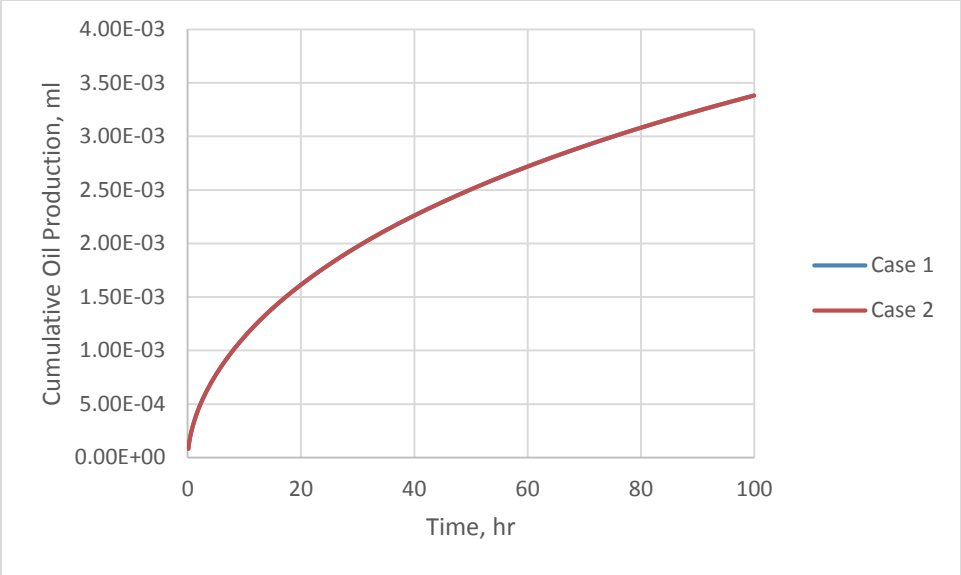

Fig. 23 – Cumulative oil production for cases with different fracture permeability values.

4.4.2.2.4 Fracture Porosity

Fracture porosity in case 2 was reduced to 20% compared with case 1. **Table 12** and **Fig. 24** show that the fracture porosity greatly affects the recovery factor from the matrix. Case 1 has larger production because it has higher CO_2 and oil volume ratio compared of 14 compared with that of case 2, which is 6. The chemical potential of CO_2 in case 1 is higher than that in case 2 because of the higher concentration, which resulted in larger production.

	Porosity, %	Recovery Factor, %
Case 1	45	10.59
Case 2	20	7.79

Table 12 – Fracture porosity values and the corresponding recovery factors.

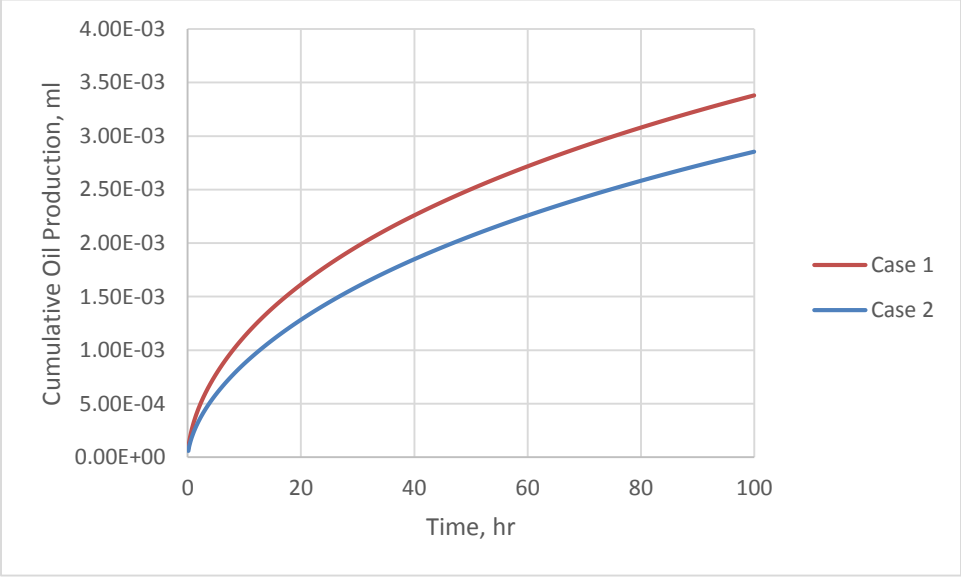

Fig. 24 – Cumulative oil production for cases with different fracture porosity values.

4.4.2.2.5 Water Saturation

Four cases with different water saturations were then investigated. All cases in this section have a porosity of 8% and a permeability of 1E-4 mD. As observed in **Table 13**, water saturation merely affected the ultimate recovery factor, although the volumes produced were different for the cases as seen in **Fig. 25** since the HCPV were different. The mere differences in the recovery factor for the cases are most likely due to the differences in the compressibility of water and oil and CO_2 being soluble in water. In

addition, no water was produced into the fracture for all cases in the simulation, which agrees with the experimental observation.

	Water Saturation, %	Recovery Factor, %
Case 1	10	10.59
Case 2	20	10.62
Case 3	30	10.65
Case 4	40	10.66

Table 13 – Core region water saturation values and the corresponding recovery factors.

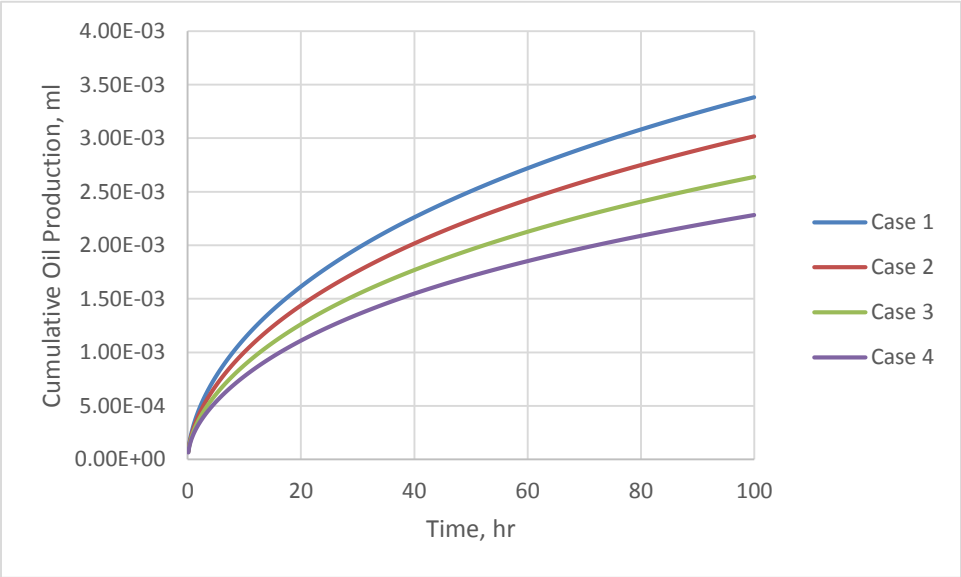

Fig. 25 – Cumulative oil production for cases with different water saturation values.

4.4.2.2.6 Diffusion Coefficient

The diffusion coefficients for each component in the mixture were calculated using the Sigmund correlation as mentioned in Section 4.2.6. They were then corrected with **Eq. 52** to account for the effects of tortuosity and porosity.

$$D_{i,eff} = D_i \cdot \phi^{m-1} \qquad \textit{(Eq. 52)}$$

Where

m is the cementation factor ranging from 1 to 2.

The effective diffusion coefficient after correction are calculated and listed in **Table 14**. Corrections are made using a porosity of 8% and a cementation factor of 2.

Component	CO_2	COMP1	COMP2	COMP3	COMP4
Gas, cm^2/hr	8.69E-04	4.28E-05	3.86E-05	2.72E-05	2.04E-05
Oil, cm^2/hr	2.96E-04	3.52E-05	3.26E-05	2.62E-05	2.05E-05

Table 14 – Diffusion coefficient calculated with the Sigmund correlation with correction.

For all cases below, a porosity of 8%, permeability of 1E-4 mD and water saturation of 0.1 were used. Diffusion coefficients were deactivated in the first case as shown in **Table. 15**. In case 1, only shallow CO_2 penetration into the core was observed in early time, and no hydrocarbon was produced from the matrix. The observation from case 1 not only proves that the mass transfer mechanism is diffusion, it also shows that oil swelling has little contribution in the oil recovery process, which agrees with the

conclusion made by Hawthorn *et al.* (2013). The third case used the diffusion coefficient listed in Table 14. The second case and fourth case used diffusion coefficients multiplied by a factor. As observed in Table 15 and **Fig. 26**, increasing the diffusion coefficients significantly incases the recovery factor.

	Diffusion Coefficient, cm^2/hr	Recovery Factor, %
Case 1	No Diffusion Coefficient	0
Case 2	Diffusion Coefficient X 0.1	3.43
Case 3	Diffusion Coefficient	10.59
Case 4	Diffusion Coefficient X 10	21.81

Table 15 – Diffusion coefficient values and the corresponding recovery factors.

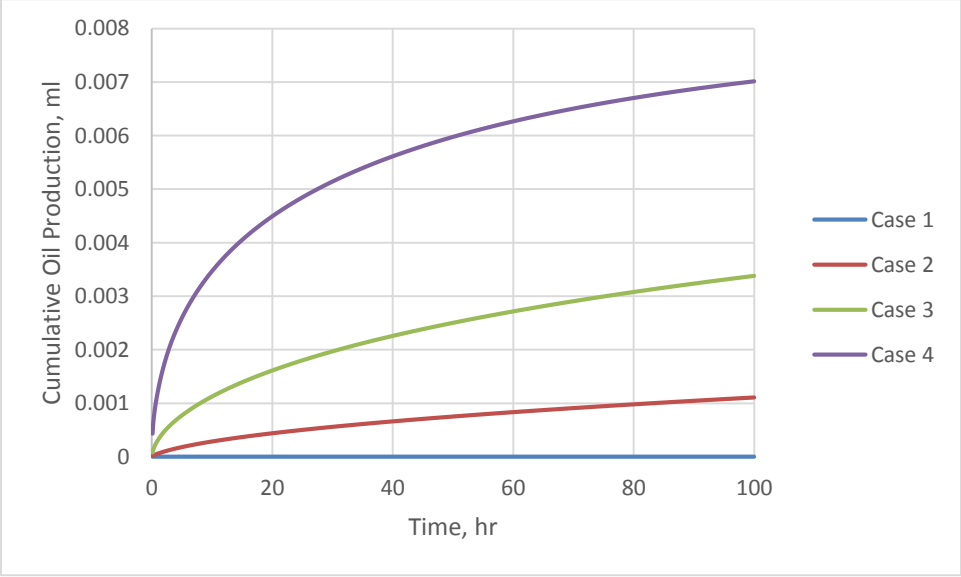

Fig. 26 – Cumulative oil production for cases with different diffusion coefficient values.

4.4.2.2.7 Pressure

At 150 ºF, the pressure was altered for the three cases. The MMP of the fluid system was determined to be 1727 psi. Therefore, case 1 and case 2 were run at 3000 psi and 1600 psi respectively, which are the same as the pressures used in the two experiments, resulting in a miscible and an immiscible case. Case 3 was run at pressure of 1800 psi, which is slightly above the MMP for the purpose of comparison. As shown in **Table 16** and **Fig. 27**, the miscible cases gave higher production than the immiscible case. This is because of the higher solubility of CO_2 in oil, as well as the more pronounced component stripping for the miscible cases. However, one can notice the increase in production in case 1 compared with case 2 were only two percent. As discussed earlier, the main mechanism for mass transfer occurring between the matrix and fracture is diffusion for the experimental setup. For a diffusion case, higher pressure would result in better CO_2 solubility in oil, which contributes to the increase in recovery. Furthermore, comparing case 1 with case 3, increasing the testing pressure from 1800 psi to 3000 psi only resulted in an additional recovery of one percent, whereas in case 2 and case 3, an additional of approximately one percent recovery was achieved by an increase the pressure by only 200 psi. In conclusion, similar to that of a conventional flooding scheme, increasing pressure above the MMP does not significantly increase recovery.

	Pressure, psi	Recovery Factor, %
Case 1	3000 (Miscible)	10.59
Case 2	1600 (Immiscible)	8.79
Case 3	1800 (Miscible)	9.66

Table 16 – Pressure values and the corresponding recovery factors for different cases.

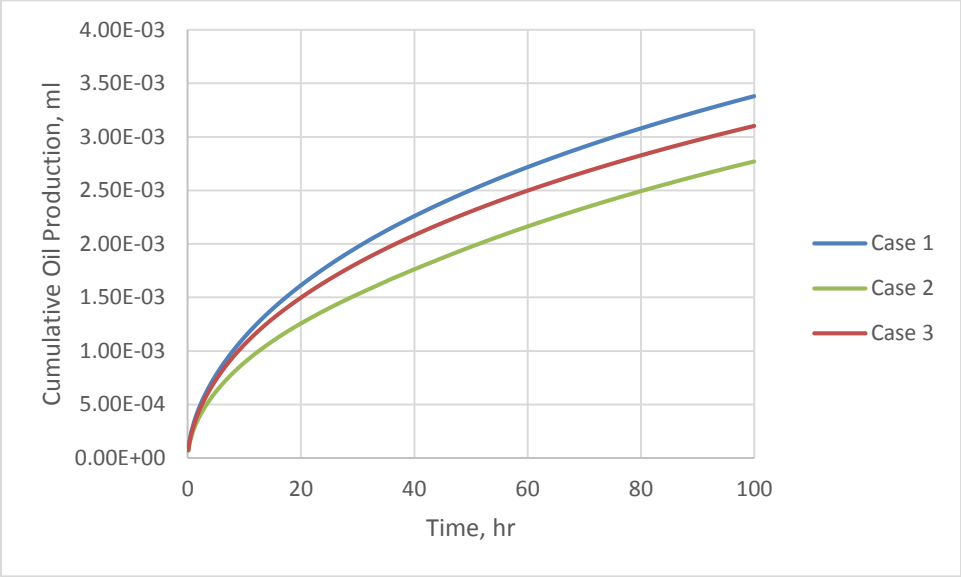

Fig. 27 – Cumulative oil production for cases with different pressure values.

4.4.2.2.8 Capillary Pressure for the Immiscible Case

Since for immiscible cases, the oil and gas capillary pressure will not be scaled down to zero, different capillary pressure schemes were investigated. Three sets of oil and gas capillary pressure curves were tested. They were arbitrarily defined as shown in **Fig. 28** at different ranges since there is no knowledge of the real capillary pressure. This

study is similar to that of Fai-Yengo *et al.* (2014). The results are shown in **Table 17** and **Fig. 29**.

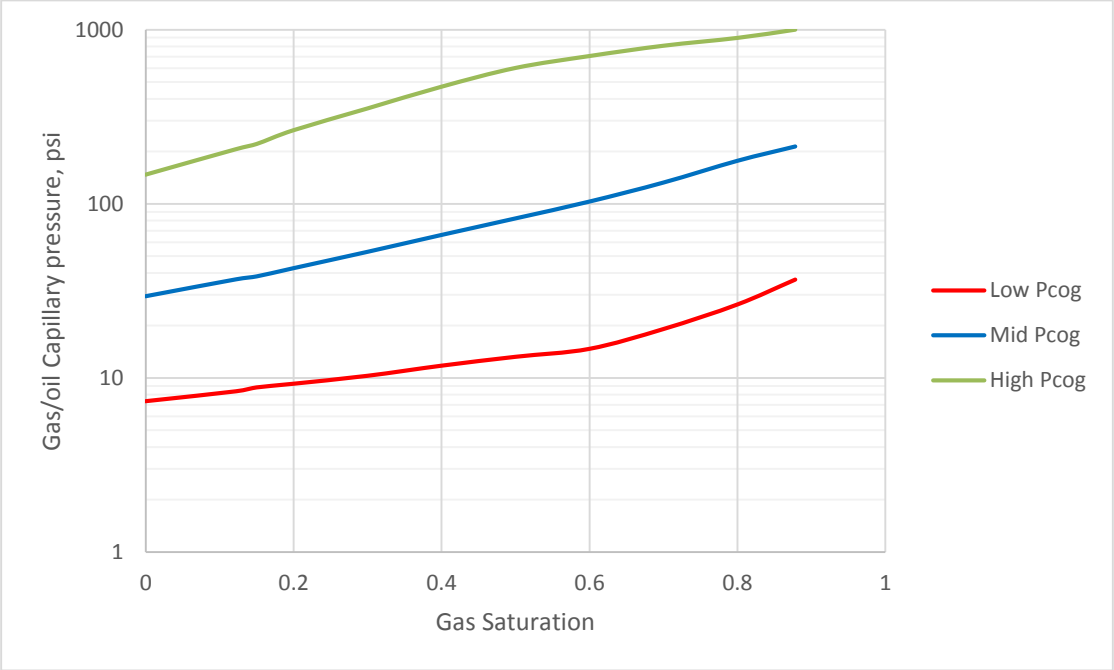

Fig. 28 – Three sets of capillary pressure curves representing low, mid and high ranges.

	Capillary Pressure Range	Recovery Factor, %
Case 1	Low	8.79
Case 2	Mid	8.79
Case 3	High	8.82

Table 17 – Capillary pressure ranges and the corresponding recovery factors for different cases.

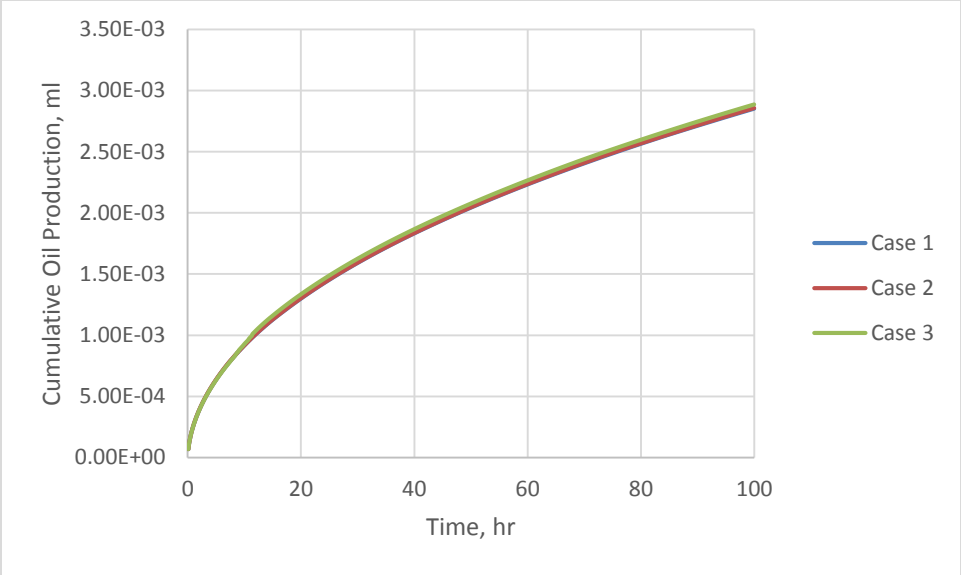

Fig. 29 – Cumulative oil production for cases with different capillary pressure curves.

Fig. 29 shows that capillary pressure has no effect in oil production. A similar conclusion was reached in the study done by Fai-Yengo *et al*. (2014). Their interpretation of the results was that the hydrocarbon production from the matrix into the fracture was mainly in the gas phase, which holds true in this study. In addition, since large mole percent of CO_2 is required to flash the oil into gas phase due to the low saturation pressure, the oil saturation inside the core does not change significantly in this study, which means capillary pressure does not have a significant change in the majority of the grid blocks.

4.4.3 Experiment I – Homogenous 3D Model

In this section, a 3D homogenous model was used to simulate experiment I. The grid used was Cartesian 1 mentioned in Section 4.4.2.1. Experiment I was performed

under 3000 psi at 150 ºF. For the particular fluid occupying the core, this pressure is above FCM pressure. CO_2 and oil will mix at any proportion when in contact, and the resulting mixture is a single phase fluid. Three cases were investigated for the homogenous 3D model.

In case 1, only soaking was considered. The pressure in the fracture region was maintained at 3000 psi with injectors. And producers were not introduced in this case. The volume of produced hydrocarbon was measured based on the amount of oil flowing from the matrix region into the fracture region.

Case 2 followed the procedures used during the actual experiment I. Producers were introduced in the fracture region. There were six cycles of soaking and producing. Each cycle consisted of 12 hours of soaking period and 1 hour of production. During the production period, the injectors and the producers were all opened, with the producers producing at 3000 psi and injectors injecting CO_2 at 3050 psi with a surface volume constraint of 100 ml/hour.

For the third case, six cycles of huff n puff were considered. However, since the injectors and producers are on the opposite sides of the cores, it is still not the conventional huff n puff scheme. In this case, 12 hours of soaking and 1 hour of production were modeled as well. Different than case 2, during the production time in case 3, the injectors were shut, and the producers were producing at a bottom-hole pressure constraint of 2800 psi.

One of the major issues when using compositional simulator to model molecular diffusion processes in tight rocks is the numerical instability, especially on a fine-scaled

core level. The large changes in pressure and composition can cause a tremendous amount of material balance errors. One solution is to reduce the initial time step until it stabilizes, which results in large computational time. In the simulations described in this section, small initial time steps in the range of 1E-10 hours were used. In addition, when initializing the model, pressures in the matrix and fracture regions were always set equal to 14.7 psi. The system was then pressurized altogether using injectors that inject at acceptable flow rates with a 3000 psi bottom-hole pressure constraint. This approach significantly improved the numerical stability, and at the same time, mimicked the real experimental procedures.

4.4.3.1 Results and Discussion

The model was built vertically instead of horizontally as in the experiment. Therefore, gravity effect was investigated. By inspecting the simulation result images from all three cases, gravity only affected the oil distribution in the fracture region, the amount of CO_2 penetration and oil saturation were symmetrical in the top and bottom slices inside the matrix region. **Fig. 30** below shows the mole fraction profile for COMP2 at 10 hours. Since the mole fraction inside the fracture region for COMP2 is very small in comparison to CO_2, the figure on the right shows the mole fraction of COMP2 at 10 hours in a log scale, which clearly shows the gravity effect in the fracture region. In addition, the slices closer to the two ends of the core observed lower COMP2 mole fraction than the slices in the middle section of the core because these slices were affected by both radial and axial flows.

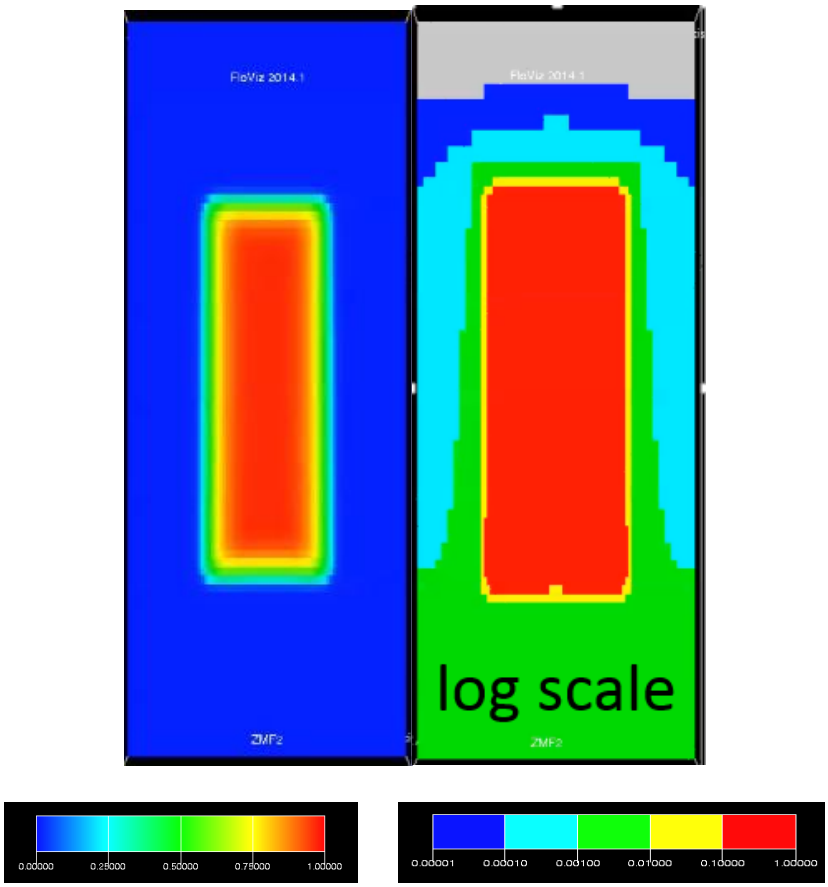

Fig. 30 – COMP 2 mole fraction profile at 10 hours. The log scaled image shows the effect of gravity on the oil distribution in the fracture region.

Fig. 31 below shows the cumulative oil production from the matrix into the fracture for the three cases. The experiment I scenario has slightly higher recovery than the soaking only case. This is because during the production period, the hydrocarbons that migrated from the matrix into the fracture were produced out from the producers, and more CO_2 was injected from the injector into the fracture. This process raised the CO_2 concentration inside the fracture region as well as the chemical potential. Therefore, higher diffusion influx occurred during this "flushing" period in response to this change.

Comparing experiment I simulation with the huff n puff scenario, one can observe a noticeable increase in production for the huff n puff case. This is because in the huff n puff case, the production occurred at 200 psi below the original system pressure. This pressure drawdown encouraged more hydrocarbon to flow from the matrix into the fracture by convection.

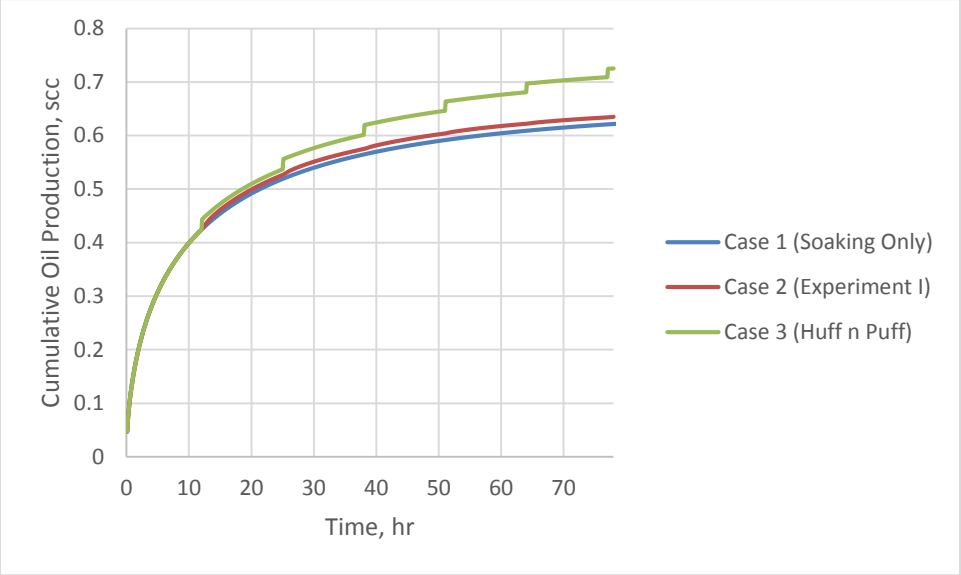

Fig. 31 – Cumulative oil production from the matrix into the fracture for the three cases.

Since the experiment I and huff n puff cases both have producers, the cumulative oil produced from the producers are shown in **Fig. 32**.

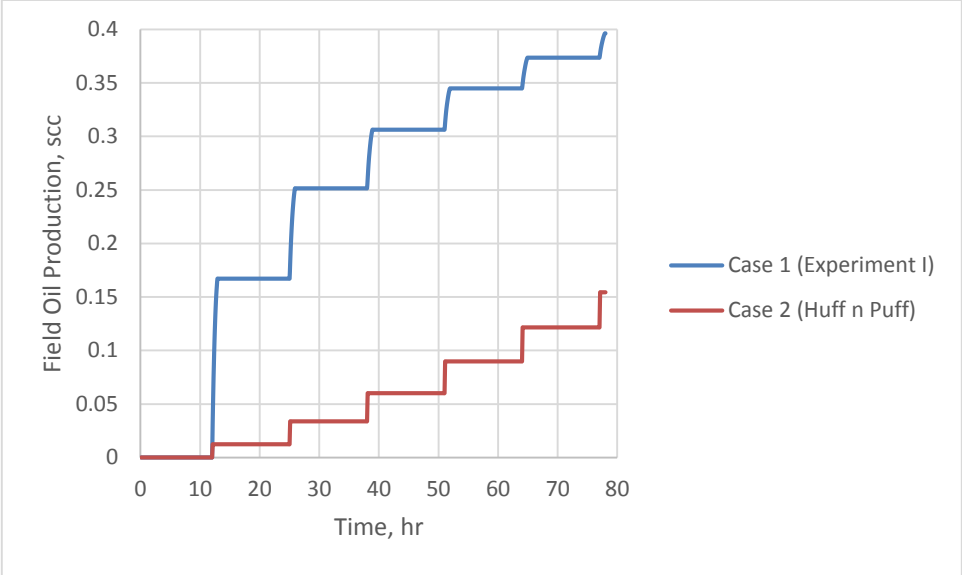

Fig. 32 – Cumulative oil production from the system (matrix and fracture) into the producers.

The huff n puff case displayed 2.7 times lower production than the experiment I scenario despite the higher production from the matrix into the fracture as observed in Fig. 31. This is because during experiment I, fresh CO_2 was injected into the fracture region during production time, which swept the hydrocarbon to the producers by viscous displacement (although most of the hydrocarbon was in the gas phase due to the comparably lower concentration than CO_2). In addition, one may notice in both experiment I and huff n puff cases, the volume of oil produced from the producers were lower than the volume of oil produced from the matrix into the fractures. In the experiment I case, the production from the producer was around 64.5% of the oil existed in the fracture. This is because only 0.91 PV of CO_2 was injected during the one hour

production period. Therefore, although it is obviously miscible flooding, the production of oil cannot reach 100% from the fracture into the producers.

On another note, **Fig. 33** shows the molar fraction in the exported oil for each individual oil component, namely COMP1, COMP2, COMP3, and COMP4. The properties of the components can be found in Section 4.4.1.3. Similar to a miscible CO_2 flooding scheme, the "lighter" components have the highest total production volume. This is the result of the lighter components having higher diffusion coefficients, and also easier to be vaporized into gas phase by CO_2. The "lighter" component is a relative term since the lightest component in this study is C_6.

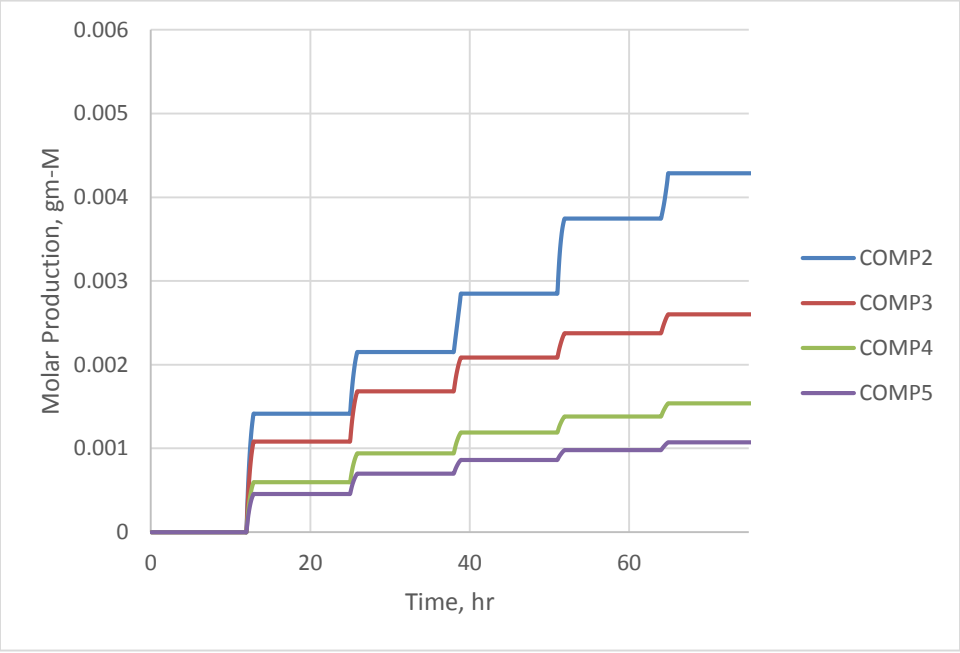

Fig. 33 – Molar fraction of each hydrocarbon components in the exported oil.

Lastly, although the production resulted from the experiment I case was higher than the huff n puff scenario, the amount of CO_2 consumed during experiment I was also significantly higher. **Fig. 34** below shows the comparison of the CO_2 production volume for both cases. Experiment I case produced 22 times more CO_2 volume along with the hydrocarbon compared with the huff n puff case.

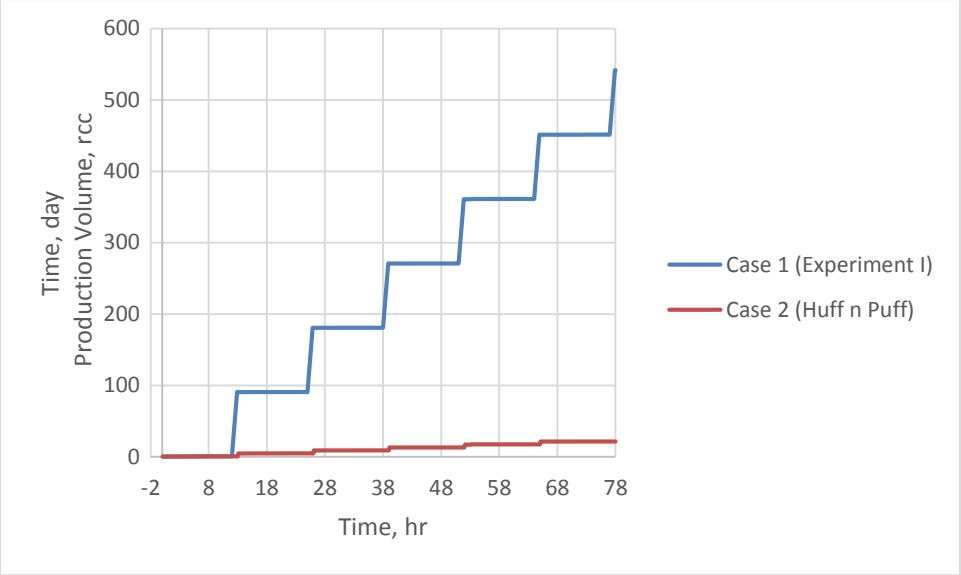

Fig. 34 – CO_2 production volume from the producers for case 1 and case 2.

In conclusion, the experiment I scenario produced 2.7 times more hydrocarbon than the huff n puff scenario. However, the GOR for experiment I was 8.3 times higher compared with the huff n puff scenario. Although this difference might not seem important in a laboratory scale study, it will be more pronounced in a field case.

4.4.3.1.1 Sensitivity Analysis of Soaking Time

As one can observe from Fig. 32, the production rate decreased as more cycles were performed. This indicated the reduced efficiency of cyclic injection over time because it takes longer for CO_2 to reach deeper into the core. The following two cases compared the effect of soaking time. The first case is the experiment I scenario, where six cycles of 12 hours of soaking were simulated. The second case followed the injection and production schemes of experiment I, except the cycle number was reduced to three cycles, and the soaking time in each cycle was increased to 24 hours. Production times were kept the same for both cases as 1 hour. The two cases were run for 78 and 75 hours, respectively. **Fig. 35** below displays the cumulative production. As one can see, although the decreasing trend of production rate can still be observed, with the longer soaking time during each cycle, CO_2 was allowed more time to penetrate inside the core, resulting in higher oil recovery.

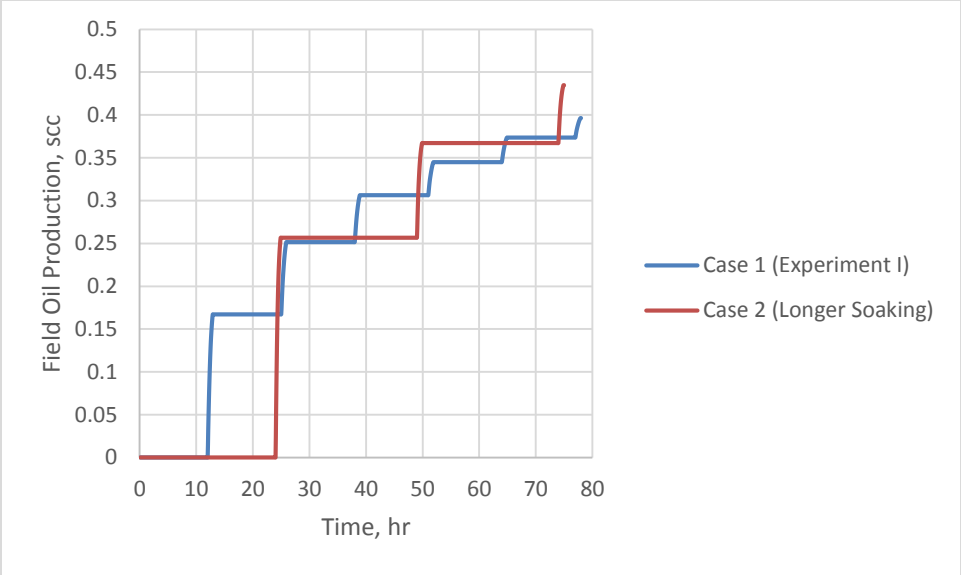

Fig. 35 – Cumulative oil production from the producers for cases with different soaking times.

4.4.4 Experiment I – Heterogeneous 3D Model

Referring to Tovar *et al.* (2014), the cores used in experiment I have very distinguished features. There were visible bedding planes on the core samples. From the CT images obtained during the experiment, changes in density mostly occurred along the bedding planes and the rest of the core observed very minimal or no change in CT number. Changes in CT number could be regarded as the only indication for the presence of CO_2, because either CO_2 adoption or mixing with the oil phase would cause potential density changes. On the other hand, there are three reasons for no density changes. One is there is no oil in the regions, which means the pores are filled with water, and the density change of water when CO_2 is dissolved in it is negligible. The second reason is the regions are isolated, which means CO_2 cannot reach those areas.

And, the third reason is the porosity is zero. The first and second reasons are most likely to be the case in experiment I. However, since defining a saturation map purely based on the CT images is not practical and does not add any values, the voxels with zero delta CT values are defined with very small porosity values of 0.5%. In future studies where the process of CO_2 diffuses through the water phase and recovers the trapped oil is being modeled, defining a saturation map becomes necessary.

4.4.4.1 Property Determinations

In this part of the study, co-kriging was used to aid in the process of defining the property maps. Various realizations were made. The diffusion coefficients used were altered by factors based on the calculated diffusion coefficients with the Sigmund correlation shown in Table 14. The goal of picking the appropriate porosity distribution is to match the ultimate 4 ml production with the least need of changing the diffusion coefficients. **Fig. 36** shows a sample slice of the porosity map used in the simulation. The diffusion coefficients used are listed in **Table 18**.

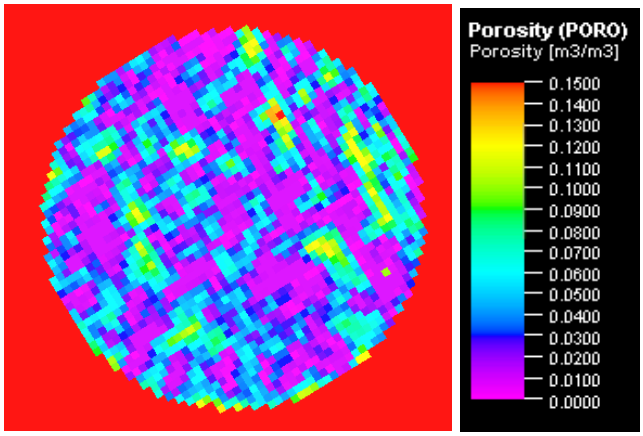

Fig. 36 – Sample porosity map for experiment I simulation.

Component	CO_2	COMP1	COMP2	COMP3	COMP4
Gas, cm^2/hr	1.04E-03	5.14E-05	4.63E-05	3.26E-05	2.45E-05
Oil, cm^2/hr	3.55E-04	4.22E-05	3.91E-05	3.14E-05	2.46E-05

Table 18 – Diffusion coefficients used to match the ultimate recovery volume.

After obtaining a porosity value for each grid block, the permeability value was determined based on porosity using the correlation proposed by Sigal (2002).

$$k = 60 r_{eff}^2 \phi^m \qquad \textit{(Eq. 53)}$$

where

r_{eff} is the effective pore throat size in micron,

φ is porosity,

m is the cementation factor, which is chosen to be 2 in this study.

Based on the study by Sigal (2013), the effective pore throat size for the particular type of rock that is similar to the one in this study measured with mercury injection was approximately 0.001 micron. Water saturation of the core was explicitly assigned at an immobile value of 0.1.

After obtaining the above properties, a fine micro scaled core model was built to mimic experiment I. The grid used was Cartesian 1 shown in Table 7. Property maps were input for the matrix grid cells. The model contains two saturation regions with individually assigned relative permeability and capillary pressure data. Injectors and producers were placed at each end of the model, and the well schedule was the same as the one described in Section 4.4.3. The condition of the simulation is at 3000 psi and 150 °F.

4.4.4.2 Results and Discussions

Fig. 37 below shows the oil density change inside the core over time. The slice is the same slice as shown in Fig. 36.

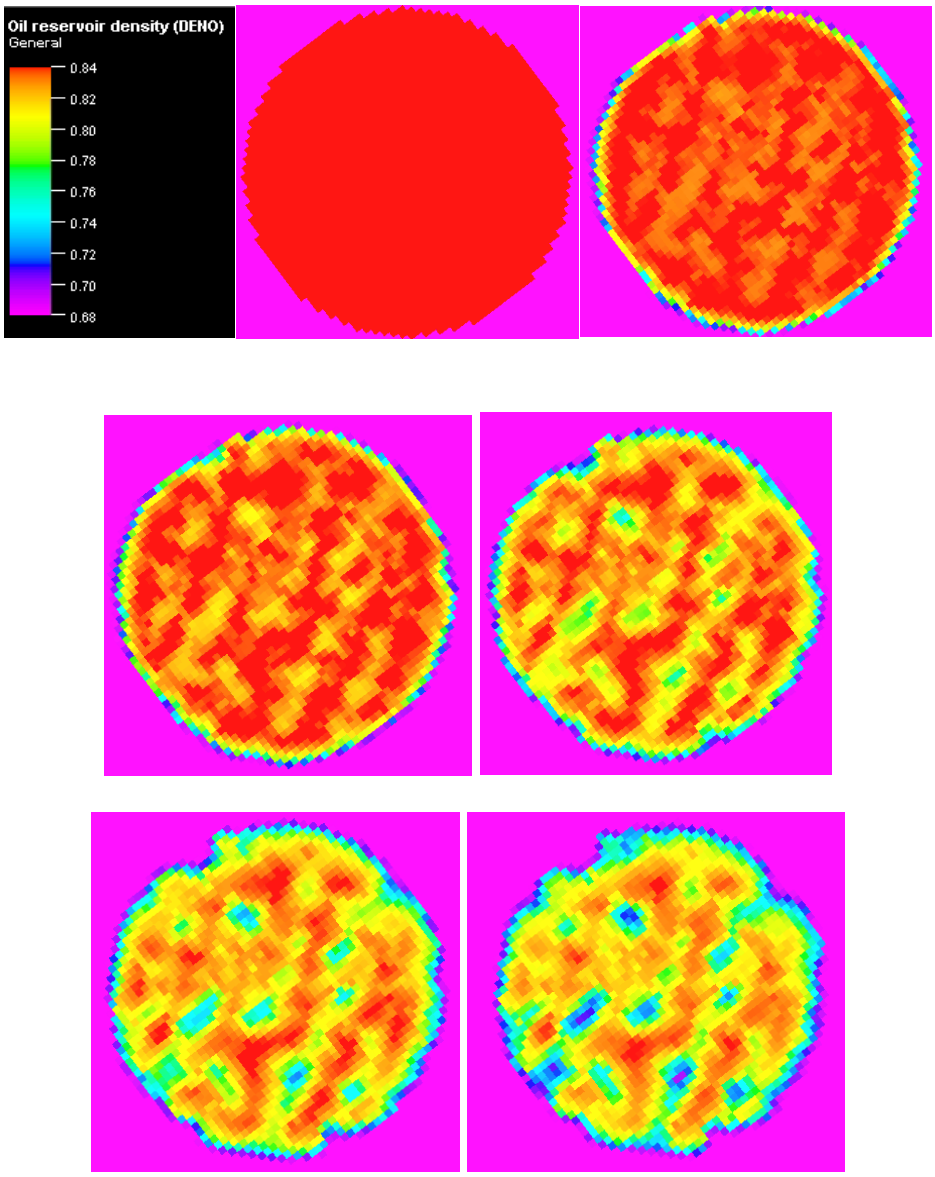

Fig. 37 – Oil density change for the experiment I 3D heterogeneous model at time 0hr, 5hr, 10hr, 24hr, 48hr, and 72hr.

As shown in Fig. 37, the rate at which oil density changes differs from cell to cell because of the different porosity and diffusivity values. And regions that have larger

changes in density correspond to the streaks with high porosity values defining the bedding plane existed in the core. However, the increasing of the average CT number of the core during the actual experiment was not observed in the simulation. As mentioned in the fluid property section, the density of the dead oil decreases when the oil is mixed with CO_2. According to Tovar *et al.* (2014), one possible explaination of the density increase of the core during the experiment was the density of supercritical CO_2 being higher than the dead oil. However, after measuring the dead oil sample density, the density of the oil at 150 ºF and 3000 psi is actually higher than that of CO_2. Therefore, this assuption was incorrect. Another explaination given by Tovar *et al.* (2014) was the adsoption of CO_2 onto the organic matters, which was not captured in the simulation. Therefore, it is possible for the core density to increase during the experiment but decrease in the simulation as shown in the results above.

As mentioned in many literature, CO_2 reduces the viscosity of the oil to enhance the oil mobility, which can also be observed from the simulation as shown in **Fig. 38** below.

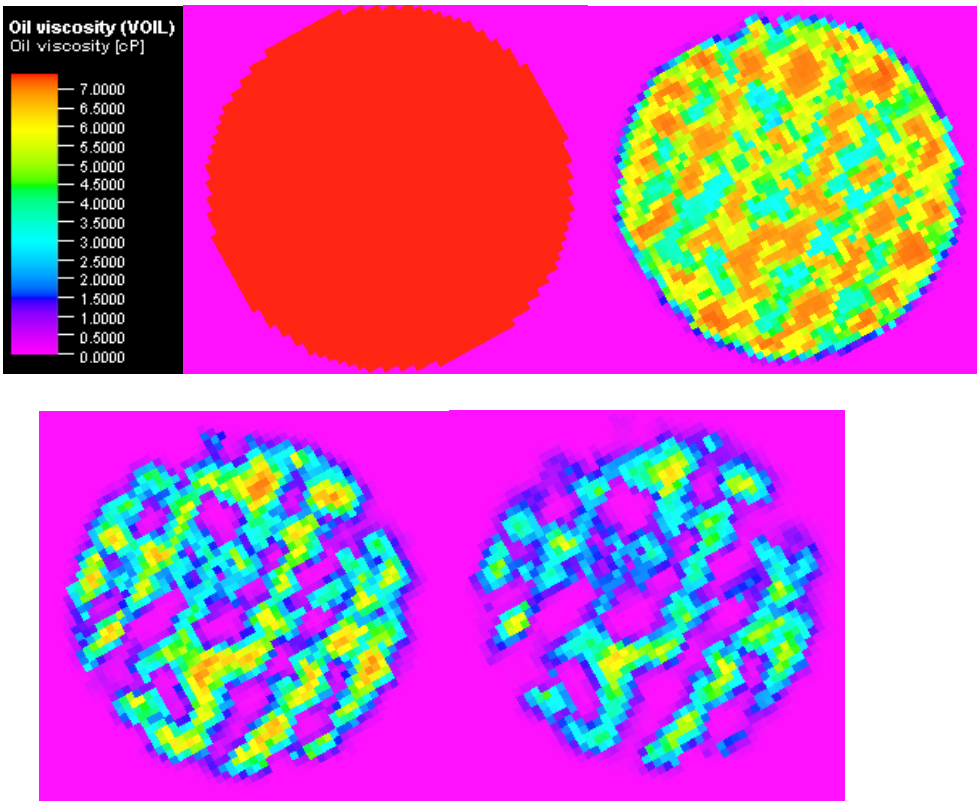

Fig. 38 – Oil viscosity reduction for the experiment I 3D heterogeneous model at time 0hr, 5hr, 24hr, 48hr.

A cumulative production of 0.4 ml was resulted from experiment I simulation as shown in **Fig. 39**. In addition, to confirm the fact that permeability values do not affect cumulative production, another case with the same porosity map as shown in Fig. 36 but a uniformed permeability value of 1E-4 mD for all grid blocks was run. Fig. 39 indicates that the two cases have the same cumulative production, which again proved that permeability plays a minor role in determining recovery when diffusion is the dominant mechanism.

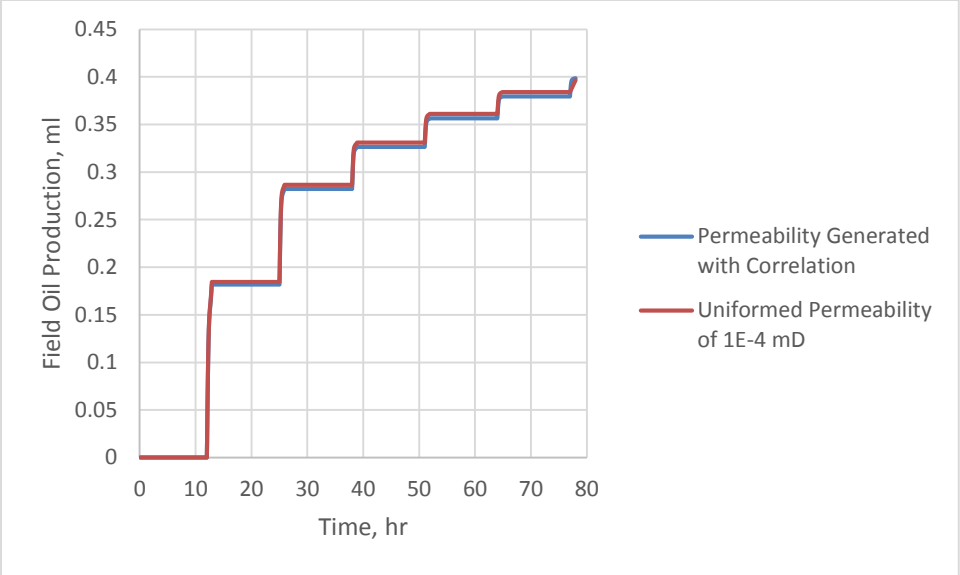

Fig. 39 – Cumulative production for the experiment I 3D heterogeneous model.

4.4.5 Experiment II – Heterogeneous 3D Model

The majority of the studies focusing on either core scale or field scale modeling of gas injection in unconventional reservoirs is based on homogenous models. The reason is because it is difficult to characterize the reservoir with conventional methods due to the complex compositions of organic and inorganic networks and properties that are difficult or impossible to measure in the laboratory. Studies such as Yan *et al.* (2013) are expanding into areas of using micro-scale multiple-porosity systems that include fracture, organic and inorganic matrices to model the nano-scale pores. This section presents a method utilizing MicroCT scan images to build a fine-scale heterogeneous 3D core model, which will aid in the understanding of the physical phenomena that took place during the actual experiment.

Experiment II was performed under immiscible conditions at 1600 psi and 150 ºF according to the estimated MMP of the fluid system. Since the cores from experiment II were readily available after the experiment for petrophysical property investigations, a heterogeneous 3D model was built for this experiment modeling. However, since the experiment was performed on preserved cores, dry core images of the same position as the available scans were unavailable. Therefore, a different approach was taken using MicroCT images of the dry cores after the experiment. However, this makes the validation of the experimental results with simulation impossible.

4.4.5.1 Porosity Map Determination

The two cores, namely 2-1 and 2-2, from the second experiment were cleaned with a Dean Stark apparatus for two weeks until toluene no longer had change in color by visual inspection. No water was extracted from the process. The cores were then placed inside an oven at 150 ºF for two days to evaporate the residual fluids. After cleaning the cores, helium porosity of cores were measured with a helium porosimeter. **Table 19** below shows the effective porosity values of core 2-1 and core 2-2 measured with the helium porosimeter.

	Test 1		Test 2	
Core	2-1	2-2	2-1	2-2
Effective Porosity	17.00%	18.10%	17.00%	17.60%

Table 19 – Effective porosity values of core 2-1 and 2-2 measured with helium porosimeter.

The helium porosity gives an approximation of the effective porosity of the core, which turned out to be surprisingly higher than the most accepted values for unconventional cores. To validate the results, a thin section analysis was done on both cores. The samples used for thin section analysis were 27 by 46 mm in dimension, and 0.03 mm in thickness. **Fig. 40** below are sample slices of thin section for the two cores. The blue colored regions are pores saturated with epoxy.

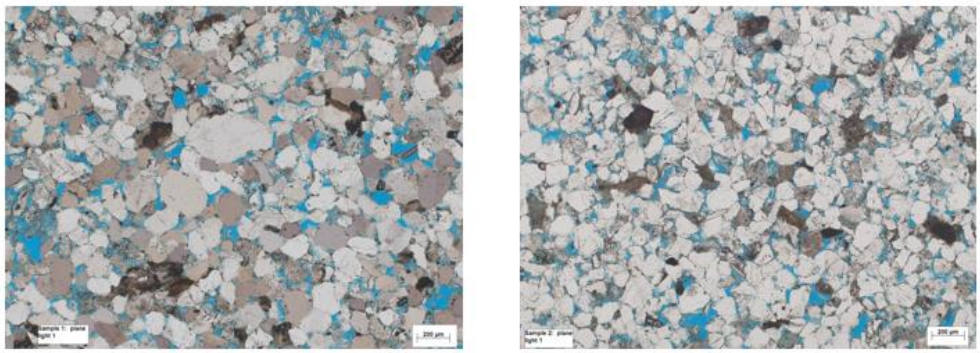

Fig. 40 – Thin section images for core 2-1 (left) and core 2-2 (right).

Image processing using software ImageJ point count revealed that core 2-1 and 2-2 have approximately 13% and 15% porosity, respectively, as shown in **Fig. 41**.

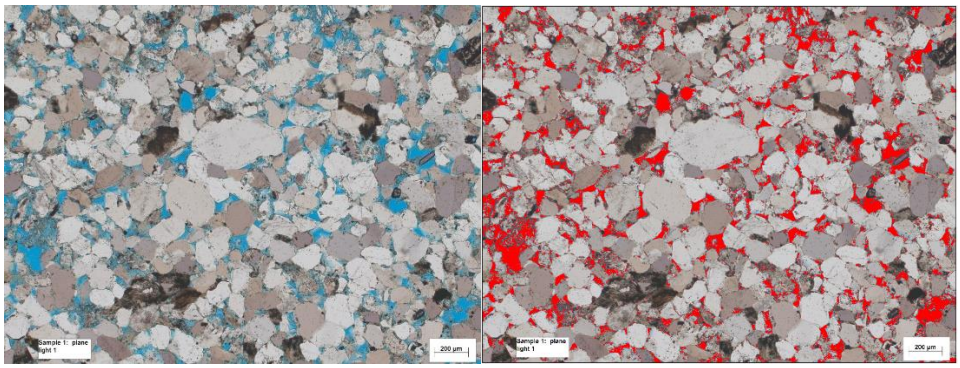

Fig. 41 – Image analysis for core 2-1 porosity estimation.

From the above measurements, the cores used in the second experiment after the Dean Stark process turned out to have considerably high porosity compared with unconventional core porosity stated in other literature. However, attempts of direct injection on these cores were unsuccessful. There are two possible explanations for the high porosity values. One is although the porosity of the core is high, the pores are not connected very well, which resulted in high hydrocarbon storage but little flow capability. The second possibility is that some of the materials contributing to the organic network presented in the pores were somehow removed during the Dean Stark process, although kerogen and bitumen are known to have low solubility in toluene. The matrix after the process was mainly composed of inorganic materials such as quartz, clays and calcites.

As seen in the CT images of the density change within the cores during experiment II in Tovar *et al.* (2014), the changes in density does not occur homogenously across the core. From the sensitivity analysis conducted earlier on a

homogenous slab model, porosity, diffusion coefficient, and saturation are the three main contributing factors for a heterogeneous change within the core. Since it is impossible to reasonably define the original water oil saturation inside the preserved core because of the low resolution of the CT images as well as the lack of knowledge of the water and oil capillary pressure, the study below is based on the assumption that the degree of change in CT number directly correlates to the porosity of each voxel.

In order to capture the heterogeneity of the core, a porosity map was determined from MicroCT images of the dry core. Conventionally, core porosity is determined from CT scan images with Hounsfield units of a dry core and the same core saturated with a certain fluid and scanned at the same position as the dry core. However, since it is inconvenient to saturate a shale core with a contrasting agent, and because of the low resolution of CT scan (0.3 – 0.5 mm per voxel), Microfocus Computed Tomography System was used in this part of the study. Although the MicroCT scanner does not have the fine resolution to define the nano pores existing in the shale, it is not necessary to define those pores for the purpose of this simulation.

Core 2-1 and 2-2 were scanned using GE Phoenix Nanotom S at 150 kV and 20 µA. The scans yielded 1677 16 bit gray scale images in the XY plane, and 1722 images in both YZ and XZ plane. The voxel size of the images is 14.99 µm. **Fig. 42** and **Fig. 43** below shows sample images of core 2-1 taken in XY and XZ planes.

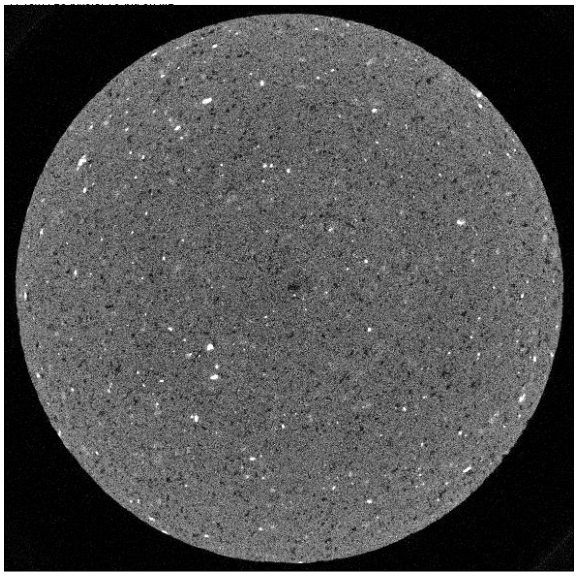

Fig. 42 – Sample MicroCT image of core 2-1 taken in the XY plane.

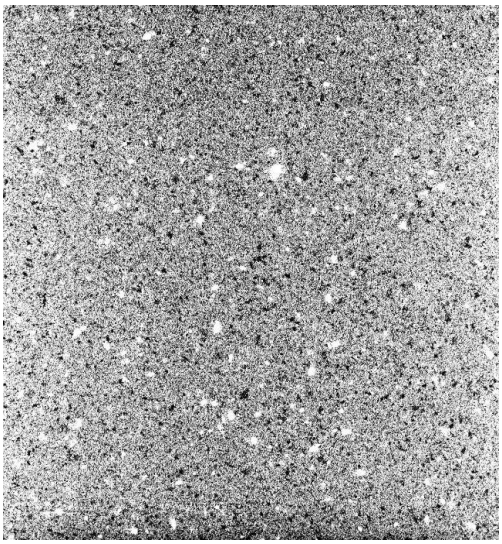

Fig. 43 – Sample MicroCT image of core 2-1 taken in the XZ plane.

From Fig. 42 and Fig. 43, one can see that the pores can be visually inspected from the images, and the voxels are small enough that it requires several of them to construct one pore as shown in **Fig. 44**.

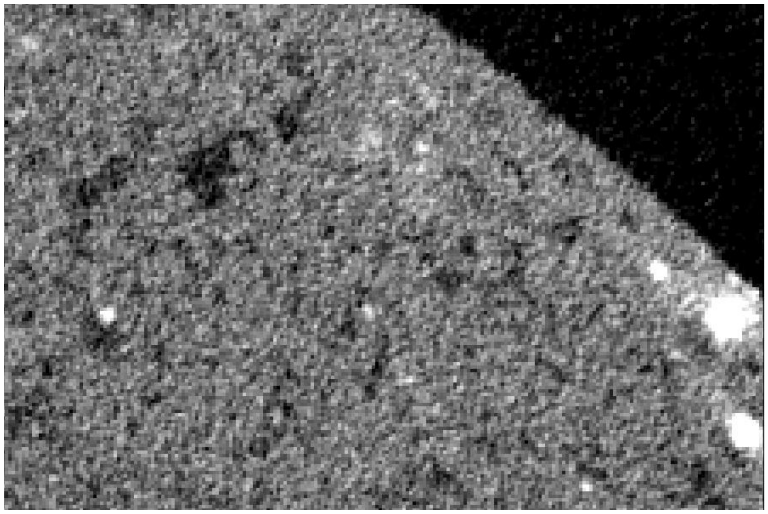

Fig. 44 – An enlarged view of a section of the XY plane view.

The MicroCT scan image was scaled down to a 50 voxel by 50 voxel image, which will fit in the grid built in Eclipse shown in Section 4.4.2.1. During the scaling of the images, the resolution of each voxel dramatically reduced from 14.99 μm 0.508 mm. The 50 by 50 image was then converted into a text file and imported into Excel. The method of segmentation was applied for porosity determination, which was mentioned in Landis and Keane (2010) and Taud *et al.* (2005). The threshold value for pores was determined to be 10000, which is the average voxel value for the air surrounding the

core. In other words, any voxel with values equals to or below 10000 will be defined as pores. And an average value of matrix is defined as 11676. Based on the two cutoff values, the porosity for each scaled down voxel was determined using a linear relationship. This method is repeated on a total of 10 slides of images, 5 from core 2-1 and 5 from core 2-2 to get a fair representation of the cores. Image selection is based on the position of the slice as well as avoiding the presence of artifacts which could greatly affect the results. On a side note, one should be aware of the level of uncertainty related with this method. There are two main sources which can cause an increase in the uncertainty. The first one is the scaling of the voxel, and the other one is the subjectively defined threshold values for pores and matrix.

In addition, to match the 0.4 ml production, the diffusion coefficients need to be scaled down dramatically since the porosity of the core averages 17%. In order to mimic the original core condition, the overall porosity value was scaled down instead of the diffusion coefficients. The original preserved core porosity average was assumed to be 6% based on the average values provided in literature (Sagar *et al.* 2010). A sample porosity distribution within a slice is shown in **Fig. 45**.

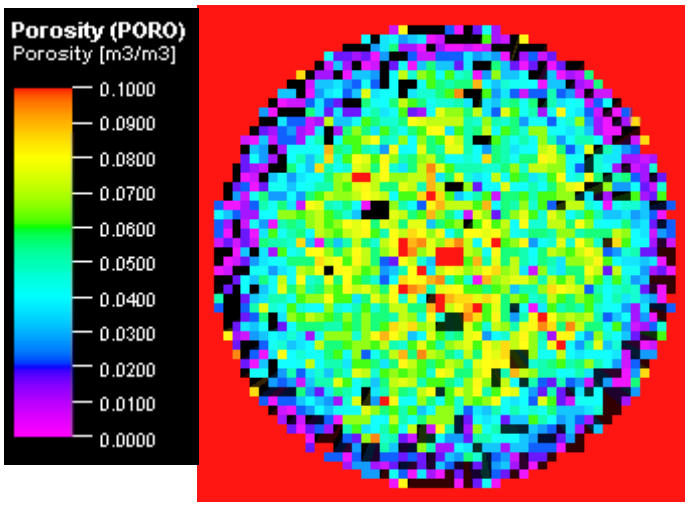

Fig. 45 – Porosity distribution for slice 3.

The black grid blocks are null cells that have the porosity value of zero. Although it is hard to observe in the MicroCT images, Fig. 45 shows a trend that the outer layer of the core has considerably lower porosity than the inside of the core. This trend was observed on every porosity slice generated from the MicroCT images. This is possibly due to the damage on the core during coring or the re-sizing process before the helium porosimeter measurement. This is a potential source of error in the porosity determination. Other properties were determined using the same method mentioned in Section 4.4.4.1.

The model was run at the immiscible condition as experiment II, which is 1600 psi at 150 ºF.

4.4.5.2 Results and Discussions

Again, by mimicking the soaking and producing schedule during experiment II, a cumulative production curve was obtained from the model run. Slight scaling down of diffusion coefficient was made in order to obtain a 0.4 ml cumulative production shown in **Fig. 46** below. The rate of production for each stage displays a decreasing trend.

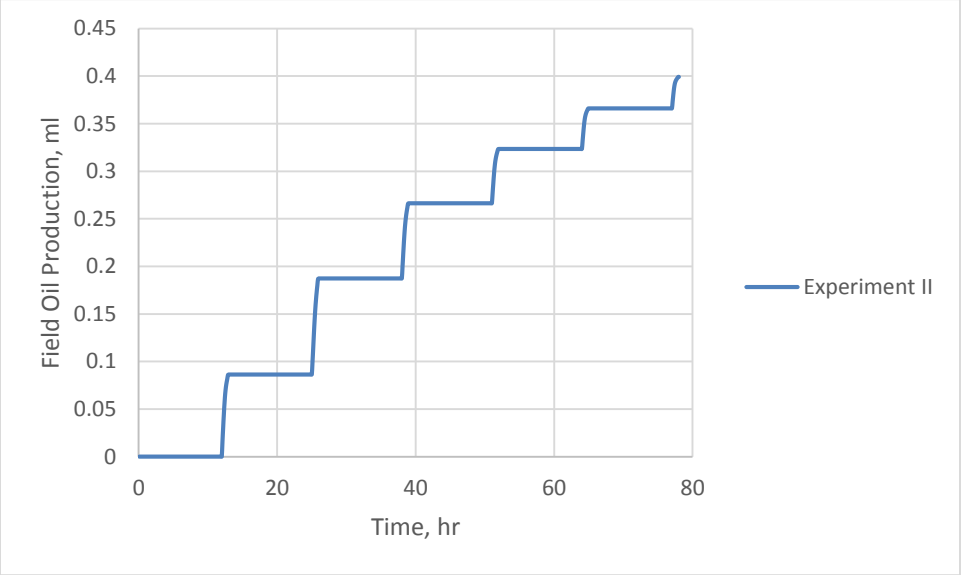

Fig. 46 – Cumulative oil production of experiment II 3D heterogeneous model.

Since the assumption made for the model was that the change in CT number (ΔCT) corresponds to density change in the oil phase. The oil density change for a particular grid block depends on the mole fraction of CO_2 at the time being considered. The oil density change can be observed in **Fig. 47**.

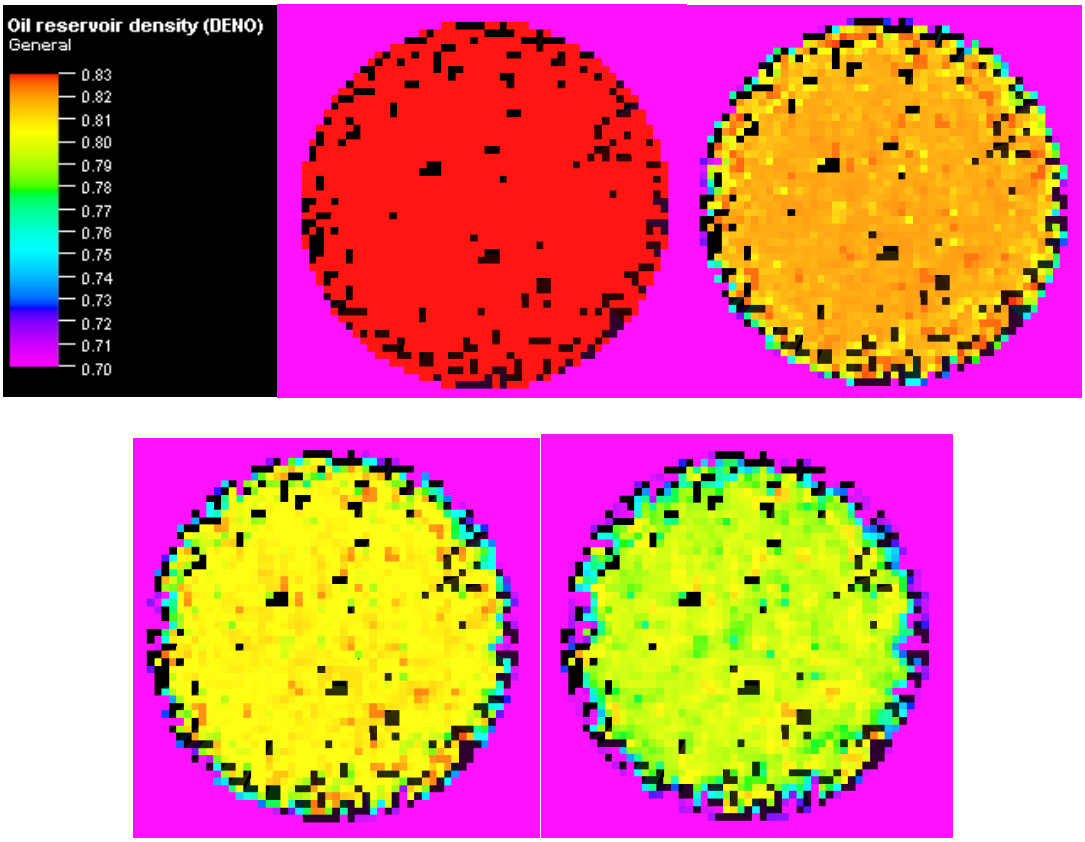

Fig. 47 – Oil density change over time for slice 3 at time 0 hr, 2 hr, 5 hr, 10 hr, 24 hr, 48 hr, 72 hr, and 78 hr.

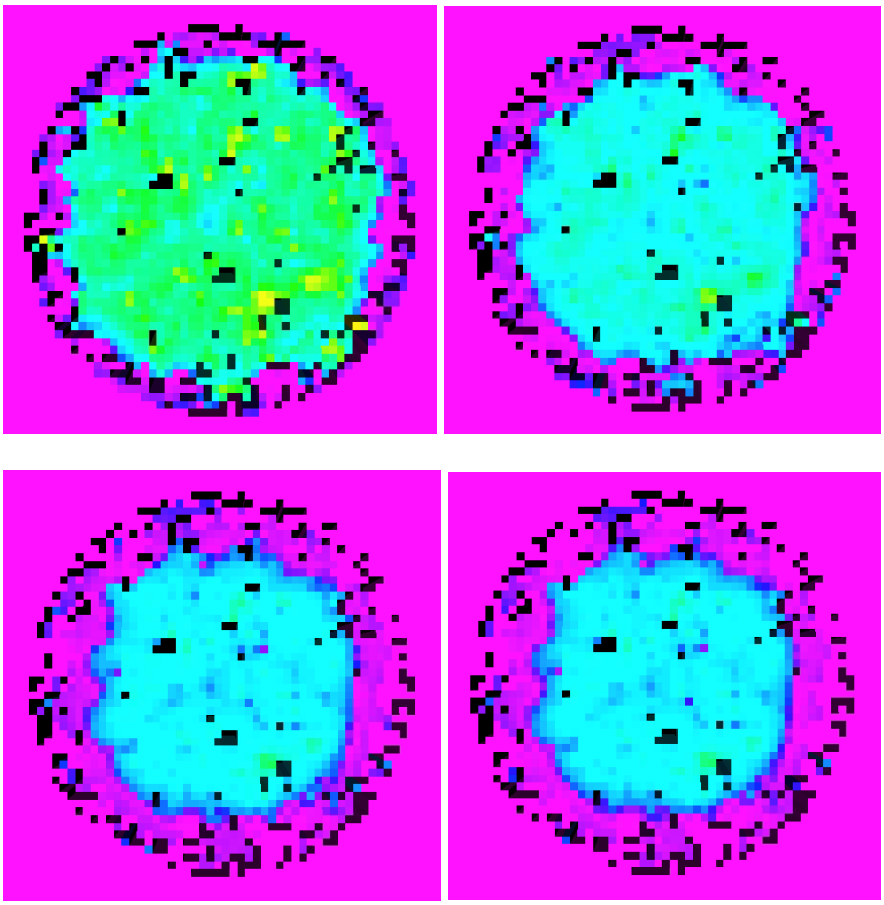

Fig. 47 Continued.

One should not expect to see the exact pattern in the change in density as the ones seen in the CT images from the experiment. However, similar trending can be observed. That is at different grid blocks with different properties, the change in density varies. However, similar to the CT images obtained from experiment II, one can observe the change in density is rather homogenous in comparison with the experiment I simulated results.

Properties that affect the degree of change in density are porosity, pressure, and diffusion coefficient. Water saturation also plays a role, however it is not accounted for in this case.

4.5 Field Case Modeling

A synthetic field case was developed to study the oil recovery mechanisms on a larger scale. To save computational time, a single stage with one fracture on a horizontal well was modeled. The main focus of this field study is to use the properties from the core model to predict and optimize the performance of CO_2 injection in various cases.

The SRV can be viewed in the schematic shown below in **Fig. 48**.

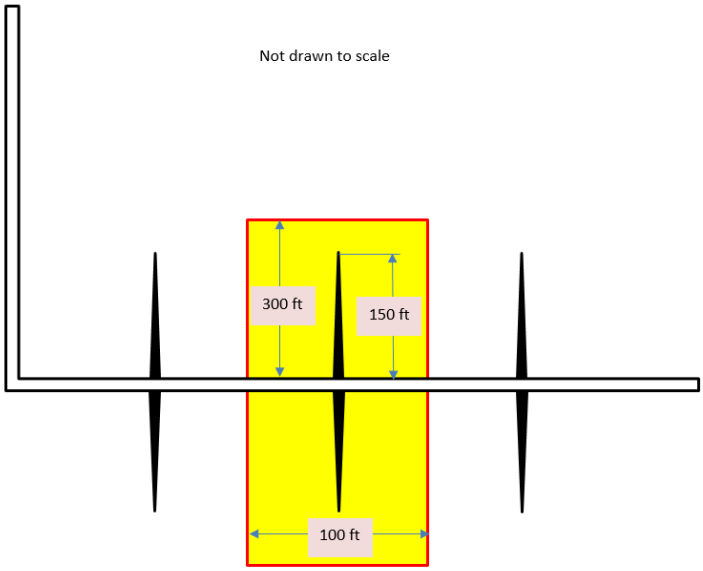

Fig. 48 – Schematic of the simulated reservoir volume (SRV).

Rivera (2014) fully explored the effect of production pressure, CO_2 injection time, injection length, number of cycles, soaking length, and permeability of matrix and natural fractures on the performance of a field scale cyclic gas injection in the Bakken formation in his study. In this study, the parameters used were obtained from core scale simulation, which is an improvement of the previously existed studies.

4.5.1 Fluid Model and Reservoir Properties

The fluid model for the experimental simulation was built based on the dead oil data from the reservoir. To model the fluid in the reservoir with little knowledge of the live oil properties, methane is combined with the dead oil components to create a live oil model to be used in the field model. In this section, since the model is built with field units, all units for tables and figures are switched from the previously used lab units to field units. **Table 20** below contains the fluid properties of the recombined live oil model. **Fig. 49** shows the phase diagram of the fluid. The bubble point pressure at 150 ºF occurs at 1200 psi.

Component	Mole Fraction, %	Critical Pressure, psi	Critical Temperature, R	Acentric Factor	Molecular Weight, g/mol
CO_2	1.00E-06	1055.88	547.56	0.23	44.01
C1	0.34	667.20	343.08	0.01	16.04
COMP1	0.22	497.47	1007.532	0.25	95.33
COMP2	0.20	347.60	1068.05	0.40	124.12
COMP3	0.15	248.97	1212.01	0.62	181.06
COMP4	0.09	136.43	700.45	1.00	259.99

Table 20 – Live oil composition and properties.

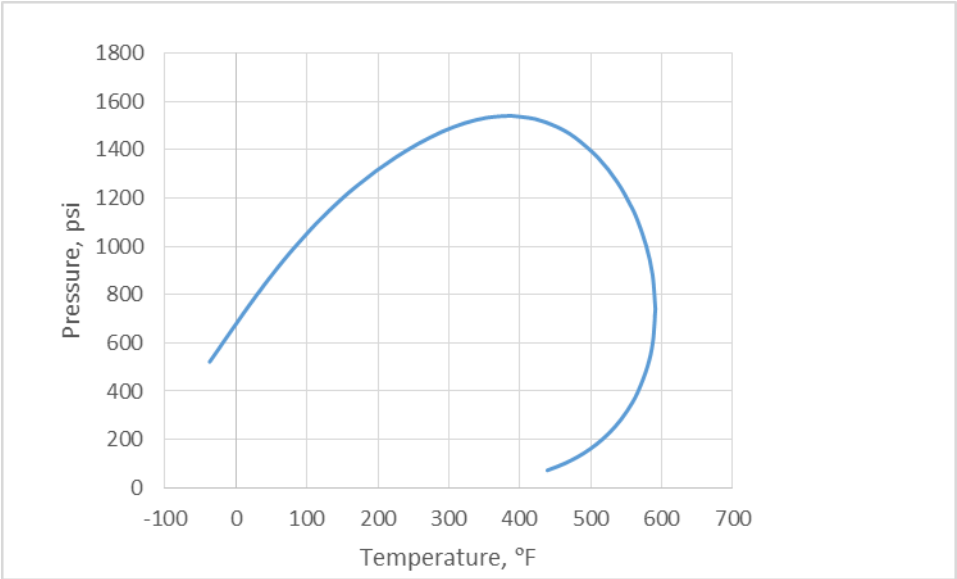

Fig. 49 – Phase diagram of the live oil.

The live oil has lower MMP than the dead oil due to the change in composition. Using the MMP module in PVTsim, the MMP is estimated to be 1417 psi, and FMC is 1789 psi at 150 °F.

Fig. 50 and **Fig. 51** below shows the density and viscosity change of the live oil at various pressures. As pressure increased, the density and viscosity both increased.

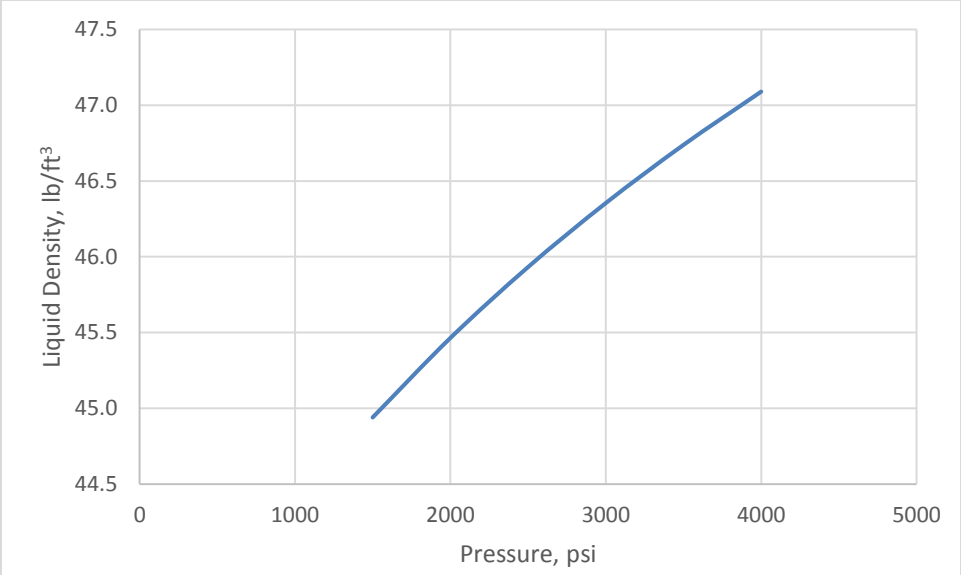

Fig. 50 – Oil density change at various pressure.

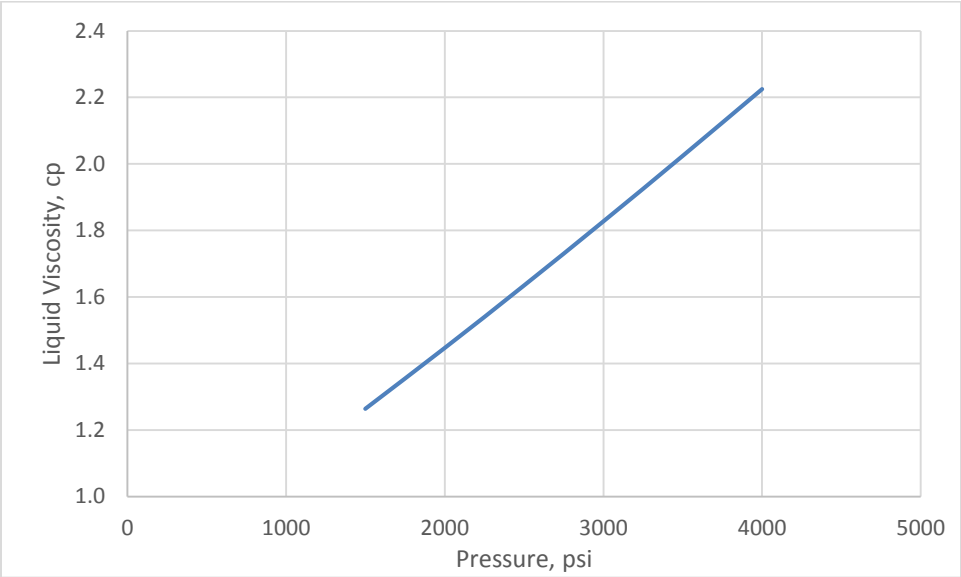

Fig. 51 – Oil viscosity change at various pressure.

During CO_2 injection, as the CO_2 mole fraction increases in the liquid phase the density and viscosity of the oil decrease as shown in **Fig. 52** and **Fig. 53**. In addition, oil swelling occurs as more CO_2 is mixed, and the saturation pressure increases as seen in **Fig. 54** and **Fig. 55**.

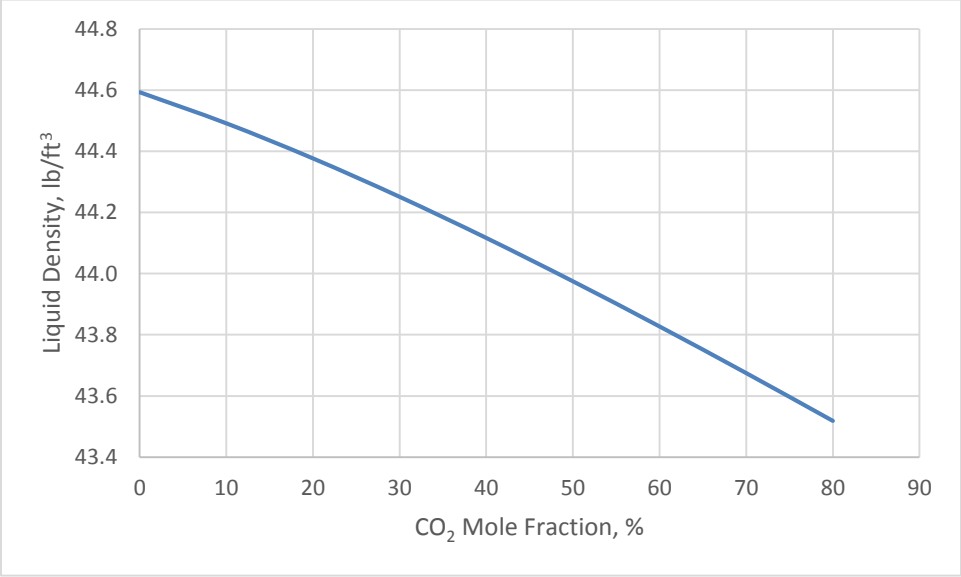

Fig. 52 – Oil density change at various CO_2 mole fraction in oil.

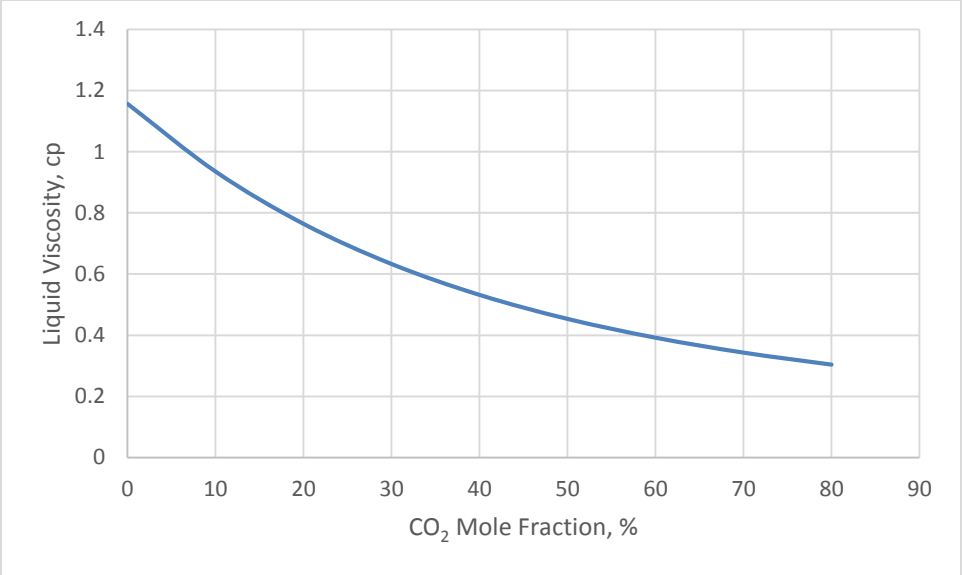

Fig. 53 – Oil viscosity change at various CO_2 mole fraction in oil.

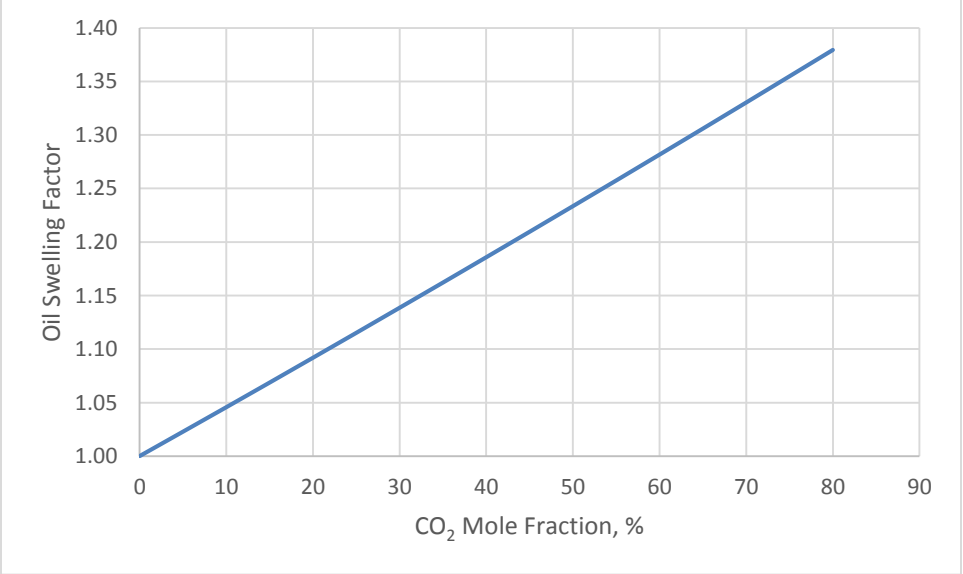

Fig. 54 – Oil volume change at various CO_2 mole fraction in oil.

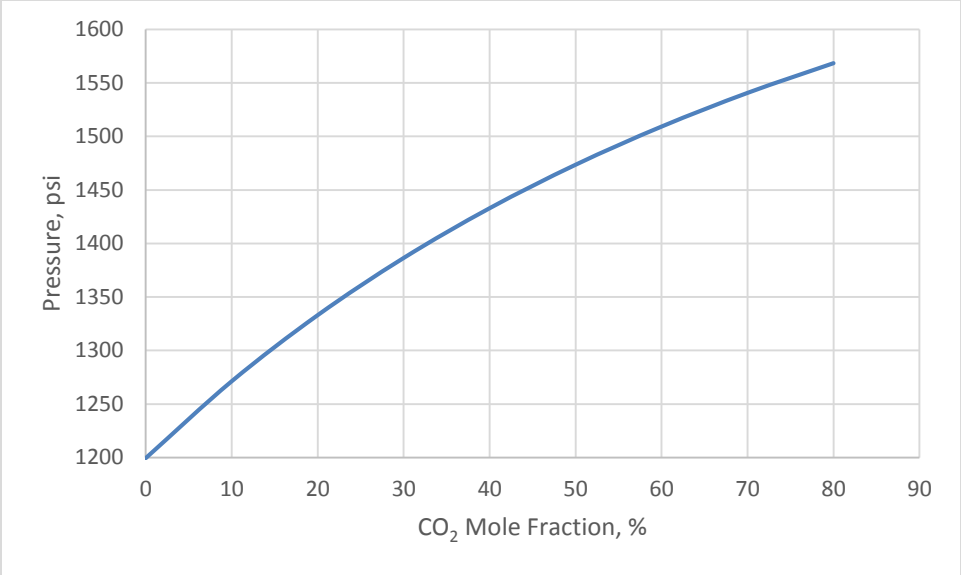

Fig. 55 – Saturation pressure change at various CO_2 mole fraction in oil.

The properties of the simulated reservoir are listed in **Table 21** below.

Grid Dimension	63 x 13 x 10
Fracture Half-length, ft	150
Pseudo-Fracture Width, ft	1
Pseudo-Fracture Permeability, mD	30
Fracture Porosity, %	45
Matrix Permeability, mD	1.00E-04
Matrix Porosity, %	6
Initial Water Saturation, %	10
Initial Reservoir Pressure, psi	3000
Reservoir Temperature, F	150
Pay Thickness, ft	100
HCPV, MSTB	40.72

Table 21 – Simulated reservoir properties.

The diffusion coefficients used were from experiment I simulation. **Table 22** below shows the diffusion coefficients after converting to field units.

Component	CO_2	COMP1	COMP2	COMP3	COMP4
Gas, ft^2/day	2.69E-05	1.33E-06	1.20E-06	8.43E-07	6.32E-07
Oil, ft^2/day	9.18E-06	1.09E-06	1.01E-06	8.12E-07	6.35E-07

Table 22 – Diffusion coefficient used in the field model.

4.5.2 Primary Depletion and Base Case

4.5.2.1 Primary Depletion

The bubble point pressure for the recombined live oil is at 1200 psi, which is below the MMP value. In this study, since the reservoir is slightly over pressured, the initial pressure of the reservoir is 3000 psi. Cases with different production pressures were considered for the primary depletion case, which will all be investigated for huff-n-puff performance later. In this study, the bottom-hole pressure of the producer is a fixed value. Generally, to model the early time behavior of production, the bottom-hole pressure is adjusted to decrease with time to match the early increase in production due to wellbore cleaning. However, this can be ignored because the main objective of the study is not to match production, but to investigate the feasibility of CO_2 huff-n-puff with parameters obtained from matching laboratory experiments. The production pressure for the different cases are 2000 psi, which is above the FMC pressure; 1550 psi, which is slightly above the MMP; 1300 psi, which is below the MMP but above the bubble point pressure; and 1000 psi, which is below the bubble point pressure. **Table 23** below shows the producer BHP and the recovery factors for the different cases. **Fig. 56** shows the pressure depletion only cumulative oil production for all cases for 5000 days.

	Producer BHP, psi	Recovery Factor, %
Case 1	1000	4.11
Case 2	1300	2.24
Case 3	1550	1.86
Case 4	2000	1.24

Table 23 – Cases with different producer BHP and the corresponding recovery factors.

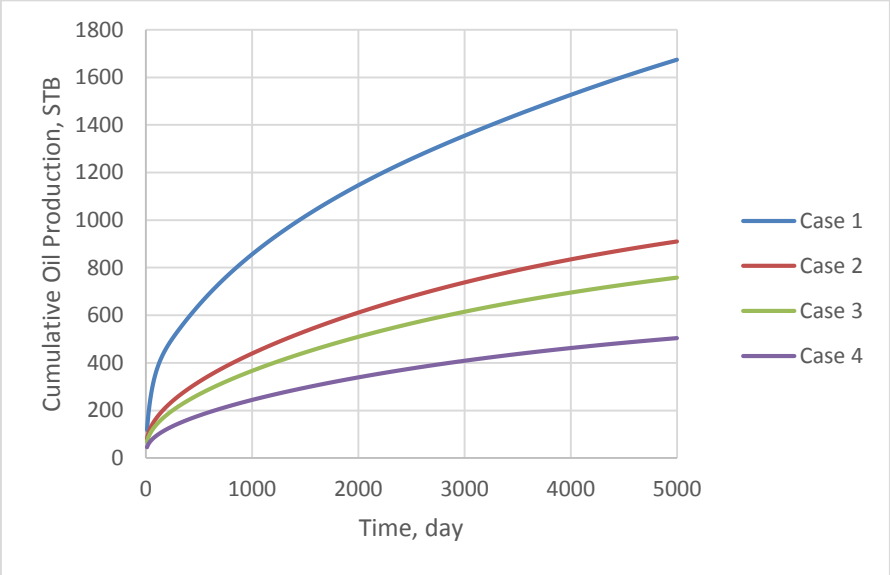

Fig. 56 – Cumulative oil production for the primary depletion cases with different producer BHP.

The recovery factors for the cases above are very low. In reality, natural fractures exist in these reservoirs so that production should be higher than the calculated value in this model depending on the intensity of the natural fractures.

From Fig. 56, one can see that when producing at lower pressure, the cumulative production is significantly higher. Especially when the pressure in the near wellbore and

fracture regions dipped below bubble point pressure, the flow becomes two phase, and the gas coming out from solution provided extra energy for the flow.

4.5.2.2 Huff n Puff 1 Cycle

In this section, 1 cycle of CO_2 was injected following the primary depletion cases shown in the last section. The injection time was on day 1000 for all cases. The injectors were constrained by surface rate at 500 Mscf/day with BHP constraint at 3500 psi, which was assumed to be below the reservoir fracture pressure at the corresponding depth. Four cases were run, each with different primary depletion BHP shown in the last section. After 30 days of injection and 15 days of soaking, the production took place at the same pressure as the corresponding primary depletion BHP. **Table 24** lists all injection cases as well as the corresponding depletion only cases. The recovery factors for all cases, as well as the recovery factor increment for each injection case were calculated. **Fig. 57** shows the cumulative oil production for all cases.

	Producer BHP, psi	Recovery Factor, %	Recovery Factor Increment, %
Case 1 Depletion	1000	4.11	N/A
Case 2 Depletion	1300	2.24	N/A
Case 3 Depletion	1550	1.86	N/A
Case 4 Depletion	2000	1.24	N/A
Case 1 - 1 Cycle	1000	4.52	0.41
Case 2 - 1 Cycle	1300	2.31	0.08
Case 3 - 1 Cycle	1550	1.89	0.03
Case 4 - 1 Cycle	2000	1.26	0.02

Table 24 – Recovery factor for the different cases and recovery factor increment for the injection cases.

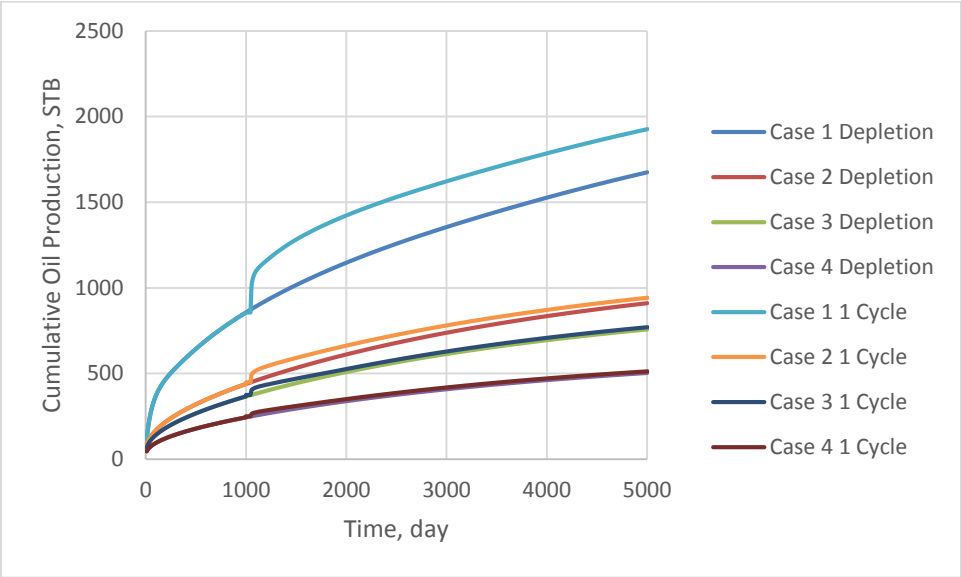

Fig. 57 – Cumulative oil production for all cases.

As Table 24 shows, case 1 depletion and case 1 injection show the largest production, as well as the largest recovery increment among all cases. This is because two-phase flow occurs when producing at pressures below the bubble point. The pressurizing effect of injected gas is more pronounced. Again, when production occurs at pressure below the bubble point following the injection, gas comes out of the solution and provides extra energy for the flow. Unfortunately, the rest of the cases have very small increment in recovery even when CO_2 is mixed with the oil phase. This is because unlike the laboratory experiment, the fractures were saturated with oil instead of fully saturated with pure CO_2. This greatly reduced the chemical potential of CO_2 existing in the fractures and very little CO_2 was able to reach further into the nano-Darcy

permeability matrix with the small diffusion coefficient values obtained from laboratory experiment simulations. Therefore, the production after CO_2 injection showed very minimal improvement because the primary change of oil properties still existed in the fracture regions. The improvement of production was mainly due to the viscosity reduction of the oil existed in the fractures.

Case 1 and case 1 with 1 cycle of injection were chosen to be the base case for the preceding studies in the following section.

4.5.3 Sensitivity Analysis of Reservoir Properties

4.5.3.1 Matrix Porosity

In this section, the matrix porosity was altered for various cases. Increasing the matrix porosity to 12% gave higher HCPV values. **Table 25** below summarizes the cases and the corresponding recovery factors and recovery factor increments. **Fig. 58** shows the cumulative production for all cases.

	Matrix Porosity	Recovery Factor, %	Recovery Increment, %
Case 1 Depletion	0.06	4.11	N/A
Case 1 - 1 Cycle	0.06	4.52	0.41
Case 2 Depletion	0.12	5.50	N/A
Case 2 - 1 Cycle	0.12	5.89	0.38

Table 25 – Recovery factor and recovery factor increment for different matrix porosity cases.

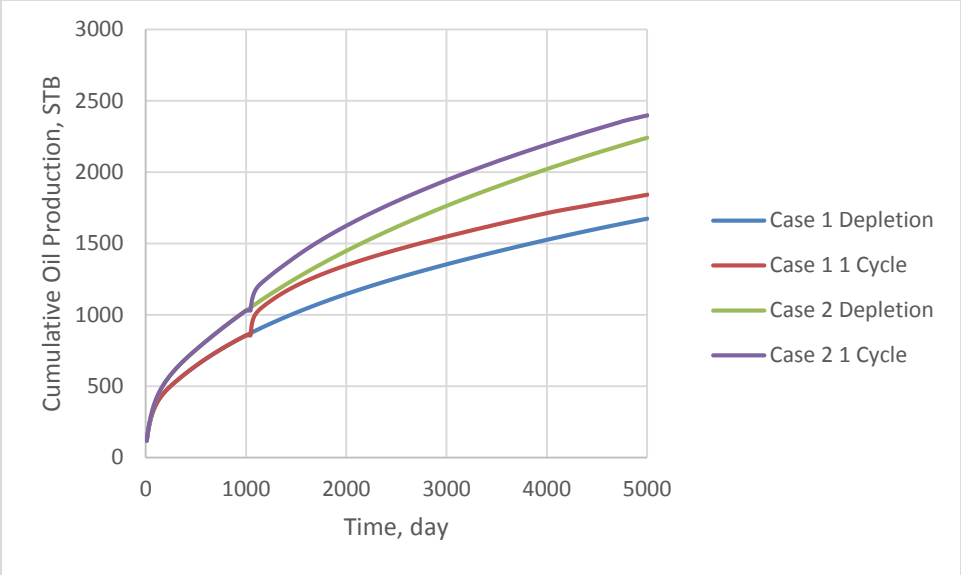

Fig. 58 – Cumulative production for matrix porosity sensitivity analysis.

As mentioned in the last section, the reason for the little increments in oil recovery for case 2 to 4 was the fact that CO_2 was not able to diffuse into the matrix in large quantities to change the oil properties. The sensitivity analysis on matrix porosity validated this hypothesis. From the core scale simulation, the conclusion of having higher matrix porosity results in higher oil recovery due to a larger contact area and higher diffusivity was drawn. However, the same behavior was not observed in the field case. Having higher matrix porosity resulted in lower recovery increments as seen in Table 25. If the CO_2 was able to reach deep into the matrix by diffusion, the result would be the opposite. However, having higher matrix porosity resulted in higher overall recovery factors. As seen in Fig. 58, even the primary depletion time observed higher recovery due to the higher HCPV. In conclusion, contrary to laboratory observation and

simulation results, higher matrix porosity does not grant advantages during CO_2 injection due to the significantly smaller fracture/matrix PV ratio and the fact that CO_2 was unable to reach deep into the matrix.

4.5.3.2 Matrix Permeability

As mentioned in the experiment simulation section, the matrix permeability did not have an effect on recovery because diffusion was the dominating oil recovery mechanism. In this section, the matrix permeability was increased by a factor of 10. Based on **Table 26** and **Fig. 59**, increasing the matrix permeability significantly increased the recovery factor by more than two folds. The large increase in production can be observed starting early time. The recovery factor increment also increased for the cases with higher matrix permeability values. Based on this observation, convection due to pressure drawdown can be said to be the dominating mechanism instead of diffusion in a field scale model. The effect of diffusion will be discussed later on.

	Matrix Permeability, mD	Recovery Factor, %	Recovery Increment, %
Case 1 Depletion	1.00E-04	4.11	N/A
Case 1 – 1 Cycle	1.00E-04	4.52	0.41
Case 2 Depletion	1.00E-03	8.85	N/A
Case 2 – 1 Cycle	1.00E-03	9.53	0.68

Table 26 – Matrix permeability sensitivity analysis.

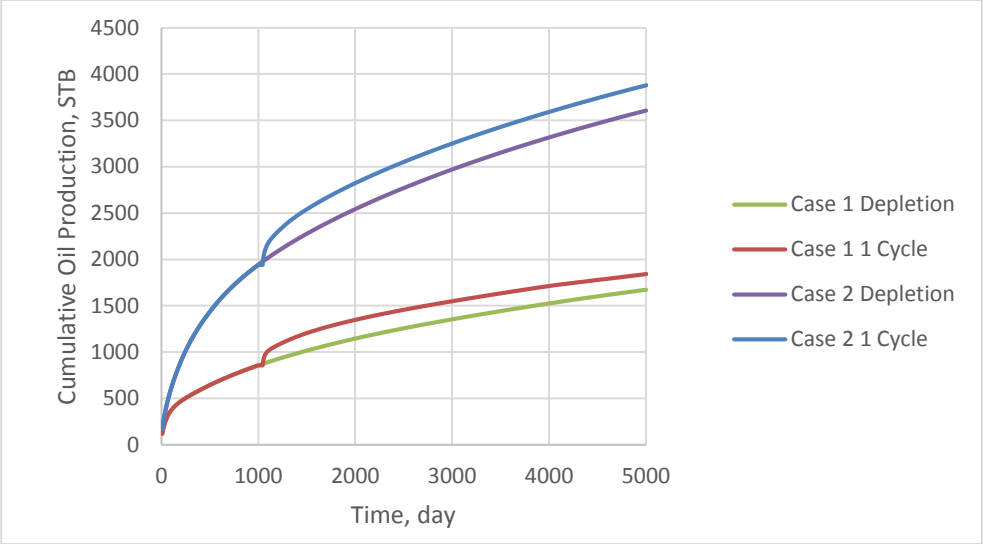

Fig. 59 – Cumulative oil production of matrix permeability sensitivity analysis.

4.5.3.3 Fracture Porosity

In this section, the fracture porosity is reduced to 20% from the base case 45%. Since earlier discussion contributed the oil production mainly from the fracture regions, reducing the fracture storage would cause a decrease in production, which can be seen in **Table 27** and **Fig. 60**.

	Fracture Porosity	Recovery Factor, %	Recovery Increment, %
Case 1 Depletion	0.2	3.63	N/A
Case 1 – 1 Cycle	0.2	3.91	0.28
Case 2 Depletion	0.45	4.11	N/A
Case 2 – 1 Cycle	0.45	4.52	0.41

Table 27 – Fracture porosity sensitivity analysis.

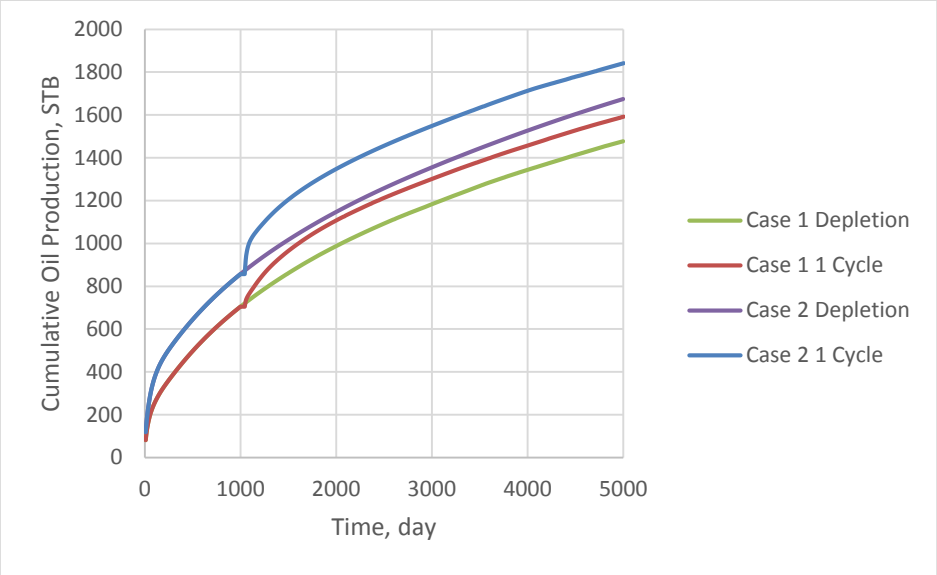

Fig. 60 – Cumulative oil production for fracture porosity sensitivity analysis.

4.5.3.4 Fracture Permeability

In the base case, the fracture conductivity was 30 mD-ft. In this section, the fracture conductivity was increased to 200 mD-ft as shown in **Table 28**. From Table 28 and **Fig. 61**, one can see that unlike other reservoir properties, increasing fracture conductivity have a pronounced effect on oil recovery because fractures are the main contributing factors to flow to the well.

	Fracture Permeability, mD	Recovery Factor, %	Recovery Increment, %
Case 1 Depletion	30	4.11	N/A
Case 1 - 1 Cycle	30	4.52	0.41
Case 2 Depletion	200	4.17	N/A
Case 2 – 1 Cycle	200	4.82	0.65

Table 28 – Fracture permeability sensitivity analysis.

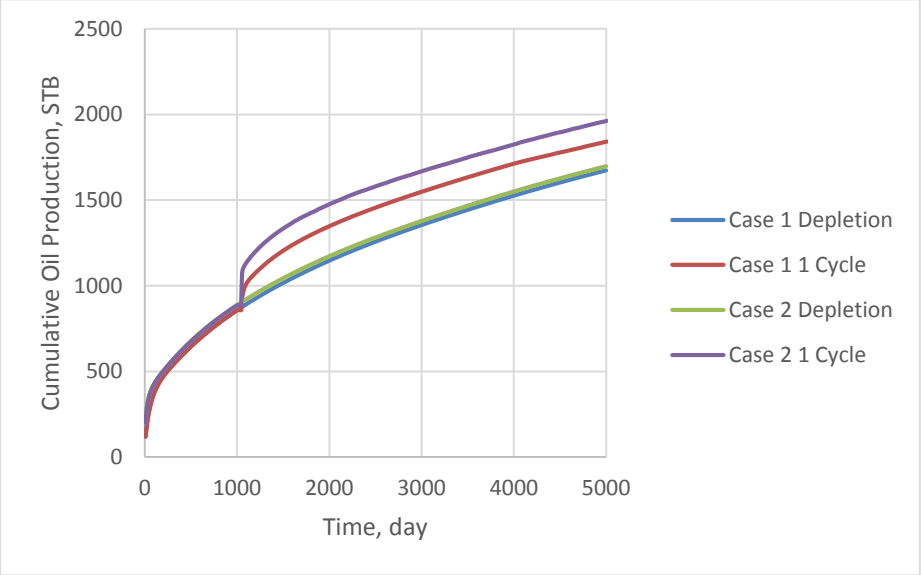

Fig. 61 – Cumulative oil production for fracture permeability sensitivity analysis.

4.5.3.5 Capillary Pressure

In this section, the oil/gas capillary pressure curves were altered from mid-range capillary pressures shown in Fig. 28 to zero capillary pressure. Note that the matrix and fracture regions have different input capillary pressures. In the matrix region, the mid-range capillary pressures were used, whereas in the fracture region, the capillary

pressure was assumed to be zero. The purpose is to exam whether interfacial tension reduction is a contributing production mechanism. Recall the conclusion drawn from laboratory experiment simulations that capillary pressure curves have no effect on the recovery factor. The same observation can be seen in **Table 29** and **Fig. 62**. The reason, again, is because the fractures are the main source of production, and the capillary pressure in the fracture region is zero in the simulation.

	Pcog range	Recovery Factor, %
Case 1	No Pcog	450
Case 2	Mid Pcog	4.52

Table 29—Sensitivity analysis of matrix capillary pressure.

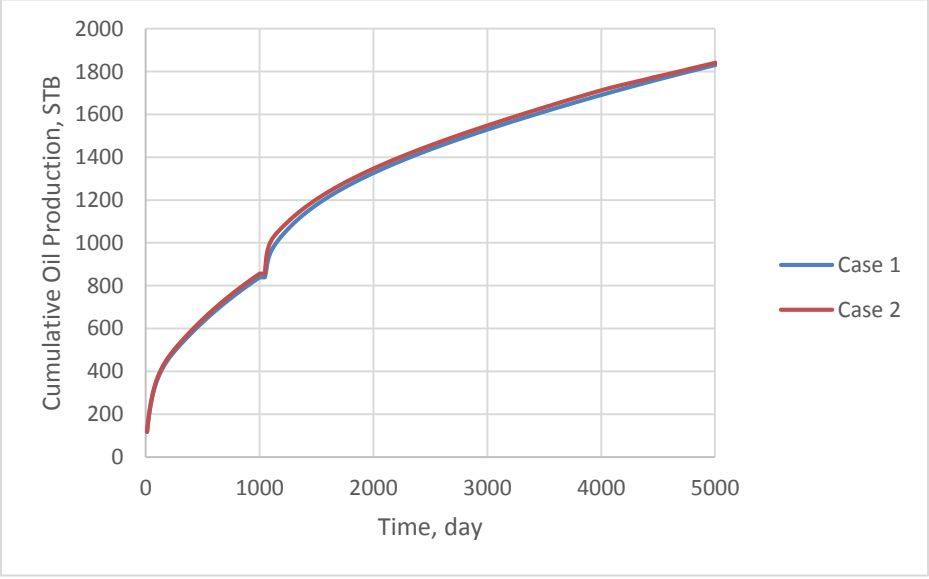

Fig. 62 – Cumulative oil production for matrix capillary pressure sensitivity analysis.

4.5.3.6 Effect of Diffusion

To answer the question of whether diffusion is the contributing mechanism during production from liquid shale reservoirs, the diffusion coefficient was deactivated in case 2. Two scenarios were investigated. In the first scenario, primary depletion and production after gas injection both occurred at BHP of 1000 psi. **Table 30** and **Fig. 63** present the result for scenario 1. One can see that deactivating diffusion makes no difference in the overall production. This observation validated the previously drawn conclusion that the penetration of CO_2 inside the matrix due to diffusion is limited. Especially in Scenario 1, where production occurs at pressure below the bubble point, the CO_2 that was mixed with the oil during injection and soaking period would come out from solution, which does not aid in the process of matrix oil production.

		Recovery Factor, %
Case 1	Diffusion	4.52
Case 2	No Diffusion	4.52

Table 30 – Diffusion coefficient sensitivity analysis for 1000 psi BHP cases (Scenario 1).

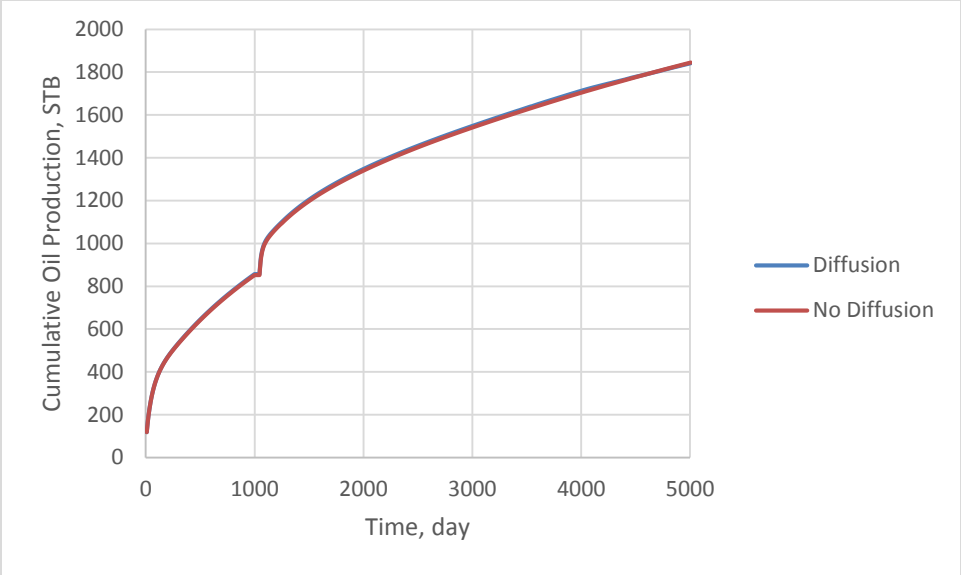

Fig. 63 – Cumulative oil production for diffusion coefficient sensitivity analysis (Scenario 1).

In the second scenario, primary depletion and production after injection occurred at 2000 psi, which is above the MMP as well as the bubble point pressure. Producing at 2000 psi ensured that CO_2 stays in solution during the production phase. In scenario 2, the effect of diffusion, although not very significant, can be observed as seen in **Table 31** and **Fig. 64**.

		Recovery Factor, %
Case 1	Diffusion	1.26
Case 2	No Diffusion	1.22

Table 31 – Diffusion coefficient sensitivity analysis for 1000 psi BHP cases (Scenario 2).

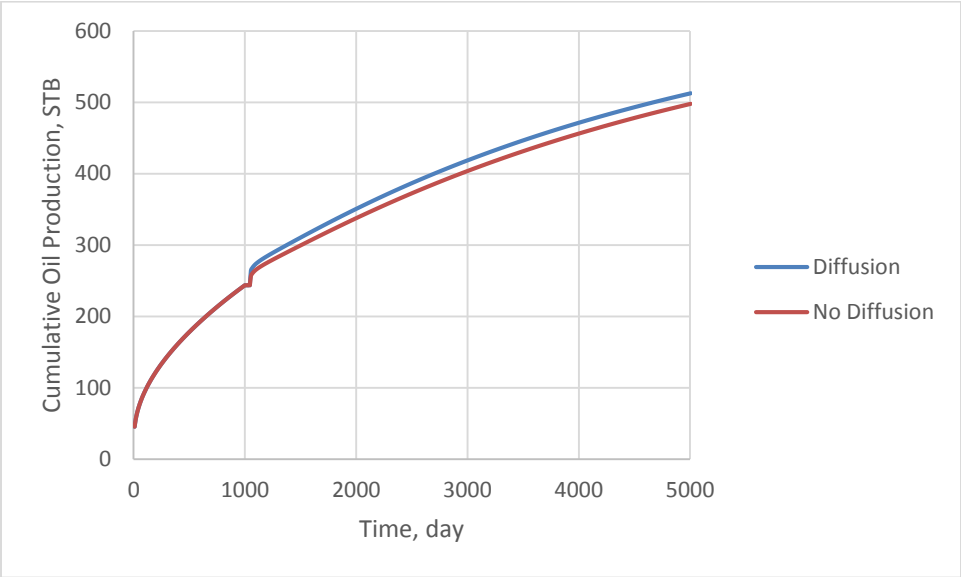

Fig. 64 – Cumulative oil production for diffusion coefficient sensitivity analysis (Scenario 2).

Some of the previously existing field scale simulation works indicate dramatic difference between the diffusion and no diffusion cases. For instance, in the work conducted by Wan and Sheng (2015), the effect of incorporating diffusion coefficient is large compared with the case with no diffusion coefficient. There are two possible reasons that the conclusions drawn from this section are in contrary with their conclusions. One is that they used a dual porosity/dual permeability model to simulate a direct injection case. The model incorporates natural fractures, which during a gas flooding are easier to be saturated with high concentration of CO_2 than a huff n puff case without natural fracture modeling. The second reason is that they used diffusion coefficients that are almost 1000 times higher than the diffusion coefficients used in this

work, which does not really have a sound basis, especially when their reservoir pressure is a lot higher than the one in this work at the same reservoir temperature. A typical diffusion coefficient value is in the range of 10^{-8} to 10^{-10}. The diffusion coefficients used in this study fall within this reasonable range.

4.5.4 Sensitivity Analysis of Operational Parameters

4.5.4.1 Time of First Injection

In this section, the time of the first injection cycle was studied. **Table 32** summarizes the first injection date. As shown in Table 32 and **Fig. 65**, starting the injection at a later time improved production. This is mainly because of the re-pressurizing effect is larger when the reservoir is allowed to deplete for longer. However, as discussed in the study done by Rivera (2014), economic value of the project needs to be investigated because the optimal CO_2 injection time varies for different cases.

	First Injection Day	Recovery Factor, %
Case 1	N/A	4.11
Case 2	500	4.43
Case 3	1000	4.52
Case 4	2000	4.63

Table 32 – Sensitivity analysis on the starting time of the first injection cycle.

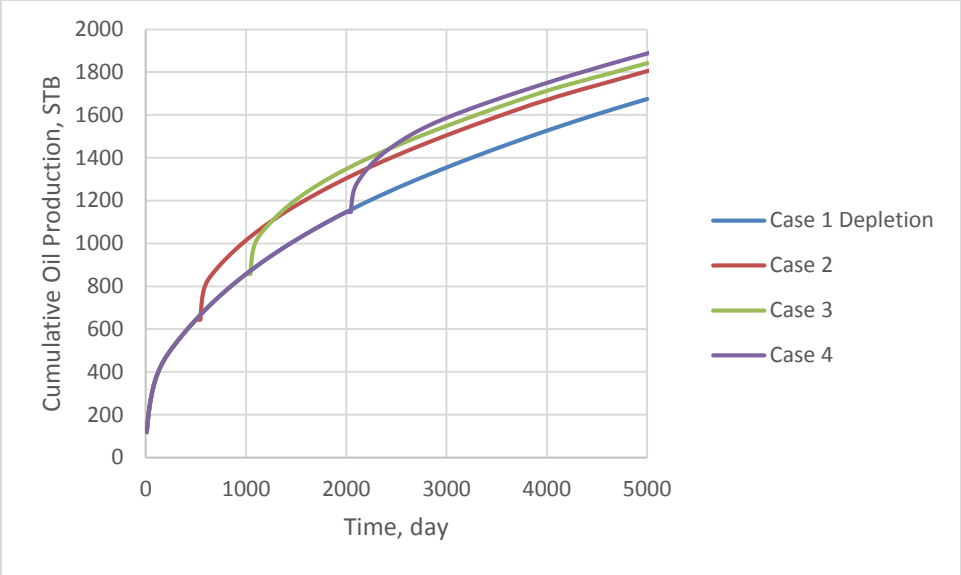

Fig. 65 – Cumulative oil production of sensitivity analysis on the starting time of the first injection cycle.

4.5.4.2 Injection Rate

In this section, different injection rates were investigated. The injector BHP constraints were kept the same for both at 3500 psi. The keyword WTEST (Eclipse 2014) was used to ensure the reopening of the injector when the physical condition allows it to flow again. As **Table 33** and **Fig. 66** show, increasing the injection rate has some effect on recovery factors. This is because larger injection rates resulted in larger CO_2 volume to be pumped inside the formation. If the injector for the higher injection rate were allowed a higher BHP constraint, a much higher increment in recovery factor would have been observed because of the even larger CO_2 volume. Increasing the amount of CO_2 volume pumped into the reservoir not only helps reduce the fracture oil

viscosity further, but also raises the chemical potential of CO_2 in the fracture and allow more CO_2 to go into the matrix.

	Injection Rate, MSCF	Recovery Factor, %
Case 1	N/A	4.11
Case 2	500	4.52
Case 3	5000	4.74

Table 33 – Sensitivity analysis on injection rate.

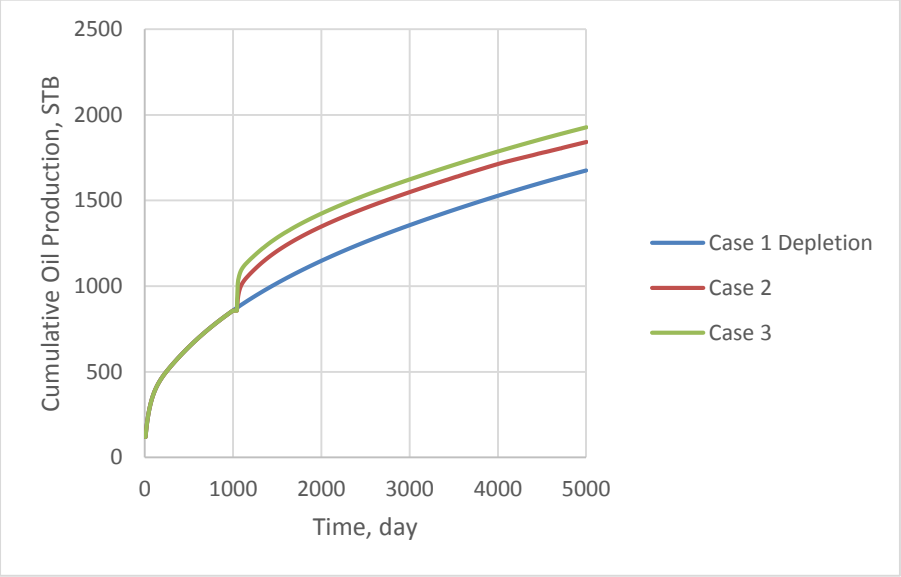

Fig. 66 – Cumulative oil production for sensitivity analysis on injection rate.

4.5.4.3 Injection Pressure

Three cases were investigated in this section. Case 1 is the base case in which the injector BHP constraint is at 3500 psi. Case 2 is an immiscible injection case with injector BHP constraint at 1400 psi. Case 3 is a continuation of the capillary pressure study, in which the capillary pressure of case 2 is set to be zero.

From **Table 34** and **Fig. 67**, one can see the increase in the recovery factor when pumping at higher pressure. Case 2 proves that even under immiscible condition, re-pressurizing the reservoir (or rather the fracture) and providing gas drive can help with production. Case 3 further validated that the recovery factor is not affected by oil/gas capillary pressure of the matrix.

	Injection Pressure, psi	Recovery Factor, %	Note
Case 1	3500	4.52	
Case 2	1400	4.27	
Case 3	1400	4.27	No Pcog

Table 34 – Sensitivity analysis of injection pressure.

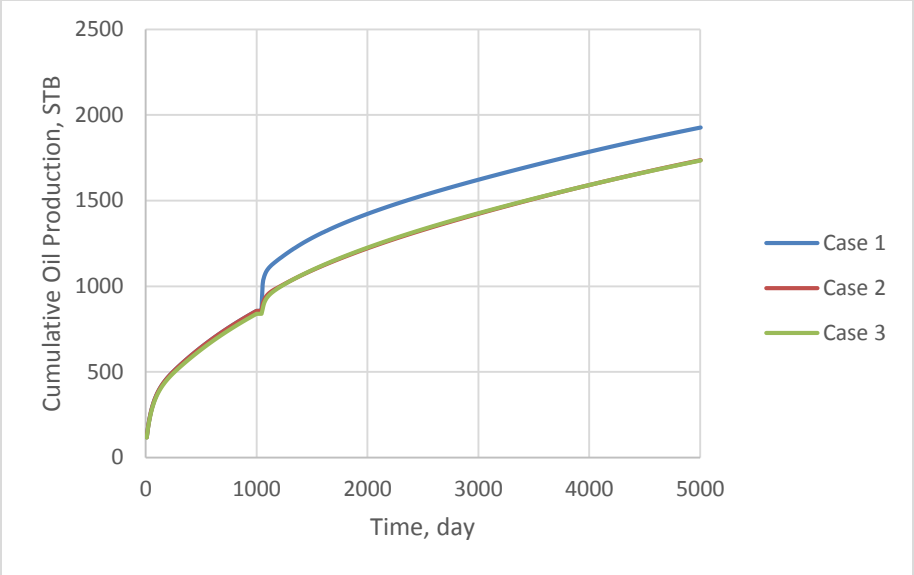

Fig. 67 – Cumulative oil production of injection pressure sensitivity analysis.

4.5.4.4 Length of Injection Time

In this section, the length of injection time was studied. The four cases with various injection duration are listed in **Table 35**. Having longer injection compromises production time to some degree. However, as one can see in Table 35 as well as **Fig. 68**, the longer injection times resulted in higher recovery factors. Again, the reason for higher recovery is similar to that of larger injection rate. Larger injected CO_2 volume results in higher production.

	Injection Duration, day	Recovery Factor, %
Case 1	N/A	4.11
Case 2	10	4.50
Case 3	30	4.52
Case 4	60	4.58
Case 5	200	4.66

Table 35 – Sensitivity analysis of the length of injection time.

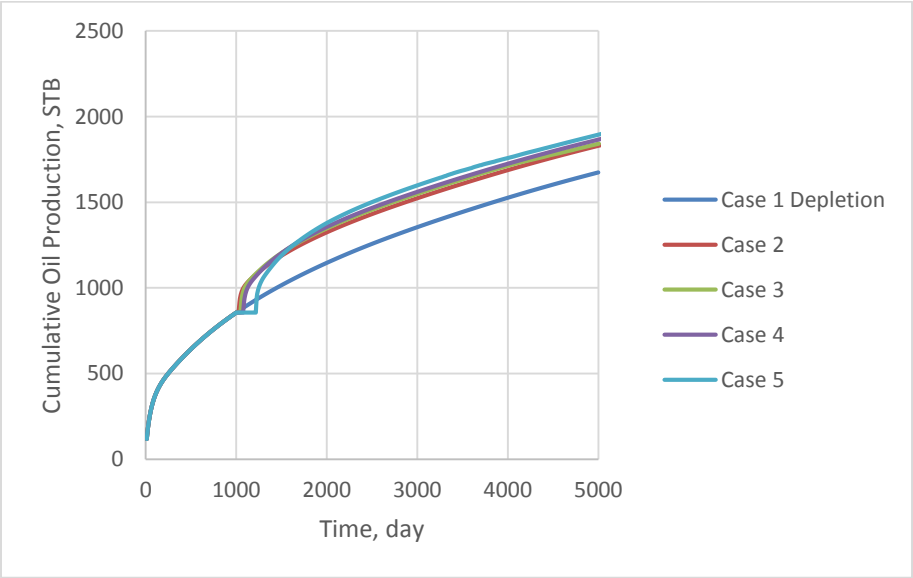

Fig. 68 – Cumulative oil production of injection duration sensitivity analysis.

4.5.4.5 Length of Soaking Time

In this section, three cases with different lengths of soaking time were investigated. Theoretically, a longer soaking time will allow CO_2 to reach deeper into the formation. On the contrary, no change in production can be observed from **Table 36** and **Fig. 69**. The case with 15 days and 100 days soaking time even had very slight decrease

in production due to the longer shut-in time. However, keep in mind that the cases with 15 days and 100 days shut in time achieved similar recovery factors as the 1 day shut in case, which means that the production rate was still slightly enhanced for the longer soaking time cases to make up for the production time losses. In other words, the longer soaking time allowed some degree of CO_2 penetration into the matrix. Unfortunately, because the diffusion coefficient is small, the improvement was not very pronounced.

	Soaking Time, day	Recovery Factor, %
Case 1	N/A	4.11
Case 2	1	4.53
Case 3	15	4.52
Case 4	100	4.52

Table 36 – Sensitivity analysis for soaking time.

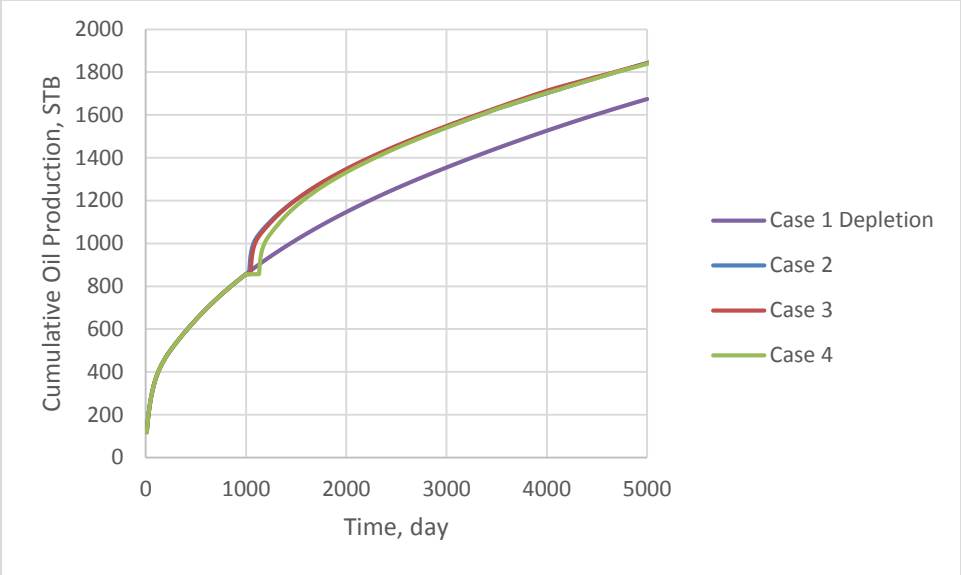

Fig. 69 – Cumulative oil production for soaking time sensitivity analysis.

4.5.4.6 Number of Cycles

In this section, the effect of increasing the number of injection cycles was investigated. From **Table 37** and **Fig. 70**, one can see that more injection cycles produced higher oil volumes. However, Fig. 70 also indicated the increment in recovery factor display a decreasing trend as the number of cycle increases. Economic analysis is in need to evaluate the optimal number of cycles.

	Injection Cycle	Recovery Factor, %
Case 1	N/A	4.11
Case 2	1	4.52
Case 3	2	4.81
Case 4	3	5.04

Table 37 – Sensitivity analysis of number of injection cycles.

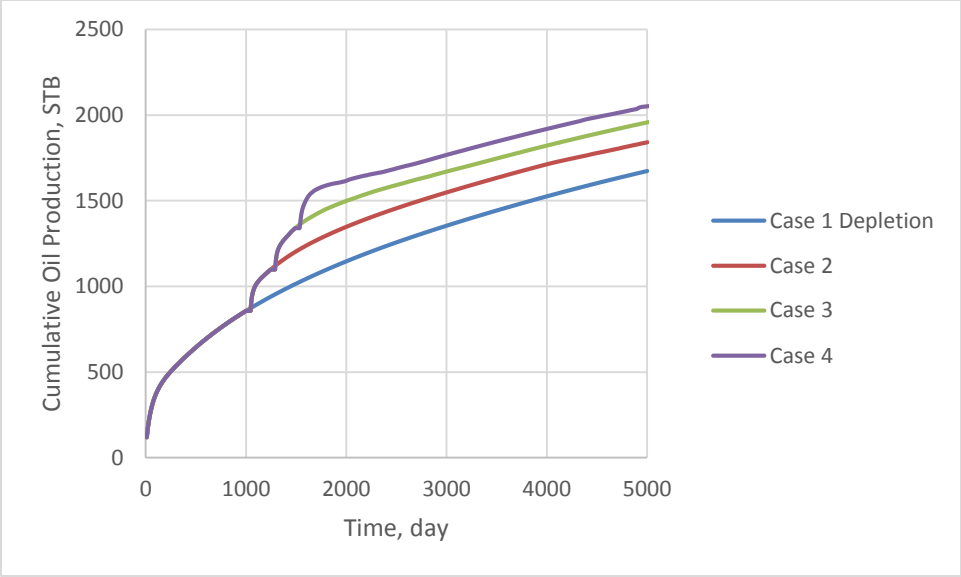

Fig. 70 – Cumulative production of number of cycles sensitivity analysis.

4.5.4.7 LPG Injection

From the previous sections, one can draw the conclusion that CO_2 huff n puff process can increase the recovery factor from liquid rich shale plays. This section compares the performance of CO_2 with LPG with a one cycle injection case. The LPG injected was composed of 33% of C_3 and 64% of C_4. In a reservoir temperature of 150

°F, the LPG is in liquid phase and can mix with the resident oil at any proportion above 200 psi, even under the saturation pressure. The reason to consider LPG injection is because LPG develops miscibility with oil at a much lower pressure than CO_2 and does not produce acidic solutions with water. **Table 38** and **Fig. 71** summarizes the performance of both CO_2 and LPG in a one cycle huff n puff scheme. From Table 38, one can conclude that CO_2 outperformed LPG by almost 1% in recovery. In addition, if compared with a primary depletion only case (recovery factor of 4.11%), injecting LPG actually hurt recovery in this case. Furthermore, the cost of LPG is significantly more expensive than that of CO_2. Therefore, in this particular reservoir, LPG huff n puff scheme is not economical.

	Injected Solvent	Recovery Factor, %
Case 1	CO_2	4.52
Case 2	LPG	3.88

Table 38 – Comparison of CO_2 and LPG performance.

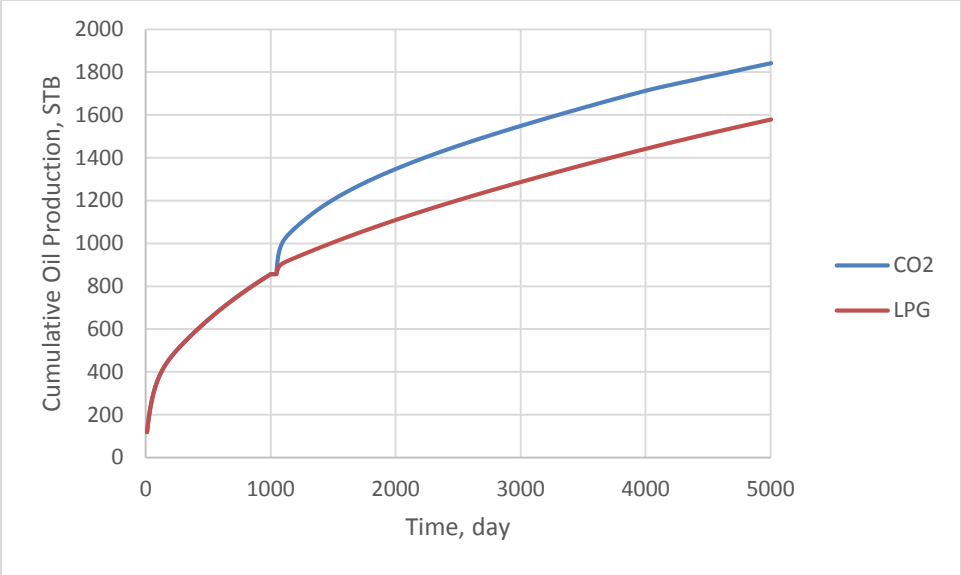

Fig. 71 – Cumulative production of CO_2 and LPG injections.

4.5.4.7.1 Reservoir Temperature

The reservoir temperature was increased to 241 °F (Bakken temperature) in this part of the study to investigate the change in performance of both CO_2 and LPG injections. **Table 39** and **Fig. 72** show that at higher temperature and same operating conditions as the base case in the previous sections, the effectiveness of CO_2 injection was dramatically reduced. This is because at higher reservoir temperatures, the MMP of CO_2 with oil increases, whereas LPG still remains miscible with the oil and could possibly exist as a gas phase when the pressure start declining during the production phase. That is primarily why LPG outperformed CO_2 at reservoir temperature of 241 °F. From this case study, one should note that the injection pressure for CO_2 should be

increased accordingly as the reservoir becomes deeper (higher pressure and higher temperature).

	Injected Solvent	Reservoir Temperature, F	Recovery Factor, %
Case 1	CO_2	150	4.52
Case 2	LPG	150	3.88
Case 3	CO_2	241	7.42
Case 4	LPG	241	7.73

Table 39 – Recovery factor of CO_2 and LPG injections at different reservoir temperatures.

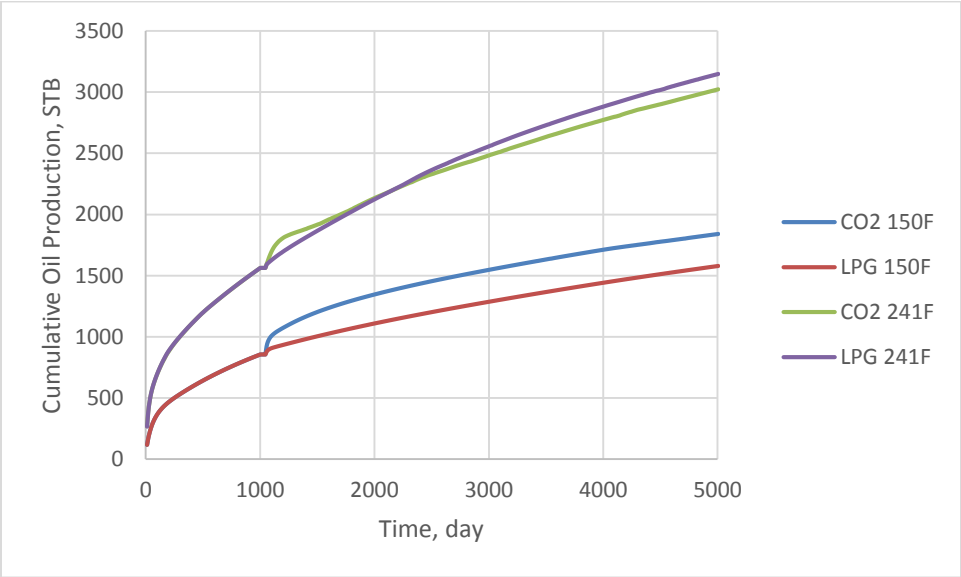

Fig. 72 – Cumulative production of CO_2 and LPG injections at different reservoir temperatures.

4.5.4.7.2 Different LPG Compositions

This section investigated the performance of LPG with different compositions in comparison with CO_2 by adding 20%, 40%, 60%, and 80% of C_2 into the C_3 and C_4 mixture. The mole fractions of C_3 and C_4 were kept the same at 33% and 64%. In case 5, where 80% of C_2 was added, the fluid is above its critical pressure at the give temperature of 150 °F. As seen in **Table 40** and **Fig. 73**, adding C_2 into the LPG only slightly improved its performance. However, the recovery factor (even with 80% of C_2 added) was still below the recovery factor from the primary depletion only case, which is 4.11%. Combining the conclusion drawn from the previous two sections, LPG is not recommended as the injected solvent in the huff n puff process for the simulated reservoir.

	Injected Solvent	Recovery Factor, %
Case 1	CO_2	4.52
Case 2	20% C_2 LPG	3.87
Case 3	40% C_2 LPG	3.88
Case 4	60% C_2 LPG	3.91
Case 5	80% C_2 LPG	3.99

Table 40 – Performance of LPG with different amount of C_2 added.

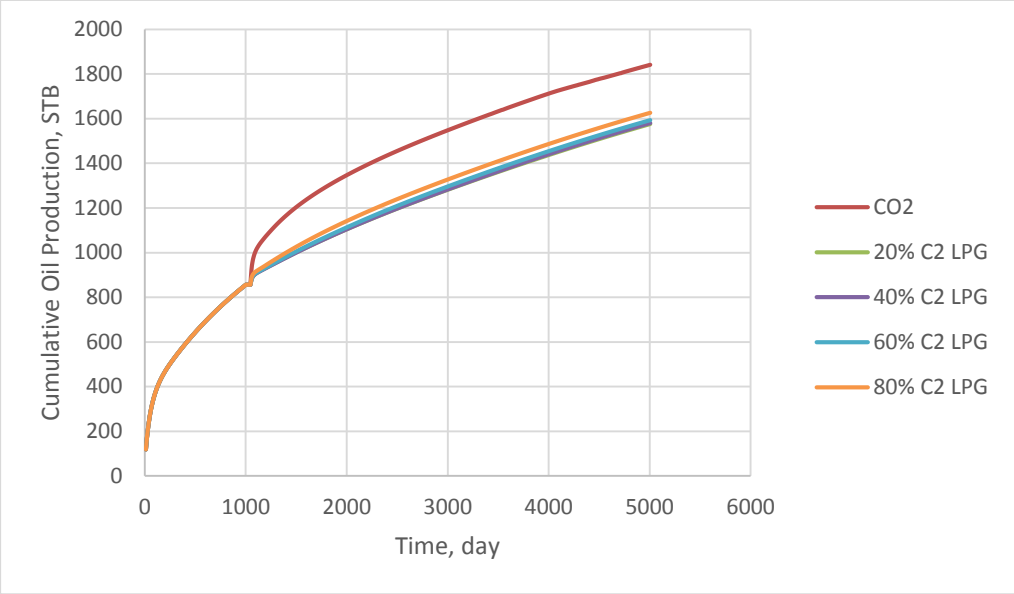

Fig. 73 – Cumulative production of LPG cases with different amount of C_2 added.

5. CONCLUSIONS AND RECOMMENDATIONS

5.1 Conclusions

Core scale simulation:

1. Cross-phase diffusion must be included to properly model the diffusion process.
2. During the core flood experiments, diffusion and achieving miscibility are the main mechanisms contributing to oil recovery. Deactivating diffusion resulted in zero oil production despite the fact that certain amounts of CO_2 were able to enter the core due to the initial pressure difference between the fracture and the matrix (convection). Oil volume swelling has no effect on oil production.
3. The oil recovery factor is sensitive to the following parameters: matrix porosity, fracture porosity, saturation, region pressure, and diffusion coefficient.
4. The oil recovery factor is not sensitive to the following parameters: matrix permeability, fracture permeability, relative permeability, and capillary pressure.
5. By changing the porosity values and diffusion coefficient, a final production of 0.4 ml was achieved from the models following the experimental schedules.

Field scale simulation:

1. Injecting CO_2 when pressure is below the bubble point pressure has more pronounced impact on improving oil recovery. Whereas, injecting CO_2 when pressure is still above the bubble point pressure (or the MMP) does not have a significant impact on oil recovery. Re-pressurizing the reservoir (or rather the fractures) and solution gas drive are the contributing mechanisms for improved oil recovery.
2. The oil recovery factor is sensitive to the following parameters: matrix porosity, matrix permeability, fracture porosity, fracture permeability, time of first injection, length of injection time, injection rate, injection pressure, number of cycles, and reservoir temperature.
3. The oil recovery factor is not sensitive to the following parameters: capillary pressure, diffusion coefficient, and length of soaking time.
4. Unlike the laboratory core flood experiment, the fractures cannot be fully saturated with CO_2 during a cyclic gas injection. Therefore, although diffusion was the mechanism responsible for oil production during the experiment, it has little contribution in the field case.
5. Although LPG can develop miscibility with oil at much lower pressure (even below saturation pressure), CO_2 injection outperformed LPG injection in the huff n puff field case. Varying the composition of LPG can slightly improve its performance.

5.2 Future Work Recommendations

Modeling shale reservoir characteristics at nano-scale is a difficult task. This study provided a preliminary basis for the future studies to better understand the mass transfer and recovery mechanisms for liquid rich shale reservoirs using CO_2. Many aspects could not be included in this study due to the many limitations. In future work, the following attributes could be considered in the modeling process: water movement due to capillary forces; CO_2 solubility in water; non-Darcy flow in fractures and matrix such as Knudson diffusion; hysteresis; gas adsorption in the kerogen network. Better rock characterization is needed to provide a solid base for simulation works, such as the organic and inorganic matrix with multiple porosity systems as shown in the study by Yan *et al*. (2013). In addition, fluid behavior in nano-scale pores differs from that in bulk volume. Corrections should be done on the fluid PVT properties in confined spaces as proposed in the studies by Teklu *et al*. (2013) and Teklu *et al*. (2014). Using a black oil model to match the results obtained from compositional model can be considered. Lastly, field case direct injection with multiple wells can be modeled and results can be compared with the huff n puff case.

For future experimental work, adding a tracer in the injected CO_2 can track the movement of CO_2 molecules over time, which can provide a better understanding of the diffusion process and experimental values of the diffusion coefficients.

REFERENCES

Ahmed, A.B., Bai. B., and Runar, N. 2012. A Selection of Criterion for CO_2-Enhanced Oil Recovery and Dispersion Modeling of High-Pressure CO_2 Releases. SPE paper presented at the SPE Western Regional Meeting, Bakersfield, California, USA, 19-23 March. SPE-152998-MS. http://dx.doi.org/10.2118/152998-MS.

Bird, R.B., Stewart, W.R., and Lightfoot, E.N. 2002. *Transport Phenomena*, second edition. New York, New York: John Wiley & Sons, Inc. ISBN: 0-470-11539-4.

Chen, C., Balhoff, M., and Mohanty, K.K. 2014. Effect of Reservoir Heterogeneity on Primary Recovery and CO_2 Huff 'n' Puff Recovery in Shale-Oil Reservoirs. *SPE Reservoir Evaluation & Engineering* **17** (3): 404-413. SPE-164553-PA. http://dx.doi.org/10.2118/164553-PA.

Chen, L., Zhang, L., Kang, Q. *et al*. 2015. Nanoscale Simulation of Shale Transport Properties Using the Lattice Boltzmann Method: Permeability and Diffusivity. *Scientific Reports*. 5, Article number: 8089. http://dx.doi.org/10.1038/srep08089.

Coats, K.H. 1980. An Equation of State Compositional Model. *Society for Petroleum Engineers Journal* **20** (5): 363-376. SPE-8284-PA. http://dx.doi.org/10.2118/8284-PA.

CMG User's Guide – GEM: Advanced Compositional and Unconventional Reservoir Simulator. 2013. Computer Modeling Group Ltd. (CMG). Calgary, Canada.

Corey, A.T. 1954. The Interrelation between Gas and Oil Relative Permeabilities. *Producers Monthly* **19** (1): 38-41.

Darvish, G.R. Lindeberg, E.G., Holt, T., and *et al*. 2006. Reservoir Conditions Laboratory Experiment of CO_2 Injection into Fractured Cores. SPE paper presented at the SPE Europec/EAGE Annual Conference and Exhibition, Vienna, Austria, 12-15 June. SPE-99650-MS. http://dx.doi.org/10.2118/99649-MS.

Deen, W.M. 1998. *Analysis of Transport Phenomena*, first edition. New York, New York: Oxford University Press, Inc. ISBN: 0-19-508494-2.

Donaldson, E.C., Chilingarian, G.V. Yen, T.F. *et al*. 1989. *Enhanced Oil Recovery, II Processes and Operations.* AE Amsterdam, the Netherlands: Elsevier Science Publishers B.V. ISBN: 0-444-41625-0.

Eclipse. 2014. Eclipse Reservoir Simulation Software Technical Description, version 2014.1. Schlumberger.

EIA. 2013. Petroleum & Other Liquids. http://www.eia.gov/petroleum/ (accessed 20 November 2014).

Eide, O., Ferno, M.A., and Graue, A. 2014. Visualization of CO_2 EOR by Diffusion in Fractured Chalk. SPE paper presented at the SPE Annual Technical Conference and Exhibition, Amsterdam, The Netherlands, 27-29 October. SPE-170920-MS. http://dx.doi.org/10.2118/170920-MS.

Fai-Yengo, V., Rahnema, H., and Alfi, M. 2014. Impact of Light Component Stripping During CO_2 Injection in Bakken Formation. SPE paper presented at the Unconventional Resources Technology Conference, Denver, CO, USA, 25-27 August. SPE-1922932-MS. http://dx.doi.org/10.15530/urtec-2014-1922932.

Firoozabadi, A. 1999. *Thermodynamics of Hydrocarbon Reservoirs.* New York, New York: McGraw-Hill Companies, Inc. ISBN: 0-07-022071-9.

Gamadi, T.D., Elldakli, F., and Sheng, J.J. 2014. Compositional Simulation Evaluation of EOR Potential in Shale Oil Reservoirs by Cyclic Natural Gas Injection. URTeC paper presented at the Unconventional Resources Technology Conference, Denver, CO, USA, 25-27 August. URTeC-1922690. http://dx.doi.org/10.15530/urtec-2014-1922690.

Green, D.W. and Willhite, G.P. 1998. *Enhanced Oil Recovery*. SPE Textbook Series Vol. 6. Society of Petroleum Engineers. ISBN: 978-1-55563-077-5.

Grogan, A.T. and Pinczewski, W.V. 1987. The Role of Molecular Diffusion Processes in Tertiary CO_2 Flooding. *Journal of Petroleum Technology* **39** (5): 591-602. SPE-12706-PA. http://dx.doi.org/10.2118/12706-PA.

Hawthorne, S.B., Gorecki, C.D., Sorensen, J.A. *et al*. 2013. Hydrocarbon Mobilization Mechanisms from Upper, Middle, and Lower Bakken Reservoir Rocks Exposed to CO_2. SPE paper presented at the SPE Unconventional Resources Conference,

Calgary, Alberta, Canada, 5-7 November. SPE-167200-MS. http://dx.doi.org/10.2118/167200-MS.

Haynes, W.M. 2015. *CRC Handbook of Chemistry and Physics*, nighty-fifth edition. Boulder, Colorado: Nobel Laureate. ISBN: 1-4822-0867-9.

Holme, A. 2013. *Optimization of Liquid-Rich Shale Wells*. Master thesis, Norwegian University of Science and Technology, Trondheim, Norway.

Hoteit, H. 2013. Modeling Diffusion and Gas-Oil Mass Transfer in Fractured Reservoirs. *Journal of Petroleum Science and Engineering* **105** (3): 1-17. http://dx.doi.org/10.1016/j.petrol.2013.03.007.

Hoteit, H. 2011. Proper Modeling of Diffusion in Fractured Reservoirs. SPE paper presented at the SPE Reservoir Simulation Symposium, The Woodlands, TX, USA, 21-23 February. SPE-141937-MS. http://dx.doi.org/10.2118/141937-MS.

Hoteit H. and Firoozabadi, A. 2009. Numerical Modeling of Diffusion in Fractured Media for Gas-Injection and Recycling Schemes. *SPE Journal* **14** (2): 323-337. http://dx.doi.org/10.2118/103292-PA.

Jarrell, P.M., Fox, C.E., Stein, M.H. *et al*. 2002. *Practical Aspects of* CO_2 *Flooding.* SPE Monograph Series, Vol. 22. Richardson, TX: SPE. ISBN: 978-1-55563-096-6.

Karimaie, H. 2007. *Aspects of Water and Gas Injection in Fractured Reservoirs*. PhD Dissertation, Norwegian University of Science and Technology, Trondheom, Norway.

Kovscek, A.R., Tang, G.Q., and Vega, B. 2008. Experimental Investigation of Oil Recovery from Siliceous Shale by CO_2 Injection. SPE paper presented at the SPE Annual Technical Conference and Exhibition, Denver, CO, USA, 21-24 September. SPE-115679-MS. http://dx.doi.org/10.2118/115679-MS.

Landis, E.N. and Keane, D.T. 2010. X-ray Microtomography. *Materials Characterization* **61** (12): 1305-1316.

Leahy-Dios, A. and Firoozabadi, A. 2007. Unified Model for Non-ideal Multicomponent Molecular Diffusion Coefficients. *AIChE Journal* **53** (11): 2932-2939. http://dx.doi.org/10.1002/aic.11279.

Lie, S.H. 2013. *Diffusion as an Oil Recovery Mechanism during CO_2 Injection in Fractured Reservoirs.* Master Thesis in Reservoir Physics, University of Bergen, Bergen, Norway.

Liu, G., Sorensen, J.A., Braunberger, J.R. *et al.* 2014. CO_2-Base Enhanced Oil Recovery from Unconventional Reservoirs: A Case Study of the Bakken Formation. SPE paper presented at the SPE Unconventional Resources Conference, The Woodlands, TX, USA, 1-3 April. SPE-168979-MS. http://dx.doi.org/10.2118/168979-MS.

McKay, W.N. 1971. Experiments Concerning Diffusion of Multicomponent Systems at Reservoir Conditions. *Journal of Canadian Petroleum Technology* **10** (2): 25-32. PETSOC-71-02-04. http://dx.doi.org/10.2118/71-02-04.

Mohammadi, S. Kharrat, R. Khalili, M. and Mehranfar, M. 2011. Optimal Conditions for Immiscible Recycle Gas Injection Process: A Simulation Study for One of the Iranian Oil Reservoirs. *Scientia Iranica* **18** (6): 1407-1414. http://dx.doi.org/10.1016/j.scient.2011.10.003.

Morel, D., Bourbiaux, B., Latil, M. *et al*. 1993. Diffusion Effects in Gas-flooded Light-Oil Fractured Reservoirs. *SPE Advanced Technology Series* **1** (02): 100-109. SPE-20516-PA. http://dx.doi.org/10.2118/20516-PA.

Ozkan, E., Raghavan, R., and Apaydin, O.G. 2010. Modeling of Fluid Transfer from Shale Matrix to Fracture Network. SPE paper presented at the SPE Annual Technical Conference and Exhibition, Florence, Italy, 19-22 September. SPE-134830-MS. http://dx.doi.org/10.2118/134830-MS.

Pasala, S.M. 2010. *CO_2 Displacement Mechanisms: Phase Equilibria Effects and Carbon Dioxide Sequestration Studies*. PhD Dissertation in Chemical Engineering, the University of Utah, Salt Lake City, Utah.

Pedersen, K.S., Christensen, P.L., and Shaikh, J.A. 2014. *Phase Behavior of Petroleum Reservoir Fluids*, second edition. Boca Raton, Florida: CRC Press. ISBN: 978-1-4398-5227-9.

Perkins, T.K. and Johnston, O.C. 1963. A Review of Diffusion and Dispersion in Porous Media. *Society of Petroleum Engineers Journal* **3** (1): 70-84. SPE-480-PA. http://dx.doi.org/10.2118/480-PA.

Reid, R.C., Prausnitz, J.M. and Sherwood, T.K. 1977. *The Properties of Gases and Liquids*, third edition. New York, New York: McGraw-Hill.

Rivera, D.S. 2014. *Reservoir Simulation and Optimization of CO_2 Huff-and-Puff Operations in the Bakken Shale*. Master thesis, University of Texas at Austin, Austin, TX.

Sagar, K. V., Rai, C. S. and Sondergeld, C.H. 2010. Petrophysical Characterization of Barnett Shale. SPE paper presented at SPE Unconventional Gas Conference, Pittsburgh, Pennsylvania, USA, 23-25 February. SPE-131770-MS. http://dx.doi.org/10.2118/131770-MS.

Sahimi, M. 2011. *Flow and Transport in Porous Media and Fractured Rock.* New York, New York: Wiley.Vch Verlag Gmbh & Co.

Shafikova, G.M. 2013. *Analysis of Diffusion Models in Eclipse 300*. Master Thesis, Norwegian University of Science and Technology, Trondheim, Norway.

Sheng, J. J. 2014. Enhanced Oil Recovery in Shale Reservoirs by Gas Injection. *Journal of Natural Gas Science and Engineering* **22**: 252-259. http://dx.doi.org/j.jngse.2014.12.002.

Sigal, R.F. 2002. The Pressure Dependence of Permeability. *Petrophysics Journal* **43**(2): 92-102. ISSN: 1529-9074.

Sigal, R.F. 2013. Mercury Capillary Pressure Measurements on Barnett Core. *SPE Reservoir Evaluation & Engineering Journal* **16** (4): 432-442. SPE-167607-PA. http://dx.doi.org/10.2118/167607-PA.

Sigmund, P. M. 1976a. Prediction of Molecular Diffusion at Reservoir Conditions. Part 1 – Measurement and Prediction of Binary Dense Gas Diffusion Coefficients. *Petroleum Society of Canada* **15** (2). PETSOC-76-02-05. http://dx.doi.org/10.2118/76-02-05.

Sigmund, P. M. 1976b. Prediction of Molecular Diffusion at Reservoir Conditions. Part II – Estimating the Effects of Molecular Diffusion and Convective Mixing in Multicomponent Systems. *Petroleum Society of Canada* **15** (3). PETSOC-76-03-07. http://dx.doi/org/10.2118/76-03-07.

Taud, H., Martinez-Angeles, R., Parrot, J.F. *et al*. 2005. Porosity Estimation Method by X-ray Computed Tomography. *Journal of Petroleum Science and Engineering* **47** (3-4), 209-217. http://dx.doi.org/10.1016/j.petrol.2005.03.009.

Teklu, T.W., Alharthy, N., Kazemi, H. *et al.* 2013. Minimum Miscibility Pressure in Conventional and Unconventional Reservoirs. SPE paper presented at the Unconventional Resources Technology Conference, Denver, CO, USA, 12-14 August. SPE 168865/URTeC-1589572-MS. http://dx.doi.org/10.1190/URTEC2013-228.

Teklu, T.W., Alharthy, N., Kazemi, H. *et al*. 2014. Phase Behavior and Minimum Miscibility Pressure in Nanopores. *SPE Reservoir Evaluation & Engineering* **17** (3): 396-403. SPE-168865-PA. http://dx.doi.org/10.2118/168865-PA.

Terry, R.E. 2001. Enhanced Oil Recovery. *Encyclopedia of Physical Science and Technology*, third edition, **18**: 503-518.

Thomas, G.A. and Monger, T.G. 1991. Feasibility of Cyclic CO_2 Injection for Light Oil Recovery. *SPE Reservoir Engineering* **6** (2): 179-184. SPE-20208-PA. http://dx.doi.org/10.2118/20208-PA.

Tovar, F.D., Eide, O., Graue, A. *et al*. Experimental Investigation of Enhanced Recovery in Unconventional Liquid Reservoirs Using CO_2: A Look Ahead to the Future of Unconventional EOR. SPE paper presented at SPE Unconventional Resources Conference, The Woodlands, TX, USA, 1-3 April. SPE-169022-MS. http://dx.doi.org/10.2118/169022-MS.

Vega, B., O'Brien, W.J., and Kovscek, A.R. 2010. Experimental Investigation of Oil Recovery From Siliceous Shale by Miscible CO_2 Injection. SPE paper presented at the SPE Annual Technical Conference and Exhibition, Florence, Italy, 19-22 September. SPE-135627-MS. http://dx.doi.org/10.2118/135627-MS.

Wan, T. and Sheng, J. 2015. Compositional Modelling of the Diffusion Effect on EOR Process in Fractured Shale-Oil Reservoirs by Gasflooding. *Journal of Canadian*

Petroleum Technology **54** (2): 107-115. SPE-1891403-PA. http://dx.doi.org/10.2118/2014-1891403-PA.

Wan, T., Sheng, J.J., and Soliman, M.Y. 2013. Evaluate EOR Potential in Fractured Shale Oil Reservoirs by Cyclic Gas Injection. SPE paper presented at the Unconventional Resources Technology Conference, Denver, CO, USA, 12-14 August. SPE-168880-MS. http://dx.doi.org/10.1190/URTEC2013-187.

Yan, B., Wang, Y., and Killough, J.E. 2013. Beyond Dual-Porosity Modeling for the Simulation of Complex Flow Mechanisms in Shale Reservoirs. SPE paper presented at the SPE Reservoir Simulation Symposium, the Woodlands, TX, USA, 18-20 February. SPE-163651-MS. http://dx.doi.org/10.2118/163651-MS.

Yang, T., Fevang, Ø., Ruhrgas, E. *et al*. 2007. LBC Viscosity Modeling of Gas Condensate to Heavy Oil. SPE paper presented at the SPE Annual Technical Conference and Exhibition, Anaheim, CA, USA, 11-14 November. SPE-109892-MS. http://dx.doi/org/10.2118/109892-MS.

Yaws, C.L. 2008. *Thermophysical Properties of Chemicals and Hydrocarbons.* Norwich, New York: William Andrew Inc. ISBN: 978-0-8155-1596-8.